FLOW/ACOUSTICS MECHANISMS IN TWO- AND THREE-DIMENSIONAL WAKE VORTICES

by

WENHUA LI

B.S., Tongji University, 1997
M.S., Shanghai Jiaotong University, 2000

AN ABSTRACT OF A DISSERTATION

submitted in partial fulfillment of the requirements for the degree

DOCTOR OF PHILOSOPHY

Department of Mechanical and Nuclear Engineering
College of Engineering

KANSAS STATE UNIVERSITY
Manhattan, Kansas

2007

Abstract

In this study, a vortex particle method is used to simulate incompressible vortical flows, specifically aircraft wake vortices. This is particularly suitable for a wake vortex system that is slowly varying in the axial direction and has a high Reynolds number and low Mach number. The flow field, in the form of vorticity, is employed as the source in the far-field acoustic calculation using a vortex sound formula that enables computation of acoustic signals radiated from an approximated incompressible flow field.

In a two-dimensional vortex system, the stretching effect in the axial direction is neglected. The purpose of this study is to focus on vortex core behaviors. A numerical simulation is performed in a more realistic wake consisting of a counter-rotating vortex pair with inviscid ground effects and shear flows. A Kirchhoff spinning-core vortex model is thus used as a starting point.

In a vortex system with multiple vortices, such as a complicated aircraft vortex wake vortices, the sound emission frequency of the unsteady vortex core is subjected to change because of interactions between multiple vortices. The behaviors of the influence, indicated by the ratio between the core size and the distance of the vortices, are investigated as well as the underlining vortex core dynamic mechanisms. Cases of co-rotating vortices and a multiple-vortex system composed of two counter-rotating vortex pairs are studied for applications to aircraft wake vortex sound.

In three-dimensional vortices, sinusoidal instabilities, which occur in the axial direction at various length scales, result in significant flow structure changes in these vortices, and thus influence their radiated acoustic signals. Cases of vortex rings and a pair of counter-rotating vortices are studied when they are undergoing both long-wave

and short-wave instabilities. Both inviscid and viscous interactions are considered and the effects of turbulence are simulated using sub-grid-scale models. A higher peak frequency than the Kirchhoff frequency appears due to the straining field caused by mutual perturbation, under both long-wave and short-wave instabilities. Vortices with the initial core vorticity of the Gaussian distribution and the elliptic distribution are also studied.

FLOW/ACOUSTICS MECHANISMS IN TWO- AND THREE-DIMENSIONAL WAKE VORTICES

by

WENHUA LI

B.S., Tongji University, 1997
M.S., Shanghai Jiaotong University, 2000

A DISSERTATION

submitted in partial fulfillment of the requirements for the degree

DOCTOR OF PHILOSOPHY

Department of Mechanical and Nuclear Engineering
College of Engineering

KANSAS STATE UNIVERSITY
Manhattan, Kansas

2007

Approved by:

Major Professor
Dr. Zhongquan Charlie Zheng

Abstract

In this study, a vortex particle method is used to simulate incompressible vortical flows, specifically aircraft wake vortices. This is particularly suitable for a wake vortex system that is slowly varying in the axial direction and has a high Reynolds number and low Mach number. The flow field, in the form of vorticity, is employed as the source in the far-field acoustic calculation using a vortex sound formula that enables computation of acoustic signals radiated from an approximated incompressible flow field.

In a two-dimensional vortex system, the stretching effect in the axial direction is neglected. The purpose of this study is to focus on vortex core behaviors. A numerical simulation is performed in a more realistic wake consisting of a counter-rotating vortex pair with inviscid ground effects and shear flows. A Kirchhoff spinning-core vortex model is thus used as a starting point.

In a vortex system with multiple vortices, such as a complicated aircraft vortex wake vortices, the sound emission frequency of the unsteady vortex core is subjected to change because of interactions between multiple vortices. The behaviors of the influence, indicated by the ratio between the core size and the distance of the vortices, are investigated as well as the underlining vortex core dynamic mechanisms. Cases of co-rotating vortices and a multiple-vortex system composed of two counter-rotating vortex pairs are studied for applications to aircraft wake vortex sound.

In three-dimensional vortices, sinusoidal instabilities, which occur in the axial direction at various length scales, result in significant flow structure changes in these vortices, and thus influence their radiated acoustic signals. Cases of vortex rings and a

pair of counter-rotating vortices are studied when they are undergoing both long-wave and short-wave instabilities. Both inviscid and viscous interactions are considered and the effects of turbulence are simulated using sub-grid-scale models. A higher peak frequency than the Kirchhoff frequency appears due to the straining field caused by mutual perturbation, under both long-wave and short-wave instabilities. Vortices with the initial core vorticity of the Gaussian distribution and the elliptic distribution are also studied.

Table of Contents

List of Figures

List of Tables

Nomenclature

Symbol list

$\mathbf{x}$	position of a particle	r	radial distance
$\mathbf{y}$	far-field position	A	perturbation amplitude
$\Delta\boldsymbol{x}$, $\Delta\boldsymbol{y}$	far-field position	Re	Reynolds number
$\boldsymbol{\omega}$	vorticity	Ω	angular frequency
Γ	circulation	Δt	time step size
$\boldsymbol{\alpha}$	vorticity strength	ξ	cut-off function
v	viscosity	η^{lab}	Laplacian kernel for PSE
σ	blob radius of a particle	f	field quantity
V	volume of a particle	Q	source term
$\mathbf{u}$	velocity	M	Mach number
$\mathbf{K}$	Biot-Savart kernel	W	remeshing kernel
p	pressure	θ	angle of the far-field receiver
c	sound speed	ε	eccentricity
b	wake vortex span	n	wave number
h	spatial size	SGS	sub-grid scale
a	core radius	LES	large eddy simulation
R	vortex ring radius		

Subscript

p, q	particle
σ	blob radius of a particle

Acknowledgements

The time I have spent at Kansas State University was certainly enjoyable and fruitful. I would like to express my gratitude to my advisor, Professor Zhongquan Charlie Zheng, for his support, patience, and guidance through the past four years. He has always been available for consultations and inspiration. I also must thank other members of my committee: Professors B. Terry Beck, Ken Shultis and Stephen S. Gao for their comments and encouragement.

I have enjoyed working with people in our office. I received help from Ning Zhang (Michael) about Unix and CFD. I also thank Satish K. Motipalli for giving me countless suggestions during my stay here.

Most importantly I want to thank my wife and best friend, Lixia Fan, who has given me companionship, support and confidence during the four years. And the birth of our daughter Amanda Li was a special blessing!

This research has been funded under NASA grants NNL04AA77G with Wayne Bryant as the technical monitor, and under DOT Volpe contract DTRT57-06-P-80188 with Frank Wang as the technical monitor. Some of the computer hours were provided by the SHARCNET of Canada.

1 Introduction

1.1 A Brief Description of Aircraft Vortex Wake Problems

The behavior of aircraft vortex wake has been an important safety consideration in air traffic control. Wake vortices present a hazard to a following aircraft, especially to lighter following ones, because a vortex can cause a dangerous roll of an aircraft flying into it. Wake hazard also limits airport capacity due to aircraft spacing. Donaldson and Bilanin (1975) provided a comprehensive summary of the research prior to 1975. Wake vortex research has been conducted in the U.S. for over thirty years by a diverse group including the participation of the FAA, NASA, the Air Force, the Army, airlines, airport operators, university groups and so on.

An aircraft, like a ship, leaves a wake behind it. This wake is in the form of two counter-rotating swirling rolls of air—the wake vortices—the outer vortex pair is produced at the wing tips and the inner one by flaps and horizontal tail planes (see Figure 1.1). All aircraft produce wake vortices—much like small horizontal tornadoes trailing behind the wing tips.

Once vortices are formed, they may last for several minutes and stretch for many kilometers (km) behind the aircraft. The strength of the vortices basically depends on the aircraft weight divided by the product of air density, flying speed, and wingspan. It therefore generally increases with aircraft weight. Vortices last longer in calm air, and atmospheric turbulence hastens their decay. When the plane is larger and heavier, the wake is stronger, which means small aircraft that follow larger ones can encounter wake vortices if they are not kept far enough apart. The turbulence due to the wake can be severe enough to cause a small plane to crash. On

the other hand, wake vortices are normally invisible, and pilots have no warning that they are flying into them. For this reason, the International Civil Aviation Organization has strict rules about the permitted spacing between aircraft, based on their sizes. In instrument flying conditions, aircraft may follow no closer than 3 nautical miles (5.56 km), and a small aircraft must follow at least 6 nautical miles (11.12 km) behind a heavy jet (Greene et al. 1991).

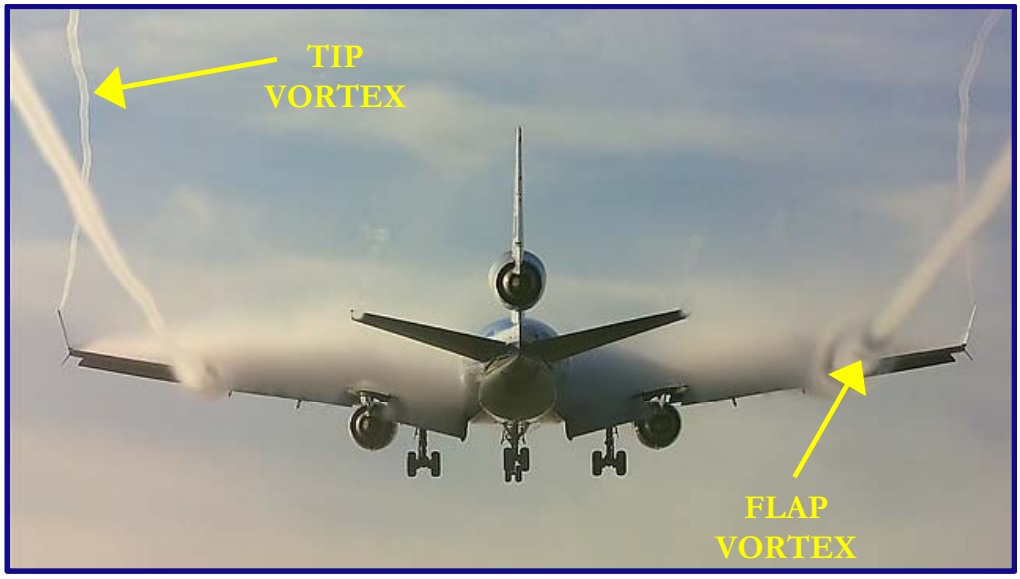

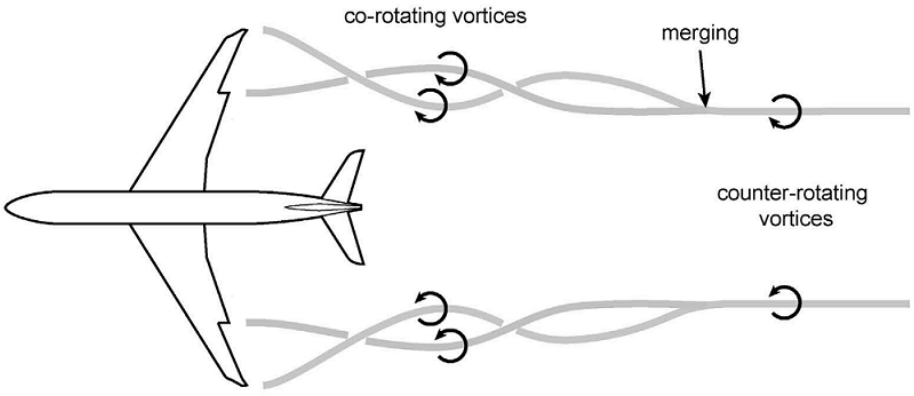

Figure 1.1 Schematic of counter-rotating pairs produced by aircraft (photo taken from http://www.airliners.net)

There has been no system to accurately predict wake vortex patterns and quantify the spacing needed for safety. The lack of information forces air traffic controllers to use rigidly fixed distances to separate different classes of aircraft during bad weather. This causes air traffic delays that disrupt flight schedules and increase costs. Engineers may also be able to design aircraft that produce less hazardous wakes. However, it is not possible to avoid vortices being created. They are an inescapable consequence of aerodynamics.

The wake flow behind an aircraft can be described by near-field and far-field characteristics. In the near field small vortices emerge from the vortex sheet at the wing tips and at the edges of the landing flaps. The governing physical processes are boundary-layer separation, roll-up of the vortex sheet, merging of co-rotating vortices, initiation of vortex instability, etc. These processes define the aircraft-induced characteristics of the wake for its development in the far field. In a summary, the field of wake vortices is generally split into four developing processes (see Figure 1.1): (a) vortex formation; (b) vortex roll-up and merging; (c) vortex drift, instability appearance; and (d) vortex collapse, disperse, and the formation of vortex rings. The reader should refer to Spalart (1998), Gerz (2002) and Jacquin (2005) for more detailed review of studies of wake vortex behaviors.

1.2 Selected Reviews of Current Studies on Vortex Dynamics

1.2.1 A Perturbed Vortex Ring

The stability of vortex rings is one of the important problems in hydrodynamic stability. Widnall and Sullivan (1973) proposed a linear long wavelength analysis of a vortex ring with invariant cores. When the self-induced rotation of vortex perturbation balances the rotation induced by the mean velocity of the ring, instability of the vortex ring around the azimuthal

direction occurs. For a ring with a non-deformable core (i.e., the vortex core size is much smaller than both the local radius of curvature and the wavelength of any perturbation along the filament), the perturbation of the vortex ring is taken to be sinusoidal displacements in both the radial and axial directions. Widnall and Sullivan (1973) found the most unstable wave number - $n=k*R/a$, where k=1.44 - corresponding to asymptotic results (R/a is the ratio of ring radius to core radius). In their analysis of short wavelength instability, Widnall et al. (1974, 1977) used a slender ring with deformable core for consideration. They supposed that the instability of the vortex ring occurs due to short wave perturbation around the azimuth whenever there is a balance between the self-induced rotation of the waves and the net translational velocity induced owing to the ring strain field. For a slender vortex ring, the most unstable wave number occurs at $n=2.5*R/a$ for the second radial mode with constant vorticity inside the core.

In addition to the theoretical studies of azimuthal instability, there are encouraging prospects for numerical simulation of this phenomenon. Knio and Ghoniem (1990) constructed a 3-D vortex method (vortex filament) for the simulation of inviscid incompressible flow, and calculated the linear growth of azimuthal instability waves for a perturbed vortex ring with non-deformable core and a deformable core. Their results agree with the linear stability theory of Widnall and Sullivan (1973) and Widnall et al. (1974). Whether in the simulation of a thin tube model or a vortex torus, they both observed the generation of hairpin vortex structures at the edge of the core, and the shape of the turbulent vortex ring is in agreement with experimental observations (Lugt 1983, Dyke 1982). Shariff et al. (1994) studied the instability of viscous vortex ring with a thicker core, with the Reynolds number as high as 5500, using the finite-difference method. In their analysis, multiple bands of wave numbers are amplified, each band having a distinct radial structure. In addition, they found a viscous correction factor of the peak

inviscid growth rate. Their computations were also extended to the nonlinear growth rate regime before the calculational resolution ran out.

The basic mechanisms of sound generation by a perturbed vortex are discussed in the following papers. Leung and Ko (2001) analyzed the dynamics and sound radiation of a perturbed slender vortex ring (non-deformable core) using vortex blob method. Their result for the most unstable mode agrees with the long-wavelength analysis of Widnall and Sullivan. With the numerical experiments, they proved that a vortex ring perturbed at the stable mode is a more efficient sound radiator than the one perturbed at the unstable mode. By comparing radial and transverse accelerations, they found that the polar radial acceleration contributes to the mechanism of the sound radiation. Ran and Colonius (2004) computed the transition and turbulent decay of an initially laminar fat vortex ring with its radiated acoustic field by DNS (direct numerical simulation) of unsteady compressible Navier-Stokes equations using a finite difference scheme. Ran and Colonius (2004) thought the turbulent vortex ring generates sound with a mechanism similar to that in an elliptical core shape of a vortex ring. By studying the velocity profile and vorticity contour inside the core during different stages, they found that the rotation of the core is induced by the mean vorticity inside the core region with the form of concentrated vorticity region rotating around the core center. They also studied the nonlinear state, which brings about significant growth of the lower azimuthal modes and leads to the strongest acoustic radiation.

1.2.2 Instability of Wake Vortex

It has been observed (Scorer and Davenport 1970) that the vortex wake does not decay by viscous diffusion, but, instead, develops a sinuous instability that leads to the formation of vortex rings. Two kinds of instabilities are known to occur in vortex systems: a long-wave and a short-

wave instability. The long wavelength is typically of the order of the distances between the different vortices of the wake and it was analyzed first by Crow (1970) on a single pair of trailing vortices. Later, Crow's linear stability analysis was extended to multiple pairs by Crouch (1997) and Fabre et al. (2002) using a vortex filament method. The evolution of the sinusoidal instabilities leads to vortex reconnection to form vortex rings. Once the rings have formed, the wake quickly degenerates into harmless, smaller-scale turbulence. The persistence of coherent flow depends mainly on the growth rate of the instability that precedes the formation of vortex rings. With a linear perturbation analysis of a pair of trailing vortices, Crow (1970) found that the wavelength of the most unstable mode could be found from the ratio of the radius r_c of the vortex cores to their separation distance b_o. A result frequently used in his analysis is r_c/b_o=0.098 and the fastest growing mode of instability is symmetric with a wavelength of $8.6b_o$. Although both long-wave and short-wave instabilities are shown in Crow's analysis, Widnall et al. (1974) later pointed out that the short-wave results are spurious, because the expression for the self-induced rotation of these perturbations, based on Crow' calculations, is asymptotically valid only for long waves. The Crow instability under atmospheric turbulence conditions has been studied by many researchers: experimentally by Sarpkaya and Daly (1987) and numerically by Spalart and Wray (1996), Han et al. (2000) and Garten et al. (2001).

The short wavelength instability results from the stretching of perturbations, whose wavelength is typically of the order of the vortex core radius. The short-wave instability was discovered simultaneously by Moore and Saffman (1975) and Tsai and Widnall (1976). Later, this kind of instability is observed in both laboratory experiments (Leweke and Williamson 1998, Ortega et al. 2003) and numerical simulations (Orlandi et al. 1998, Zheng (2002), and Nomura et al. 2006). These papers identified this phenomenon as a manifestation of a cooperative elliptic

instability, which has a length scale comparable to the size of the vortex core size and a growth rate that can exceed that of the Crow instability. The growth of the short wavelength gives rise to secondary transverse vortex structures, which lead to rapid vortex pinching off and the transition to turbulence.

1.3 The Present Task

Previous efforts in wake vortex research were concerned with developing engineering prediction models for the wake vortex behavior in response to weather conditions in the lower atmosphere (Han et al. 2000, Zheng and Lim 2000). Although wake vortices usually do not leave a visible trail, they leave an acoustic trail. Scientists are studying the sounds that wake vortices make. More recently, a scheme for actively monitoring wake vortices has emerged by passively tracking the acoustic emissions from wake vortices (Hardin and Wang 2003). Researchers want to determine whether a wake vortex sensor that uses sound would be a helpful tool for airports. One of the key concerns is to determine whether there is a relationship between a sound signal and the hazard the wake represents and whether a reliable acoustic signal can be identified for tracking acoustic emission that wake vortices produce.

The possibility of actively monitoring wake vortices is currently under examination. For that purpose, before we go on, several issues need to be discussed. First, one may ask whether wake vortices generate sound every time. The answer should be positive because many observations of wake vortex sound have been made under a variety of conditions, and the flow related to wake vortices is highly unsteady, such as the unsteady motion of the vortices, vortex decay, vortex instabilities and breakdown, wake interactions with the ambient turbulence and stratification, ground effects, etc. Because of the unsteadiness in the flow field, the expectation is that sound emission would be unavoidable from wake vortices. Given the various scales at which

these multiple vortices interact with each other, it may also be anticipated that measured acoustic spectra emitted from the trailing wake would be broadband.

Second, one may wonder whether the acoustic signal is consistent and measurable, and also contains diagnostic information to indicate the state of the vortex system. It is known that the airspace around an airport is a noisy environment. Noise sources include those from engines, the air frame, and the atmosphere (such as wind noise), in addition to all the vortex wakes from airplanes. Therefore, the question should be answered from the perspective of what is unique to the wake vortex sound, in both the signal patterns and source mechanisms, as well as in the relation between the two. For the purpose of identifying a unique sound source mechanism, all of the unsteady flow structures mentioned in the previous paragraph could be candidates since each of them represents a unique fluid dynamic aspect pertaining to wake vortices. However, not all of them are capable of generating a reliable, repeatable and detectable acoustic signal. The studies to date have focused on experimental characterization (Alix et al. 2005, Booth and Humphreys 2005, Dougherty et al. 2004, Michel and Bohning 2002, Aiao and Michel 2000, Rubin 2005, and Wang et al. 2005)) while a rigorous analytical identification of the noise source that is consistent and unique to aircraft is lacking. Our present task is to start theoretical investigations on the sound generation mechanism and to identify consistent components of wake vortex noise.

There are only two possible ways to make a vortex system emit sound: the unsteady motion of the vortices and the change of their strength. A previous study (Zheng 2005) shows that related sound emission due to viscous background turbulence and stratification is of a low frequency nature, and the frequency depends on the circulation fluctuations and the vortex decay coefficient. However, field measurement data (Booth and Humphreys 2005, Michel and Bohning

2002, Wang et al. 2005) shows higher frequency contents (e.g., 20-300 Hz) from wake vortices, even when the wake vortices are out of ground effect. Therefore, the higher frequency emission source may be attributed to the unsteady vortex motion.

This research is intended to identify the source of the high frequency sound from an isolated vortex system that includes out-of-ground aircraft wake vortices and wake vortices in inviscid ground effects. While the currently identified decay mechanisms only produce low-frequency sound, the higher frequency emission source is attributed to the unsteady vortex motion. Tang and Ko (2003) identified two independent types of unsteady vortex motion that radiate sound: the vortex centroid dynamics and the smaller scale vortex core dynamics. Their analysis showed that the vortex core deformation tends to generate more high-frequency sound than the vortex centroid dynamics. Tang and Ko (2003) focused their studies on vortex systems where the unsteady vortex motions are due to leapfrogging, collision, or coalescence. These types of vortex interactions rarely happen in a fully developed aircraft wake vortex, probably not until the Crow instability (1970) occurs leading to the demise of wake vortices. Therefore, during the lifetime of a long-lived wake vortex system, the primary vortex-core dynamics is not driven by any of the above interactions. Rather, the unsteady core dynamics depends on the initial eccentricity during the roll-up process, the background shear, and the ground boundary effect. Addressing these issues is the concern of the current study. A Kirchhoff spinning-core vortex (Lamb 1975) model is thus used as a starting point for studying the wake frequency related to the core dynamics.

There may exist interactions between the wake vortex systems, wind shear and ambient turbulence that can sometimes be modeled as a primary vortex structure interacting with a secondary vortex structure. The ground effect, which possibly causes very low-frequency sound

emission with the vortex translational acceleration in an inviscid manner (Hardin and Wang 2003), is still able to produce complex unsteady fluctuations due to vortex induced ground-boundary-layer separation and thus needs to be considered.

However, the frequency related to the vortex core vorticity can possibly shift under straining field imposed on the vortex cores due to mutual induction, such as multiple vortex interactions and vortex instabilities. In a three-dimensional vortex system, sinusoidal instabilities, in a format of both long and short waves, can occur. These instabilities lead to a contorted vortex system with the vortex core structures significantly different from its original system before contortion. Sinusoidal instabilities at various length scales result in significant flow structure changes in vortex dynamics, and thus influence their radiated acoustic signals. Cases of a vortex ring and a pair of counter-rotating vortices are studied when they are undergoing both long- and short-wave instabilities. Both inviscid and viscous interactions are considered and effects of turbulence are simulated using LES (large eddy simulation) with sub-grid-scale models.

1.4 The Present Method

In order to investigate the sound generation by aircraft wake vortices, engineering models of the phenomena, based on the Lagrangian discrete vortex method are developed. Since aircraft wake vortices are inherently vortical in nature and the noise sources are mainly vorticity-generated pressure waves, the vortex method is, therefore, particularly well suited and very efficient in describing the fundamental fluid mechanics. As a result of compact vorticity source, the flow field can be split into an inner and an outer domain, and the flow within the outer domain can be considered irrotational. Also, to compute far-field noise, the assumption that

compressibility effects remain small and that the Mach number is low ($M << 1$) is often introduced.

After the vortex particle method is used to capture the acoustic emission from the wake vortices, we then conduct a spectral analysis of vortices field that have evolved into highly controlled states at later wake age using the developed simulation software and compare the specific characteristics with younger vortices in their columnar state. The acoustic signal in the far field is computed using acoustic analogy approximation Lighthill (1952). Finally, the simulation result is compared with a few common aircraft measurements of wake acoustics (Dougherty et al. 2004).

The vortex method reformulates the Navier-Stokes or Euler equations in terms of vorticitiy, discretizes the vorticity-containing regions and tracks the discretized vorticity elements or particles in a Lagrangian reference frame. The development and application of vortex methods for incompressible 2D or 3D flow are described in several reviews (Leonard 1980, Winckelmans et al. 1993, Winckelmans et al. 2005) and a book by Cottet and Koumoutsakos (2000).

The present numerical simulation starts from an unsteady two-dimensional flow, with the effects of wind and atmospheric turbulence incorporated later. In the simulation of three-dimensional flow, we capture the long-wave and short-wave instability effects and the vortex link/pinch process, and also show that the associated wavelengths are consistent with experimental observation.

The implementation of the vortex particle method enables the vortex core size in the simulation to remain tight in the aircraft wake. The essentially grid-free nature of the vortex particle method is itself an advantage, and the vortex particle method convects without numerical

dissipation. Also, classical vortex methods have the advantages of distributing vortex particles only in the regions where the vorticity field is nonzero and the rigorous treatment of boundary conditions at infinity.

Computational techniques for flow-generated sound can be classified into two categories. One is to perform direct numerical simulation (DNS) to resolve all flow scales including the small dissipative scales. However, because of its high computational cost, its use is limited to simple flow configurations at low to moderate Reynolds numbers. Another way is to obtain far-field sound by integral or numerical solutions of acoustic analogy equations using computed source field data. The method assumes that flow is at low fluctuating Mach numbers and the sound waves do not affect the flow in any significant way. The first acoustic analogy was presented by Lighthill (1952), who rearranged the exact continuity and momentum equations into a wave equation with a source term on the right-hand side.

A two-dimensional version of the equation was derived by Mitchel et al (1995) and later by Zheng et al. (2006) using a matched–asymptotic-expansion method for a discrete vortex system. The formulation proposed by Zheng et al. (2006) to compute two dimensional far-field acoustics is implemented in the present research.

To predict the far-field sound radiated by three-dimensional incompressible, low Mach number and vortical flow, a formulation presented by Howe (1975) is used in the study.

1.5 Organization of the Thesis

In Chapter 2, numerical simulations for a realistic wake consisting of a counter-rotating vortex pair with inviscid ground effects and shear flow are carried out using a two-dimensional vortex particle method. A far-field vortex sound formulation, based on asymptotic expansions, is developed to calculate the acoustic pressure from the wake vortices. A possible sound emission

mechanism of aircraft wake vortices has been identified by using both measurement data and theoretical results in the chapter.

In Chapter 3, the sound emission frequency of the unsteady vortex core due to interactions among multiple vortices is discussed in a vortex system such as a complicated aircraft vortex wake. The behavior of the influence, indicated by the ratio between the core size and the distance of the vortices, and the underlining vortex core dynamic mechanisms are investigated. A vortex particle method is used to simulate the vortex core dynamics in two-dimensional, inviscid and incompressible flow. Cases of co-rotating vortices and a multiple-vortex system composed of two counter-rotating vortex pairs are studied for applications to aircraft wake vortex sound.

In Chapter 4, we describe the dynamics and sound generation of a perturbed vortex ring using a three-dimensional vortex particle method. The three-dimensional vortex particle method from the literature (Leonard 1980, Winckelmans et al. 1993, Winckelmans et al. 2005) is modified, by adding a divergence term to the original evolution equation of vorticity strength to help capture the small magnitude of what produced by the sinusoidal perturbations. Numerical simulations of a steady viscous vortex ring and a perturbed vortex ring validate the treatment. In this chapter, both inviscid and viscous interactions are considered and effects of turbulence are simulated using hyper-viscosity sub-grid-scale (SGS) models for Large Eddy Simulation (LES). Sound radiated by a perturbed vortex ring is discussed for both of the stable mode and unstable mode of perturbation.

In Chapter 5, the modified 3-D vortex particle method coupled with SGS model is used to investigate the dynamics and sound production by a counter-rotating vortex pair under sinusoidal wave instability conditions. Both long wave and short wave instabilities are considered. A

nearest-neighbor-image method is implemented into the vortex particle method to work as a periodic boundary condition in the direction of the vortex axes (the z axis). The investigation of the mechanism of sound generation is focused on the core distribution (Gaussian and elliptic core) and inviscid and viscous effect with perturbation and without perturbation.

Conclusions and future extension of the study are discussed in Chapter 6.

In Appendix A, we derive a two-dimensional version of a far-field vortex sound formulation to calculate the acoustic pressure for a discrete vortex system. The derivation is based on a matched-asymptotic-expansion method, which matches the inner region to the outer region.

In Appendix B, a parallelization method using MPI (message passing interface), which is implemented in our current computational codes, is described. The method divides the particles among all the processes and organizes all these processes in a ring network.

In Appedix C, computational techniques for the two- and three-dimensional vortex particle methods are introduced. The computational procedures and the corresponding C++ codes are described.

2 Influence of Vortex Core on Wake Vortex Sound Emission

As a starting point, sound produced by a two-dimensional counter-rotating vortex pair is investigated in this chapter. The stretching effect in the axial direction is neglected for the 2-D wake vortex system. The purpose of this study is to focus on vortex core behaviors. In addition, ground effects and atmospheric conditions are also considered in this chapter. A vortex particle method is used to simulate the vortex core dynamics in the 2-D, inviscid, and incompressible wake vortex flow. This method is particularly suitable for a wake vortex system that is slowly varying in the axial direction, and is of high Reynolds number and low Mach number. A far-field vortex sound formula matched with asymptotic expansions is then used to relate sound emission to the vortex-core dynamics.

2.1 Basics of Vortex Particle Method for an Incompressible and Invicid Flow

After a flow field is discretized by vortex particles, each particle or blob represents a small material volume V_p and carries vorticity strength. The position of each material volume is denoted by $\mathbf{x}_p$. The local velocity field carries the material volume through $\mathbf{u}(\mathbf{x}_p(t),t)$. The vorticity strength of each particle represents the integral of the vorticity $\boldsymbol{\omega}$ over the material volume and it can be expressed as $\boldsymbol{\alpha}_p = \int_{V_p} \boldsymbol{\omega} dV = \boldsymbol{\omega}_p V_p$, where the vorticity $\boldsymbol{\omega}$ is defined as $\boldsymbol{\omega} = \nabla \times \mathbf{u}$. In a 2-D flow, the vorticity strength is actually the circulation around the surface area of each particle. Thus the position and the vorticity strength of each particle evolve according to

$$\frac{d\mathbf{x}_p}{dt} = \mathbf{u}(\mathbf{x}_\mathbf{p}, t), \tag{2.1}$$

$$\frac{d\boldsymbol{\alpha}_p}{dt} = \int_{V_p} (\frac{\partial \boldsymbol{\omega}}{\partial t} + \nabla \cdot (\boldsymbol{\omega}\mathbf{u}))dV = \int_{V_p} \frac{D\boldsymbol{\omega}}{Dt} dV + \int_{V_p} \boldsymbol{\omega} \nabla \cdot \mathbf{u} dV \,, \tag{2.2}$$

where the material derivative $D\boldsymbol{\omega}/Dt = \partial\boldsymbol{\omega}/\partial t + (\nabla\boldsymbol{\omega})\cdot\mathbf{u}$.

The evolution of vorticity strength (Winckelmans et al. 1993) can be obtained by substituting the incompressible, inviscid vorticity transport equation $d\boldsymbol{\omega}/dt = (\boldsymbol{\omega}\cdot\nabla)\mathbf{u}$ into Eq. 2.2, which gives

$$\frac{d\boldsymbol{\alpha}_p}{dt} = (\boldsymbol{\alpha}_p \cdot \nabla)\mathbf{u}_p \,. \tag{2.3}$$

The velocity is obtained as $\mathbf{u} = \nabla \times \boldsymbol{\Psi} + \nabla\varphi$ ($\boldsymbol{\Psi}$ is the stream function related to vorticity by a Poisson equation $\boldsymbol{\omega} = \nabla \times \mathbf{u} = -\nabla^2\boldsymbol{\Psi}$ and φ is a potential). Based on the Biot-Savart law, the Poisson equation may be solved with

$$\begin{aligned} \mathbf{u}(\mathbf{x},t) &= \int (\nabla G)(\mathbf{x},\mathbf{x}') \times \boldsymbol{\omega}(\mathbf{x}',t) d\mathbf{x}' \\ &= \int \mathbf{K}(\mathbf{x}-\mathbf{x}') \times \boldsymbol{\omega}(\mathbf{x}') d\mathbf{x}' \end{aligned} \,, \tag{2.4}$$

where the Green's function is $G(\mathbf{x}) = -\frac{1}{2\pi}\log(|\mathbf{x}|)$ for 2D and $G(\mathbf{x}) = \frac{1}{4\pi|\mathbf{x}|}$ for 3D. The Biot-Savart kernel is $\mathbf{K} = \nabla G = -\frac{X}{2\pi|X|^2}$ for 2D and $\mathbf{K} = \nabla G = \frac{-X}{4\pi|X|^3}$ for 3D.

Substituting the particle representation of the vorticity field $\boldsymbol{\omega}(\mathbf{x},t) = \sum_p \boldsymbol{\alpha}_p \delta(\mathbf{x}-\mathbf{x}_p)$ to Eq. 2.4 (δ is the delta function), one can obtain

$$\mathbf{u}(\mathbf{x}_p,t) = \sum_q \mathbf{K}(\mathbf{x}_p - \mathbf{x}_q) \times \boldsymbol{\alpha}_q(t) \,. \tag{2.5}$$

In the regularized version (to avoid singularities) of the vortex particle method, the particle representation of the vorticity field is taken as (Knio and Ghoniem 1990, Winckelmans et al. 1993, Winckelmans et al. 2005)

$$\boldsymbol{\omega}(\mathbf{x},t)=\sum_{p}\boldsymbol{\alpha}_{p}\xi_{\sigma}(\mathbf{x}-\mathbf{x}_{p}), \tag{2.6}$$

where $\xi_{\sigma}(\mathbf{x})=\sigma^{-d}\xi(\mathbf{x}/\sigma)$, d denotes the dimension and σ is a small parameter. In most of the literature (Knio and Ghoniem 1990, Winckelmans et al. 1993, Winckelmans et al. 2005), the parameter σ is called the blob radius of a regularized particle and the function $\xi(\mathbf{x})$ is called cut-off or blob function that satisfies $\int\xi(\mathbf{x})d\mathbf{x}=1$, and $\int x_1^{\alpha 1}x_2^{\alpha 2}\xi(\mathbf{x})d\mathbf{x}=0$ ($\alpha_1,\alpha_2\geq 0,\alpha_1+\alpha_2\leq r$, r is the order of accuracy). A general modified Biot-Savart kernel is also obtained as the convolution of $\mathbf{K}$ and ξ_{σ}, namely $\mathbf{K}_{\sigma}=\mathbf{K}*\xi_{\sigma}$ (* is a symbol of convolution). For a more complete discussion of choosing r, constructing ξ and $\mathbf{K}_{\sigma}$, it can be found in Beale and Majda (1985).

By use of the particle approximation, the field computation, thus, amounts to a summation over the elements, giving

$$\frac{d\mathbf{x}_{p}}{dt}=\mathbf{u}(\mathbf{x}_{p},t)=\sum_{q}\mathbf{K}_{\sigma}(\mathbf{x}_{p}-\mathbf{x}_{q})\times\boldsymbol{\alpha}_{q}(t). \tag{2.7}$$

By observing the term in the right-hand side of Eq. 2.7, one can see that for a vorticity-containing flow, a rigorous boundary condition of zero vorticity at infinity is automatically satisfied. This shows Eq. 2.7 accounts explicitly for the boundary condition at infinity for the vortictiy-containing flow even when the vorticity field is truncated at the boundary.

Therefore, for an incompressible and inviscid flow, the main task of the vortex particle method is to solve the two equations Eq. 2.3 and Eq. 2.7. We use numerical solutions of the systems that are second-order accurate such as Adam-Bashforth or Runge-Kutta schemes.

Notice that the method converges for regular vorticity fields as the number of particles is increased, provided that the cores of neighbor blobs or particles maintain overlapping: one

requires that $\sigma > h$ (Beale and Majda 1985), where h is a spacing size. The overlaping of particles is essential for the "communication" of information between the particles.

Specifically, for a two-dimensional flow, the vorticity only has one component (perpendicular to the velocity field); hence, the vorticity stretch term $(\boldsymbol{\alpha}_p \cdot \nabla)\mathbf{u}_p$ in Eq. 2.3 vanishes. Eqs. (2.3) and (2.7) are reduced to

$$\frac{d\mathbf{x}_p}{dt} = \mathbf{u}(\mathbf{x}_p, t) = \sum_q \alpha_q(t)\mathbf{K}_\sigma(\mathbf{x}_p - \mathbf{x}_q) \times \mathbf{e}_3, \tag{2.8}$$

$$\frac{d\alpha_p}{dt} = 0. \tag{2.9}$$

In our 2-D numerical implementation, the cut-off function $\xi(\mathbf{x}) = e^{-|\mathbf{x}|^2}/\pi$ is chosen and the corresponding modified Biot-Savart kernel is $\mathbf{K}_\sigma(\mathbf{x}) = -\dfrac{\mathbf{x}}{2\pi|\mathbf{x}|^2}(1 - e^{-|\mathbf{x}|^2/\sigma^2})$. The blob or particle radius is $\sigma = 2h$ (Eldredge et al. 2002).

As the simulation proceeds, particles move according to Eq. 2.7 (Eq. 2.8 in a 2-D flow), and the requirement of overlap of the particle core does not remain satisfied. Due to that, the Lagrangian methods lose their accuracy quickly. So particles must periodically be redistributed or remeshed to a regular lattice ($h \times h$) in order to maintain the convergence requirement of vortex methods that preserve particle overlap. The convergence of the vortex particle method was generalized by Beale and Majda (1982). The error in the particle method does grow with time. The growth can be remedied by periodic remeshing, which introduces dissipation. However, a difficulty that occurs in dealing with the redistribution is to decide when to apply it. No clear criterion existed. To best preserve particle overlap, it is better to redistribute frequently (Ploumhans et al. 2002).

Two of the most widely used interpolation kernels, Λ_3 and $M_4^{'}$, are often implemented in vortex particle methods (Cottet and Koumoutsakos 2000) as the redistribution schemes. However, as mentioned by Eldredge et al. (2002), extra cares must be taken when applying the interpolation kernel for a flow field related to the acoustic field, which is very sensitive to the smallest errors. Since we are also concerned with the acoustic calculation, we follow the sixth-order kernel derived by Eldredge et al. (2002), given by

$$W(x_1, x_2) = \frac{1}{\pi}\left(\frac{15}{8} - \frac{5x_1^{\,2}}{2} + \frac{x_1^{\,4}}{2}\right) \cdot \left(\frac{15}{8} - \frac{5x_2^{\,2}}{2} + \frac{x_2^{\,4}}{2}\right) \cdot e^{-(x_1^2 + x_2^2)}. \tag{2.10}$$

Thus, new vorticity strength is acquired through

$$\tilde{\alpha}_p = \sum_q W_\varepsilon(\tilde{\mathbf{x}}_p - \mathbf{x}_q) V_q \alpha_q, \tag{2.11}$$

where $\tilde{\mathbf{x}}_p$ is the new particle position, $\mathbf{x}_q$ is the old particle position, V_q is the old particle volume, and $W_\varepsilon(\mathbf{x}) = W(\mathbf{x}/\varepsilon)/\varepsilon^2$ is the interpolation kernel scaled by the interpolation radius $\varepsilon = 1.7h$ (Eldredge et al. 2002). It is important that the vorticity strength does not change appreciably during remeshing. By enforcing the conditions on the integral moments of W, the discrete moment conditions (e.g. $\sum_p W(X_p) = 1$) are nearly satisfied.

2.2 Effects From Wind Shear

It can be argued that under realistic atmospheric conditions, wind shear and turbulence in the form of rotational straining fields can impose significant effects on the wake vortex-core dynamics. There are several ways to simulate these effects. One way is to represent the background field with the vorticity field and directly simulate the wake vortices along with the background vortices. Although this method is able to directly simulate the interactions between

the background shear and the wake vortices, it is computationally expensive because a large number of vortices need to be distributed all over the computational domain to represent the background flow. Another easy way to simulate these effects under wind shear is to split the wake vortices from the background flow and avoid expensive direct computations of the interaction between background shear and the wake vortices. This is derived as follows. For the vorticity transport equation of 2-D inviscid incompressible flow,

$$\frac{D(\overline{\omega}_z + \omega_z)}{Dt} = \frac{\partial(\overline{\omega}_z + \omega_z)}{\partial t} + ((\overline{\mathbf{u}} + \mathbf{u}) \cdot \nabla)(\overline{\omega}_z + \omega_z) = 0, \tag{2.12}$$

where the flow variables are split into the background flow $(\overline{\omega}_z, \overline{u})$ and the induced part by wake vortices (ω_z, u). Neglecting the influence from the wake vortices on the background flow, the background flow itself satisfies

$$\frac{D(\overline{\omega}_z)}{Dt} = \frac{\partial(\overline{\omega}_z)}{\partial t} + (\overline{\mathbf{u}} \cdot \nabla)\overline{\omega}_z = 0. \tag{2.13}$$

Substituting Eq. (2.12) into Eq. (2.11) leads to

$$\frac{D\omega_z}{Dt} = \frac{\partial \omega_z}{\partial t} + ((\overline{\mathbf{u}} + \mathbf{u}) \cdot \nabla)\omega_z = -(\mathbf{u} \cdot \nabla)\overline{\omega}_z. \tag{2.14}$$

If we only consider a constant-shear cross flow, Eq. (2.13) then becomes

$$\frac{D\omega_z}{Dt} = \frac{\partial \omega_z}{\partial t} + ((\overline{\mathbf{u}} + \mathbf{u}) \cdot \nabla)\omega_z = 0. \tag{2.15}$$

Therefore, the wake vortices can be treated as a pair of vortices transported at a velocity of background wind plus the induced velocity due to wake vortices. The vortex particle method can be easily implemented as

$$\frac{d\mathbf{x}_p}{dt} = \overline{\mathbf{u}}(\mathbf{x}_p, t) + \mathbf{u}(\mathbf{x}_p, t) = \overline{\mathbf{u}}(\mathbf{x}_p, t) + \sum_q \alpha_q(t)\mathbf{K}_\sigma(\mathbf{x}_p - \mathbf{x}_q) \times \mathbf{e}_3, \tag{2.16}$$

$$\frac{d\alpha_p}{dt} = 0 \,. \tag{2.17}$$

2.3 Case Studies for Out-of-ground Vortex Wake

In this section, we describe the aircraft wakes actually consisting of a pair of counter-rotating vortices, which are illustrated below (Figure 2.1) and the vortices are the type of the Kirchhoff vortex model. The vortex pair has the same core a and circulation Γ. But the sign of their circulations is opposite. The span between the vortex pair is b. We view the region containing the vortex pair as a near-field region while the far-field position is denoted by $\boldsymbol{y}$. The direction angle of the far-field position is denoted by θ.

As mentioned in Section 1.4, the computational technique of acoustic analogy method for flow-generated sound is employed in the study because the method is to obtain far-field sound by integral or numerical solutions of acoustic analogy equations using the computed source field data or near-field data. Compared to direct numerical simulation (DNS), the method reduces computational cost a lot.

In the study, the 2-D vortex particle method is used to compute the region containing the counter-rotating vortex pair and a two-dimensional version of far-field sound formula for a discrete vortex system derived by Zheng et al. (2006) is implemented to compute the far-field acoustics. Detailed derivation of the formula is referred to Appendix A.

It should be noted that in the following numerical simulations, the far-field position $|\mathbf{y}| = 10$ and the angle $\theta = 90^{\circ}$.

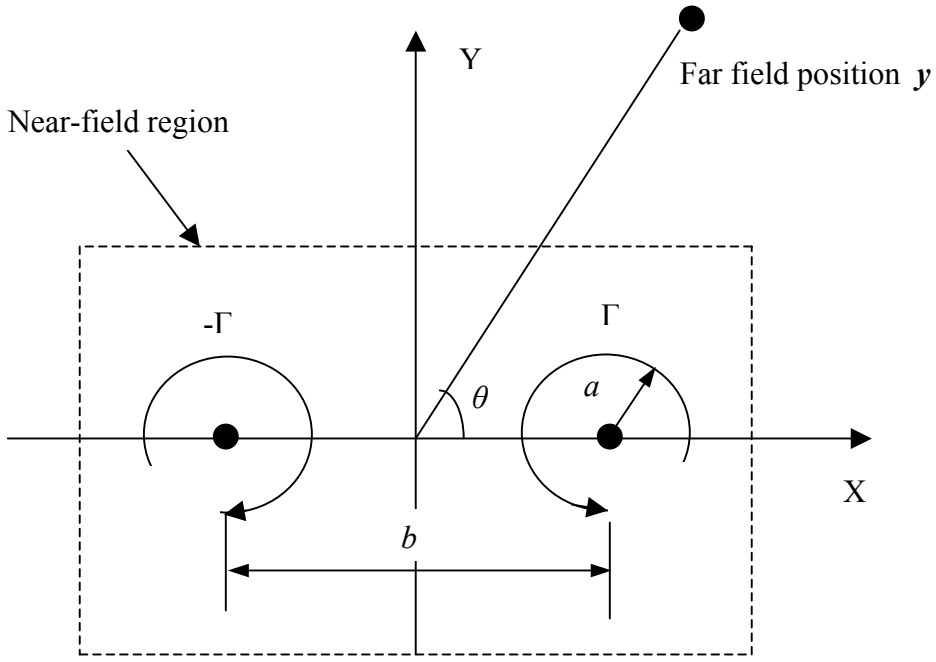

Figure 2.1 schematic of counter-rotating pair

2.3.1 Sound Emission from a Single Spinning Kirchhoff Vortex Core

The Kirchhoff vortex has a patch of uniform vorticity inside the ellipse and zero vorticity outside. It is an exact solution of the 2-D, incompressible, and inviscid flow equations (Lamb 1975). An almost circular Kirchhoff vortex has the ellipse defined by the polar equation for the radius of the vortex core:

$$R = a(1+\varepsilon\cos(2\theta - \omega t/2)), \tag{2.18}$$

where the major axis of the ellipse is $a(1+\varepsilon)$, the minor axis is $a(1-\varepsilon)$, $\varepsilon << 1$ and ω is the uniform vorticity in the core. Howe (2003) gave the acoustic pressure at $\omega r / c_0 \to \infty$ as

$$p \approx -\frac{\varepsilon}{8}\sqrt{\frac{2\pi a}{r}}\rho_o U^2 M^{3/2}\cos[2\theta - \frac{\omega}{2}(t-\frac{r}{c_o}) + \frac{\pi}{4}], \tag{2.19}$$

where c_o is the speed of sound, $U = a\omega/2$, $M_o = U/c_o$ and r is the distance between the far-field acoustic receiver location and the coordinate original. The ellipse rotates at an angular velocity

of $\omega/4$, which generates a quadrupole-type sound at a frequency of $\omega/4\pi$, as shown in Eq. (2.19). Eq. (2.19) also shows that for $\varepsilon = 0$, which is the case of a circular vortex patch in an unbounded potential flow, a Rankine vortex (Saffman 1995), for example, there is no emission because of the steady-state flow produced by a Rankine vortex. In the wake vortex system, the eccentricity is produced during the initial rollup process. An elliptical vortex resulting from shear-layer instability gave this evidence (Rogers and Moser 1992), because a major portion of the vortex wake is from the wing tip vortices resulting from a primary process of shear-layer instability. Other external effects such as wind shear or turbulence can also cause eccentricity in a wake vortex.

The analytical solution for the flow field of the Kirchhoff vortex is used to verify the results from the vortex particle method used in the study, and Eq. (2.19) is used as a base model to estimate sound emission frequencies from different types of aircraft and to verify the results from the far-field vortex sound formula presented in Appendix A.

2.3.2 *Case Studies for Out-of-Ground Vortex Wake without Background Flow*

Table 2.1 lists the major aircraft types and their configurations (related to the wake vortex behavior) whose wake vortex sound was measured during the 2003 phased array test at Denver International Airport (Dougherty etc. 2004, Wang etc. 2005). The wake sound emission frequencies are calculated based on the Kirchhoff vortex model (see Section 1.2 for the reason why the model is chosen as a starting point). The wake vortex span is estimated as 78.5% of a wing span according to a typical elliptical wing loading. The circulation is calculated approximately from a uniform aircraft landing weight at 80% maximum landing weight with fixed approach speed. While it is difficult to accurately estimate the vortex core size, a reasonable range of the core radius is from 1.5% to 2% wing span according to the field

measurement data (Delisi etc. 2003). A median core radius in between this range is selected as 1.65% of wingspan. With the relation of the vorticity $\omega = \Gamma / a^2$ and the angular frequency $\Omega = 2\pi f = \omega / 2$, the acoustic frequency of a Kirchhoff single vortex can be calculated as $f = \omega / 4\pi$. The lower bounds (**LB**), median and upper bounds (**UB**) frequencies correspond, respectively, to the core radii of 2%, 1.65% and 1.5% wing span. The last column of Table 2.1 is the results of computational simulation for the wake vortices modeled as a pair of counter-rotating vortices initially as Kirchhoff vortices with a median core size (1.65% wing span). The simulation procedure is explained in the next section. It can be seen in Table 2.1 that the acoustic frequencies from the numerical results are almost exactly the same as those predicted by a single Kirchhoff vortex model using Eq. 2.19. This is due to the fact that the two vortex cores are relatively far away because of the small radii of the cores. Therefore the mutual induction effect between the two vortices is relatively small and does not influence the vortex core rotating frequency. When the vortices are closer to each other, the ratio between the core size and the vortex distance influences the sound frequency, a point that was also made in Tang and Ko's work (Tang and Ko 2000), but needs to be further explored in future research.

The acoustic frequencies versus the wing spans shown in Table 2.1 is plotted in Figure 2.2. By grouping the aircraft types into small regional jets (**RJs**) and large jets, a general trend can be observed that shows that wake acoustics from large aircraft have an inverse relation between peak frequency and wing span. Small aircraft do not follow such a relation, which could be a reflection of a relatively wider range of aircraft design parameters for small aircraft than those for large aircraft. Comparisons of this predicted trend with the field measurement data also provide evidence that confirms the relation for the large aircraft.

In Figure 2.3, measured data are plotted for two cases of B737 and two cases of B757. Details of the measurement and data reduction procedure are described elsewhere (Wassaf et al. 2005, Wassaf et al. 2006). In these measurements, one nondimensional time unit is the approximate time for the vortex pair to descend one vortex span (Greene 1986) and is equal to $2\pi b_o^2 / \Gamma$, where b_o and Γ are respectively the initial vortex span and circulation. In each case, the data within the measurement period of the second non-dimensional time is selected for comparison because it has the full time history of the measured data and is considered more accurate from the measurement point of view, although the data at the first and the third non-dimensional time periods did show similar behaviors. The solid and dashed lines represent the wake vortex and background power spectral densities, respectively. The black dots indicate the predicted frequency peaks based on our numerical simulation values in Table 2.1 for the median frequency values. It can be seen from Figure 2.3 that near the peak frequencies there is a significant detectable wake power above background acoustic noise, although the measured power spectral levels shown here are related to the microphone-array gain from the beam-forming process (Wassaf et al. 2005, Wassaf et al. 2006) instead of the direct measure of sound-pressure levels. The measured and peak frequency values theoretically predicted by us have a very good agreement.

Figure 2.3 also shows that the measured B757 wake peak frequencies are lower than those of the B737 (Wassaf et al. 2005, Wassaf et al. 2006), which confirms the trend predicted in the calculations based on the Kirchhoff vortex model. These results suggest that the Kirchhoff vortex core could be the mechanism responsible for the peaks observed in the measured spectra. It should be pointed out that the comparisons of experimental results with the theory should focus on the trend, instead of the absolute values, since the theoretical calculation requires input

parameters that are very often not easily measured with high accuracy, such as the vortex span, core size and shape.

		Wing span b_o	Wake vortex span b	Circulation Gamma	Min Core Radius 1.5%b	My Core Radius 1.65% b	Max Core Radius 2%b	LB Acoustic Freq. (single)	Median Acoustic Freq. (single)	UB Acoustic Freq. (single)	Half of vortex span L	Maximum rotating speed	Numerical median Freq. (pair)
		(m)	(m)	(m^2/s)	(m)	(m)	(m)	(Hz)	(Hz)	(Hz)	(m)	(m/s)	(Hz)
Airbus	A318	34.15	26.82	252.68	0.51	0.56	0.68	13.74	20.18	24.42	13.41	71.38	20.17
	A319	34.15	26.82	265.77	0.51	0.56	0.68	14.45	21.23	25.69	13.41	75.08	21.22
	A320	34.15	26.82	274.72	0.51	0.56	0.68	14.94	21.94	26.55	13.41	77.61	21.93
	A321	34.15	26.82	266.76	0.51	0.56	0.68	14.50	21.31	25.78	13.41	75.36	21.30
	A343	60.06	47.17	458.12	0.90	0.99	1.20	8.05	11.83	14.31	23.59	73.58	11.82
Boeing	B717	28.35	22.27	235.57	0.43	0.47	0.57	18.57	27.29	33.02	11.13	80.14	27.28
	B737	28.96	22.75	281.74	0.43	0.48	0.58	21.29	31.28	37.85	11.37	93.83	31.27
	B738	34.45	27.06	262.06	0.52	0.57	0.69	14.00	20.56	24.88	13.53	73.37	20.56
	B757	38.11	29.93	347.95	0.57	0.63	0.76	15.19	22.31	27.00	14.97	88.07	22.30
	B767	47.56	37.35	377.17	0.71	0.78	0.95	10.57	15.53	18.79	18.68	76.49	15.52
	B777	60.67	47.65	456.62	0.91	1.00	1.21	7.86	11.55	13.98	23.83	72.60	11.55
MD	MD80	32.93	25.86	240.32	0.49	0.54	0.66	14.05	20.64	24.98	12.93	70.40	20.64
	MD90	32.93	25.86	276.26	0.49	0.54	0.66	16.15	23.73	28.72	12.93	80.93	23.72
Regional	B190	17.68	13.89	70.93	0.27	0.29	0.35	14.38	21.13	25.56	6.94	38.69	21.12
	CRJ2	21.04	16.52	139.14	0.32	0.35	0.42	19.93	29.28	35.43	8.26	63.80	29.27
	BA46	26.22	20.59	283.17	0.39	0.43	0.52	26.11	38.36	46.42	10.30	104.18	38.35
	DH8B	25.91	20.35	144.55	0.39	0.43	0.52	13.64	20.05	24.26	10.18	53.81	20.04
	E120	25.91	20.35	101.14	0.39	0.43	0.52	9.55	14.03	16.97	10.18	37.65	14.02

Table 2.1 Aircraft types and configurations and estimated wake frequencies based on the Kirchhoff vortex model (measured data from Dougherty etc. 2004, Wang etc. 2005)

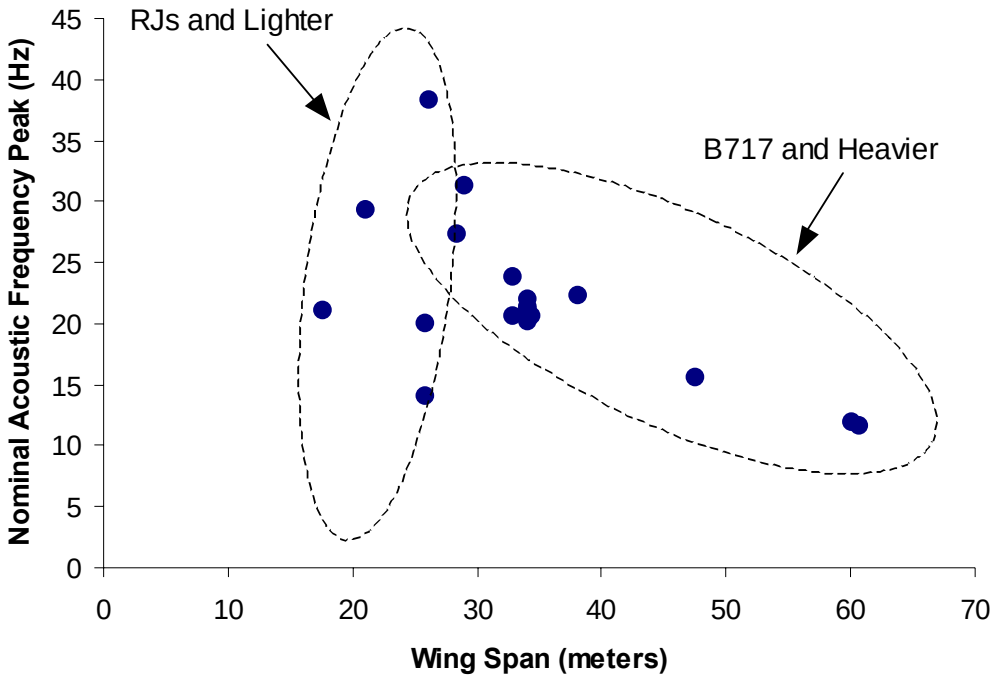

Figure 2.2 Acoustic frequencies vs the wing spans for different types of aircraft (measured data from Dougherty etc. 2004, Wang etc. 2005)

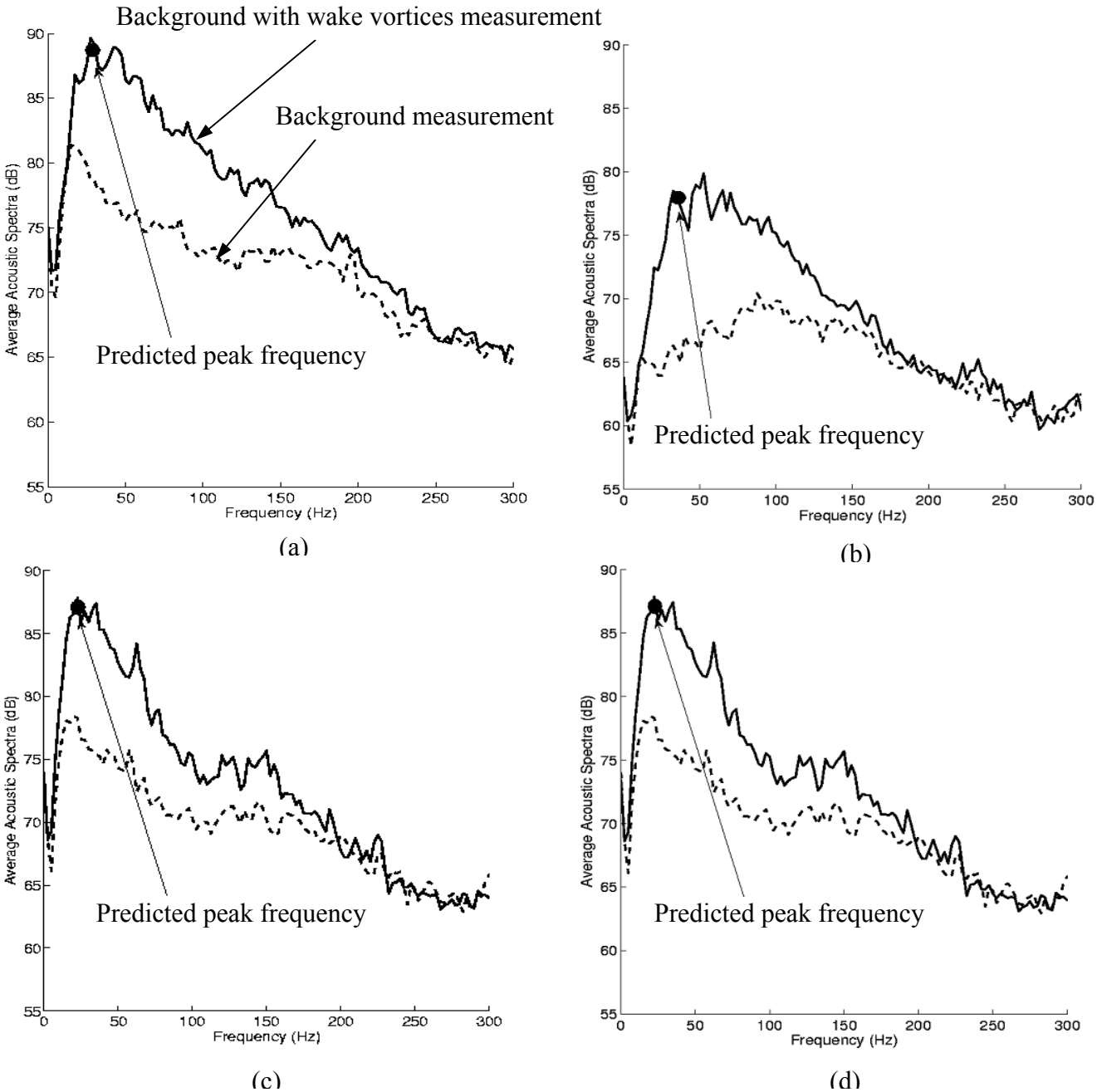

Figure 2.3 (a) B737-800, (b) B737, (c) B757, (d) B757. Measured wake acoustic spectra for B737 and B757, and comparisons of measured peak frequencies with the numerically predicted frequencies using the Kirchhoff vortex model (measured data from Dougherty etc. 2004, Wang etc. 2005)

2.3.3 Numerical Simulation Cases

Whereas the analytical solution of the Kirchhoff vortex model (Howe 2003) used in the previous sections is for a single vortex in an infinite domain, aircraft vortex wakes actually consist of a pair of counter-rotating vortices for which the analytical solution does not exist. In addition, ground effects and atmospheric conditions can further complicate the matter to pose a question on the predictions using the Kirchhoff vortex model. Therefore, for realistic vortex wake cases, numerical solutions are needed and discussed in this section.

Using the vortex half-span L as the characteristic length and the nominal maximum rotating speed at the outer edge of the vortex core, $U = a\omega/2$, as the characteristic velocity, the simulation equations can be nondimensionalized for computational purposes. Based on the characteristic length and characteristic speed, the other symbols are defined as follows: $\tilde{a} = a/L,\ \tilde{t} = tU/L,\ \tilde{f} = fL/U,\ \tilde{\omega} = \omega L/U$. Note that the tildes have been removed for brevity below. The simulation procedure is developed using the vortex particle method. At the beginning of the simulation, the initially specified Kirchhoff vortices have the parameters of $\omega = 47.69,\ \varepsilon = 0.05,\ a = 0.042$, for the median core-size (1.65% wing span) vortices. These parameters are chosen based on the theoretical formulations (Gertz et al. 2002): vortex core size is approximately 1.5% ~ 2.0% wing span b and the vortex span $b = \pi b_o/4$, which results in the vortex core size $a = 1.65\%b = 0.042L$. The initial uniform vorticity is obtained using $\omega = 2U/a = 47.69U/L$. The vortex particles are distributed on a grid mesh with grid size of $\Delta x = \Delta y = 1.68\times10^{-3}$ and a particle core parameter σ of $2\Delta x$. This gives 50 vortex particles in a nominal vortex-core diameter of $2a$. Such a fine grid solution selected in the simulation is to ensure proper resolution for the vorticty field to correctly capture the core rotation frequency. Simulation tests with lower resolution have shown that the acoustic frequency numerically shifts

to lower values. The required high resolution in this problem poses difficulties in using the Eulerian type of simulation with which only high-order accuracy schemes with high grid resolution are able to capture the frequency correctly (Muller and Yee 2002). Unfortunately, the small core radii in the wake vortices, in comparison to the distance between the vortices, limited the resolution required for the Eulerian Navier-Stokes simulation (Bohning et al. 2005). The reason is because on the one hand, the domain has to be sufficiently large to include the large distance between the two vortices so that the numerical domain-boundary effect is reduced to a minimal. On the other hand, the numerical grid size has to be sufficiently small to resolve the small vortex cores. This situation results in an excessive number of computational grid points that is difficult to accommodate even with today's state-of-the-art supercomputers.

It is noted that the small value of ε for the initial vortices is selected to satisfy the requirement of $\varepsilon << 1$ for a Kirchhoff vortex. As the vortices are allowed to freely evolve following the governing equations at the later times, the selection of this initial value does not need to be precise. There is no measured data available for determining the eccentricity of a vortex. While the wake vortices mostly result from shear-layer instability and multiple vortex merging, numerical simulations from our study of these phenomena have shown that the resultant vortices have a stable nominal eccentricity of approximately 0.1-0.2. This supports the argument that the sound mechanism described here is persistent.

The size of the time step used is Δt = 5.1465 e-3, which is equal to 10T/512, where T is the oscillation period of a single Kirchhoff vortex equal to $4\pi / \omega$. By carrying out a simulation of 512 time steps, we cover a time history of 10 periods. This time step is sufficiently small to resolve the frequency content related to the core vorticity in this case. During the simulation, re-meshing is done at each time step.

For modeling the wake vortex system, a counter-rotating vortex pair composed of two opposite-sign Kirchhoff vortices is used as the initial condition to represent the vortex wake out of ground effect. For in-ground-effect cases, the effect of an image pair of the wake vortices at the other side of the ground boundary is included to represent the inviscid ground effect. Effects of wind shear are also simulated under moderate and strong shear conditions to be discussed later in this section. In these different simulation cases, different domain sizes and moving domains are used to maintain a proper spatial resolution around the vortex core. In each case, the meshed domain that covers the vortex core is at least twice the core size, in order to ensure that the vorticity particles distributed on the mesh sufficiently include all of the vorticity fields in the core region.

Figure 2.4 is our numerical simulation result of the history of vorticity contours for interactions of a pair of wake vortices not in ground effect. Notice in this figure large vortex cores are used to illustrate their forms and the domain size shown is truncated from the real domain used in the simulation for illustration purposes. The history corresponds to a half period of the Kirchhoff vortex rotation. The light-color vortex is a counterclockwise vortex with its elliptical core also rotating counter-clockwise, and the dark-color vortex is a clockwise vortex with its elliptical core also rotating clockwise. Based on the fact that a single Kirchhoff vortex radiates a peak frequency due to the elliptic shape, it can be seen that it is this asymmetric "churning" effect of the solid-body like rotation motion of the elliptical-shaped vortex cores in Figure 2.4 that causes the unsteady fluid flow responsible for the far-field acoustics. This effect, caused by the eccentricity in an elliptical vortex core, is essential to the generation of an acoustic signal, because a perfectly round vortex does not produce sound, as stated previously in Section 2.4.1. Again, although the initial elliptical vortex cores are allowed to deform in the later times,

the basic elliptical shapes persist throughout the whole history, producing a persistent sound source.

Whereas Eq. 2.19 gives acoustic pressure from a single Kirchhoff vortex, for a system of discrete vortices such as the wake vortex system, an extended far-field acoustic pressure formula is needed to attribute its source to the near-field unsteady interactions of multiple vortices. A matched-asymptotic-expansion method (Kao 2002, Zheng 2005) has been used that matches the inner region of incompressible vortex flow to the outer region of acoustic field. Whereas previous research only considered the dipole-type sources, in the current vortex core problem only quadrupole noise is generated as shown in Eq. 2.19. Therefore, a higher order expansion than those previously derived (Kao 2002, Zheng 2005) is needed for the near field. The detailed derivations of the equations used for the far-field acoustic pressure calculation for a discrete vortex system are provided in Appendix A. In the far-field acoustic pressure calculation in the simulation, Eq. A11 in Appendix A is used. For the purpose of this study, the far-field location for calculating acoustic pressure is placed at a distance of 10 characteristic lengths (r = 10) in the fly-over direction (θ = 90 deg) under the wake vortex pair. A nominal Mach number of 0.27 is specified in the calculation.

Figure 2.5 compares the simulated dimensionless spectrum of the far-field acoustic pressure calculated using Eq. A11. It should be noted that in several cases considered here, the second quadrupole term in Eq. A11, i.e., the $\Gamma_j(x_j^2 - y_j^2)$ term, turns out to be zero because of the vorticity symmetry in the flow field. However, in other more general cases when the symmetry no longer exists, this term is not zero. Figure 2.5 (a) compares the single Kirchhoff vortex with the counter-rotating vortex pair, and Figure 2.5 (b) compares the single Kirchhoff vortex with the counter-rotating vortex pair in ground effect. It can be seen that in all the cases,

there exists a significant peak at the dimensionless frequency of $f = 3.8$, which is exactly related to the vorticity value in the Kirchhoff vortex core as $f = \omega / 4\pi$, as shown in the analytical solution of Eq. 2.19. This means that in the vortex wake, the sound generation mechanism due to vortex core rotation is not influenced by the macroscopic vortex interactions, as long as the distances between the vortices are large in comparison with the core size.

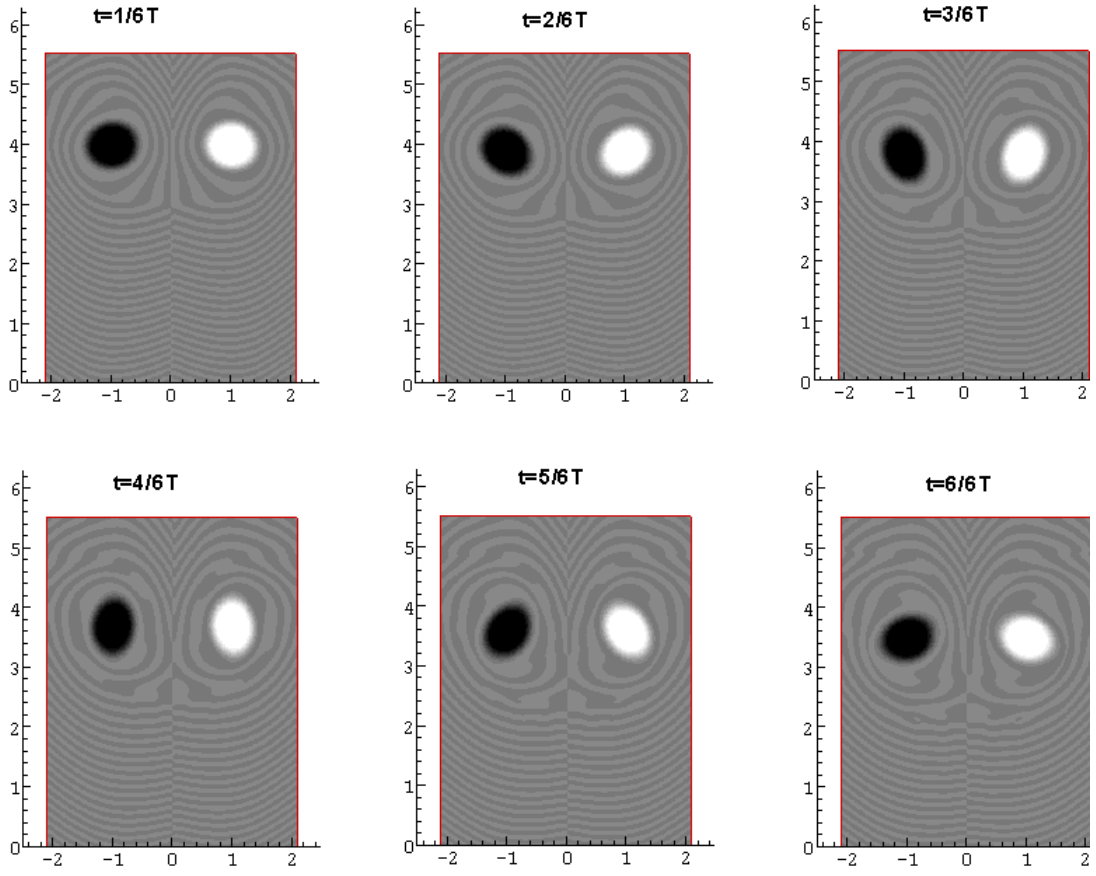

Figure 2.4 Illustration of the history of contours of the vortex wake represented by a pair of out-of-ground wake vortices initiated as a pair of counter-rotating Kirchhoff vortices.

Figure 2.6 is plotted to compare the effect of vortex core size. A case with an elliptical vortex core size of $a = 0.084$ is compared with the original core size of $a = 0.042$, with the same

vorticity of 47.69 inside the core. It can be seen that the peak frequency still remains at $f = 3.8$. The magnitude of the spectrum is increased due to the increase of the core size with the same vorticity, because the total circulation, which is initially equal to the vorticity times the core area, is increased. This phenomenon agrees with Eq. 2.19, where the frequency of the acoustic pressure only depends on the vorticity level $\omega/2$, and the magnitude of the acoustic pressure is increased due to the increase of the core size a. While Eq. 2.19 is for a single Kirchhoff vortex, the results in Figure 2.6 also shows that even when the core size is doubled in the wake vortices (with the ratio of core radius to vortex distance to be 0.084 now), the wake sound emission behavior (peak frequency) remains the same as that of a single Kirchhoff vortex.

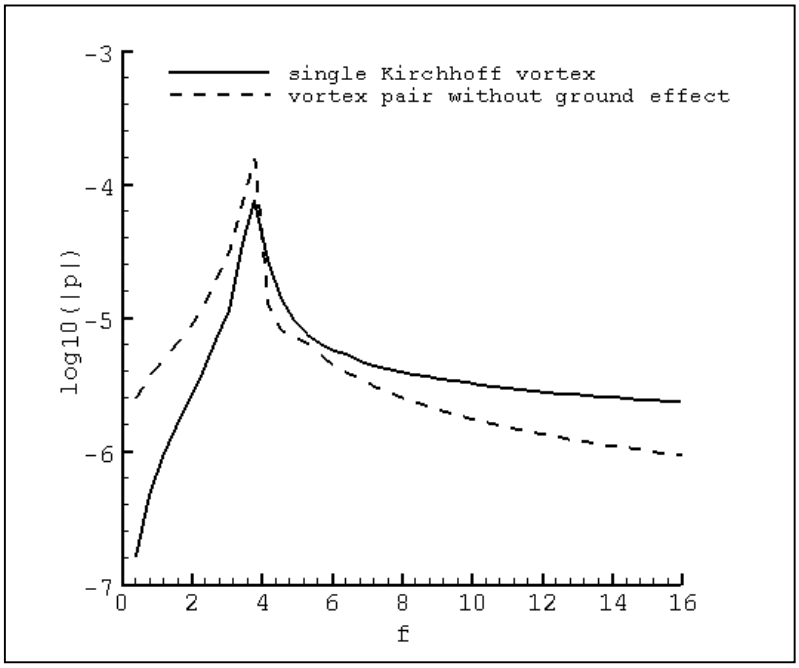

(a)

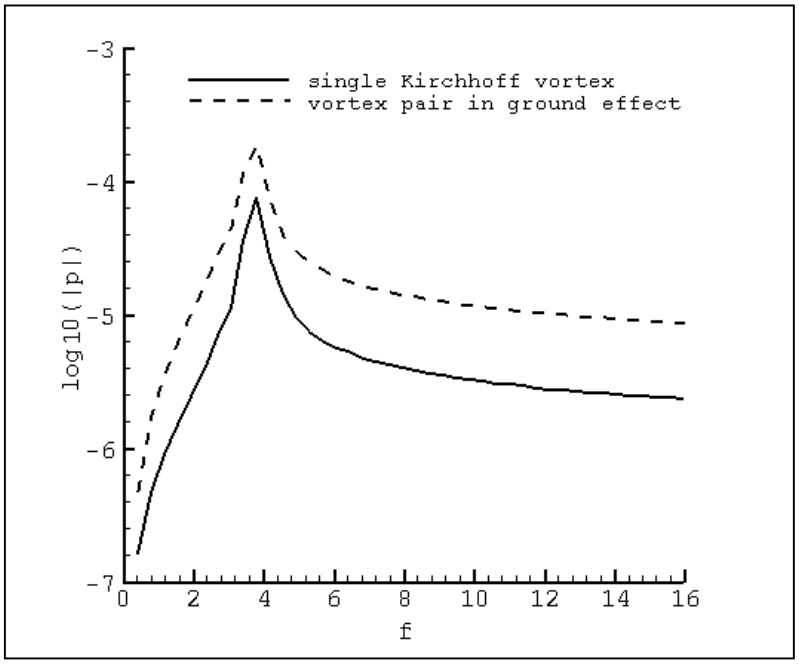

(b)

Figure 2.5 Comparison of acoustic pressure between that of a single Kirchhoff vortex and that of a pair of counterrotating vortices. (a) without the ground image; (b) with the ground image.

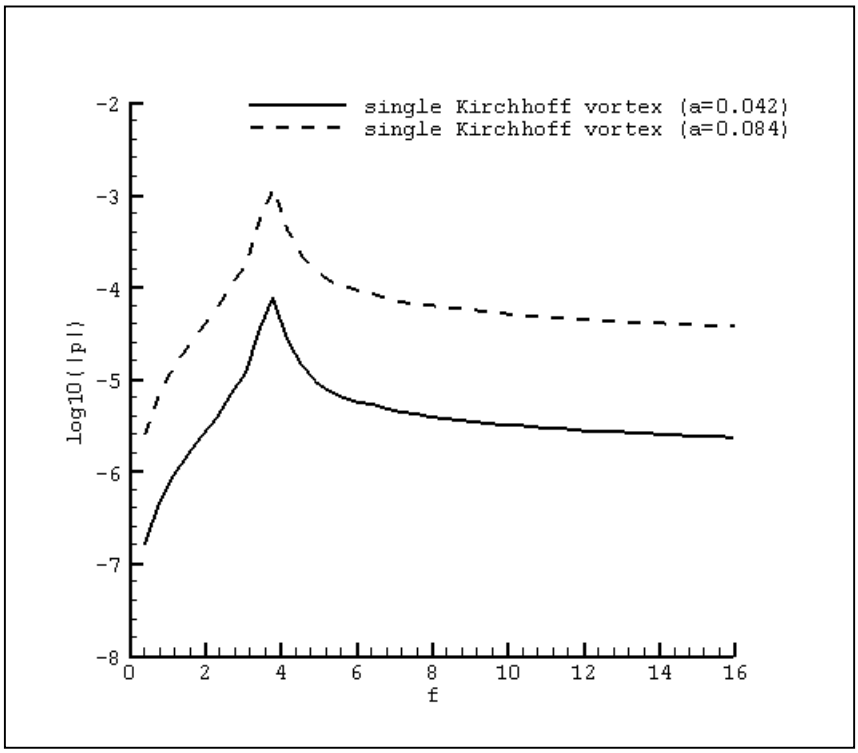

Figure 2.6 Comparison of the spectrum of acoustic pressure of two different core sizes of Kirchhoff vortex

It can be argued that under realistic atmospheric conditions, wind shear and turbulence, in the form of rotational straining fields, can impose significant effects on the wake vortex core dynamics. There are several ways to simulate these effects. One way is to represent the background field with a vorticity field and directly simulate the wake vortices along with the background vortices. While this method is able to directly simulate the interactions between background shear and the wake vortices, it is computationally expensive because a large number of vortices need to be distributed all over the computational domain to represent the background flow. Another way is to split the wake vortex flow from the background flow.

Figure 2.7 and Figure 2.8 compare cases of a wake vortex pair in a constant-shear background flow with that of a single Kirchhoff vortex. The vortices are initiated by the same parameters as mentioned before. In Figure 2.7 the level of shear vorticity is 0.01, and in Figure

2.8 it is 0.1. For a B757, these shear strengths represent a crosswind speed increase of 0.06 m/s per meter and 0.6m/s per meter respectively. Therefore for a B757, the case represented in Figure 2.7 is considered a moderate shear since the shear condition is very close to the cases of Run 7 and Run 9 in Ash and Zheng (1998). The case represented in Figure 2.8 is an unusually strong shear that can only occur locally and lasts a short period of time in the practical atmosphere. Figure 2.7 shows that under moderate shear, the dominant frequency again remains the same as that of the core rotation of a single Kirchhoff vortex. Under strong shear in Figure 2.8, the peak frequencies can be slightly shifted due to shear/vortex-core interactions. It seems one peak is slightly higher than the original frequency of a single vortex and the other is shifted slightly lower. These two peaks can be attributed to the two counter-rotating vortices in the vortex pair, one with strengthened vorticity and the other with weakened vorticity. While the total circulation remains the same in each of the vortices as guaranteed by Eq. 2.16, the vorticity level changes are caused by deformation of the cores. The background shear, if carrying vorticity of the positive sense in the simulation, deforms and expands the negative vortex core, and at the same time increases its eccentricity, resulting a lower-frequency but higher sound level peak as shown in Figure 2.8. The same shear tends to shrink the positive vortex core and decreases the eccentricity, resulting in a higher-frequency but lower sound level peak. Figure 2.8 supports the argument that each peak is caused by a corresponding Kirchhoff vortex core rotation. With other effects such as background turbulence, the two shifted peaks may get smeared into one broader hump such as that shown in the measured data in Figure 2.3.

It needs to be pointed out that the purpose of this study is to identify the most unique and consistent mechanism associated with the vortex (self-induced rotation of the elliptic core). This mechanism is related to the portion of the spectra that shows up as a hump above the background

in the measurement data as shown in Figure 2.3. It does not mean that there is no useful frequency content above or below such a hump. Although the higher frequency above the range of the rotating core frequency can be used and does show up in the source localization process (Booth et al. 2005, Michel and Bohning 2002, Wang et al. 2005, Wassaf et al. 2006), the acoustic energy is weak compared to that of the core-dynamics based mechanism, and it does not appear to be consistently above the atmospheric noise background.

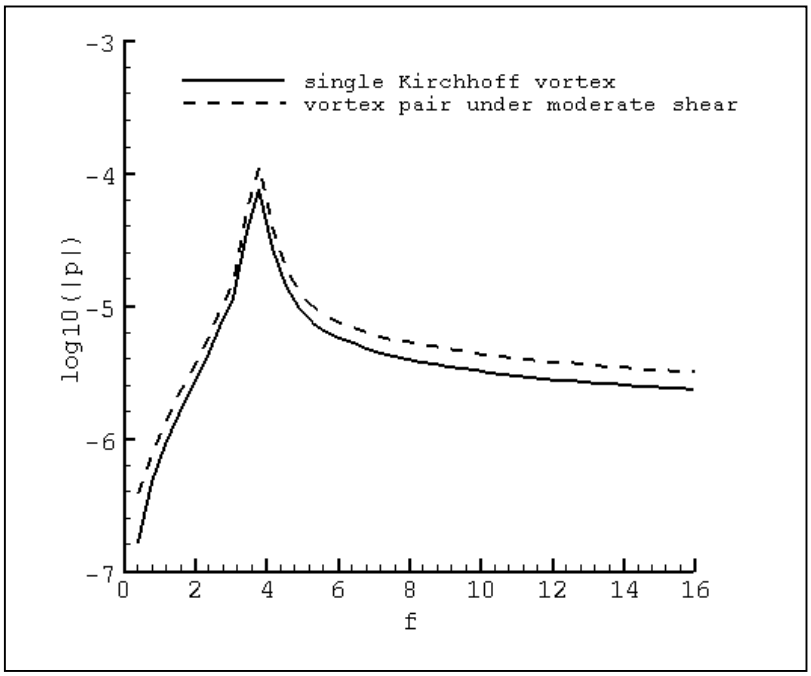

Figure 2.7 Comparison of dimensionless acoustic pressure spectra of the wake vortex pair under a moderate constant shear with that of a single Kirchhoff vortex.

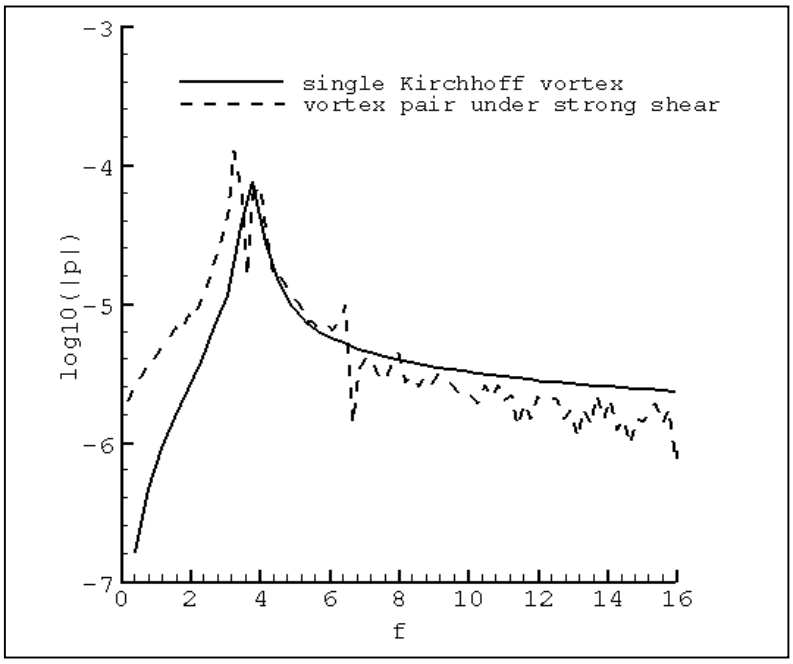

Figure 2.8 Comparison of dimensionless acoustic pressure spectra of the wake vortex pair under a strong constant shear with that of a single Kirchhoff vortex.

2.4 Summary and Discussion

Both measurement and theoretical results indicate a mechanism of sound emission of aircraft wake vortices due to the self-induction rotation of the elliptic vortex core. There is a dominant frequency of sound pressure that matches the rotation frequency of a Kirchhoff vortex core rotation. Calculated results based on this mechanism using realistic aircraft configurations show that wake acoustics from large aircraft have an inverse relation between peak frequency and wing span. Small aircraft do not follow such a relation. By looking into a particular set of data for the B757 and B737, both the measurement and the calculation agree that the B757 wake peak frequencies are lower than those of B737. When the wake vortices are initialized by counter-rotating Kirchhoff vortices, numerical simulations based on the inviscid vortex particle method confirm that the frequency of the wake sound emission remains essentially the same as that of the classical Kirchhoff vortex, even under the influences of an inviscid ground effect and a moderate, constant-shear cross wind. These results suggest that the identified sound generation mechanism attributed to the vortex core dynamics should be a robust acoustic radiation mechanism, a promising wake indicative among a number of active sound generation processes involved in aircraft vortex wakes.

3 Frequency Dependence on Core Dynamics in Multiple Vortex Interactions

In Chapter 2, we studied the sound emission mechanism of aircraft wake vortices consisting of a counter-rotating vortex pair with ground effects and shear flow. In a vortex system with multiple vortices such as in a complicated aircraft vortex wake, the sound emission frequency of the unsteady vortex core is subjected to change because of interactions between the multiple vortices. Therefore, in this chapter, sound produced by the multiple vortex system is studied. The behavior of the influence, indicated by the ratio between the core size and the distance between the vortices, and the underlining vortex core dynamic mechanisms are investigated. The vortex particle method, which was described in Chapter 2, is used to simulate the vortex core dynamics in the two-dimensional, inviscid and incompressible flow. The flow field, in the form of vorticity, is employed as the source in the far-field acoustic calculation using a vortex sound formula. Cases of co-rotating vortices and a multiple-vortex system composed of two counter-rotating vortex pairs are studied for applications to aircraft wake vortex sound.

3.1 Basics of Frequency Dependence on Core Dynamics in Vortex System

It has been shown that vorticity in a vortex core directly relates to the frequency of a significant sound peak from an aircraft wake vortex pair where each of the vortices is modeled as an elliptic core Kirchhoff vortex (Zheng et al. 2007). This sound source results from an uneven distribution of vorticity impulse about the vortex center in an elliptic core. When an aircraft vortex wake is represented by such a vortex pair, the vortex core size is very small in comparison with the distance between the vortices. In this case, the peak frequency is the same as that of a single Kirchhoff vortex, equal to $\omega/4\pi$, where ω is the uniform vorticity in the Kirchhoff vortex

core (Howe 2003). In a vortex system with multiple vortices, the peak frequencies can shift due to different straining field imposed on the vortex cores. From theoretical deduction, Tang and Ko (2000, 2003) showed that, in any vortex system, the basic sound generation mechanisms can be attributed to the vortex core deformation and the vorticity centroid dynamics. By using the method of contour dynamics as the numerical simulation tool, Zabusky et al. (1979) and Pozrikidis (1986) found that the frequency of the high-frequency oscillation, which is associated to the unsteady core deformation, is proportional to the vorticity of the vortex. It is expected that, when the effect of straining from other vortices becomes insignificant, this frequency approaches the above-mentioned sound frequency of a single Kirchhoff vortex, as shown in Zheng et al. (2007).

In a vortex system with multiple vortices such as a complicated aircraft vortex wake, this Kirchhoff vortex frequency is subjected to change because of interactions among multiple vortices. An analogy (but with totally different physical mechanisms) may be similar to that between the Crow instability (Crow 1970) for a single vortex pair and the Crouch instability (Crouch 1997) for multiple vortex pairs. Particularly, when two vortices are close to each other, the frequency may change significantly, with the extreme case of coalescence of two vortices. Although it has been suggested that the ratio between the core size and the distance between the vortices influences the frequency of the sound due to vortex core dynamics (Tang and Ko 2003), the behavior of the influence and the underlined mechanisms have not been fully investigated.

Several numerical methods have been developed to simulate vortex merging (Mokry 2005, Orlandi 2007). For the purpose of investigating the related acoustic frequencies, a vortex particle method (Cottet and Koumoutsakos 2000) is used here to simulate the vortex core dynamics in the two-dimensional, inviscid and incompressible flow. The flow field, in the form

of vorticity, is employed as the source in the far-field acoustic calculation using a vortex sound formula (Zheng et al. 2007), similar to the two-dimensional version of Mohring (1978, 1979) and others (Howe 2003, Tang and Ko 2003, Kambe 1993, Muller 1998, Mitchell 1995, Knio 1995). This method has been used and verified in the cases of a single Kirchhoff vortex and a pair of counter-rotating vortices (Zheng et al. 2007). We first look at a co-rotating vortex pair to investigate the effect of the mutual induction between the two co-rotating vortices on the peak frequency of sound due to vortex core rotation. Then a number of different configurations of a multiple-vortex system composed of two counter-rotating vortex pairs are studied for the applications to aircraft wake vortex sound.

3.2 Computational Formulation

We use the characteristic parameters related to the configurations of realistic wake vortices to non-dimensionalize the flow simulation equation. Since only the relative values are of the interest in this study, the reason for this selection is merely for the purpose of easy interpretation of some of the results when a practical aircraft vortex wake is concerned.

Using the vortex half-span as the characteristic length and the nominal maximum rotating speed at the outer edge of the vortex core, $a\Omega/2$, as the characteristic velocity, the simulation equations can be nondimensionalized for computational purposes. All of the vortices in the simulation are initially specified as almost-circular Kirchhoff vortices with the ellipse defined by the polar equation

$$R = a(1+\varepsilon\cos(2\theta - \omega t/2)), \qquad (3.1)$$

where the major axis of the ellipse is $a(1+\varepsilon)$, the minor axis is $a(1-\varepsilon)$, and ε is selected as 0.05 (<<1). Based on the characteristic parameters, we have $a = 0.042$, and $\omega = 47.69$. With this value of vorticity in the core, the corresponding theoretical sound frequency for a single vortex is $\omega/4\pi$

= 3.79. This simplified initial condition fits our current interest of looking into the frequency effect. More complicated shapes of vortices (Norbury 1973, Pierrehumbert 1980) could also be specified if the actual magnitude of the sound level was concerned. Using the vortex particle method (Cottet and Koumoutsakos 2000), we distribute the vortex particles on a grid mesh with the grid size of $\Delta x = \Delta y = 1.5 \times 10^{-3}$ and a particle core parameter σ of $2\Delta x$ (Eldredge 2002). This gives 50 vortex particles along a nominal vortex core diameter of *2a* (see Fig. 1 in Appendix C). Such a fine grid solution is selected in the simulation to ensure proper resolution of the vorticity field in order to correctly capture the core rotation frequency.

In this study, we still use 2-D vortex particle method to simulate the near-field region containing vertical flow. The basics of the method are described in Section 2.1 and computational techniques of the method are described in Appendix C. The computation of far-field sound is based on the formula of Eq. A11 in Appendix A.

In the numerical simulation, σ, the vortex particle radius, is selected as $2\Delta x$ or $2\Delta y$, following a particle radius requirement specified by Beale and Majda (1982). The size of time step is $\Delta t = 1.0293 \times 10^{-2}$, which is equal to $5T/128$, where T is the oscillation period of a single Kirchhoff vortex equal to $4\pi/\omega$. This time step is sufficiently small to resolve the frequency content related to the core vorticity in this case.

With only the quadrupole source from the vortex core, the dipole terms (related to $\sin\theta$ and $\cos\theta$) in Eq. A11 in Appendix A are zero. The strengths of the quadrupole terms depend on $Q_1 = d[\alpha_j (x_j^2 - y_j^2)]/dt$ and $Q_2 = d(2\alpha_j x_j y_j)/dt$. The far-field location for calculating acoustic pressure in this paper is located at a distance of 10 characteristic lengths ($|\mathbf{y}| = 10$) at the directional angle of $\theta = 90^o$ (also see Fig. 2.1 and the following Fig. 3.1 about the far-field distance and the directional angle).

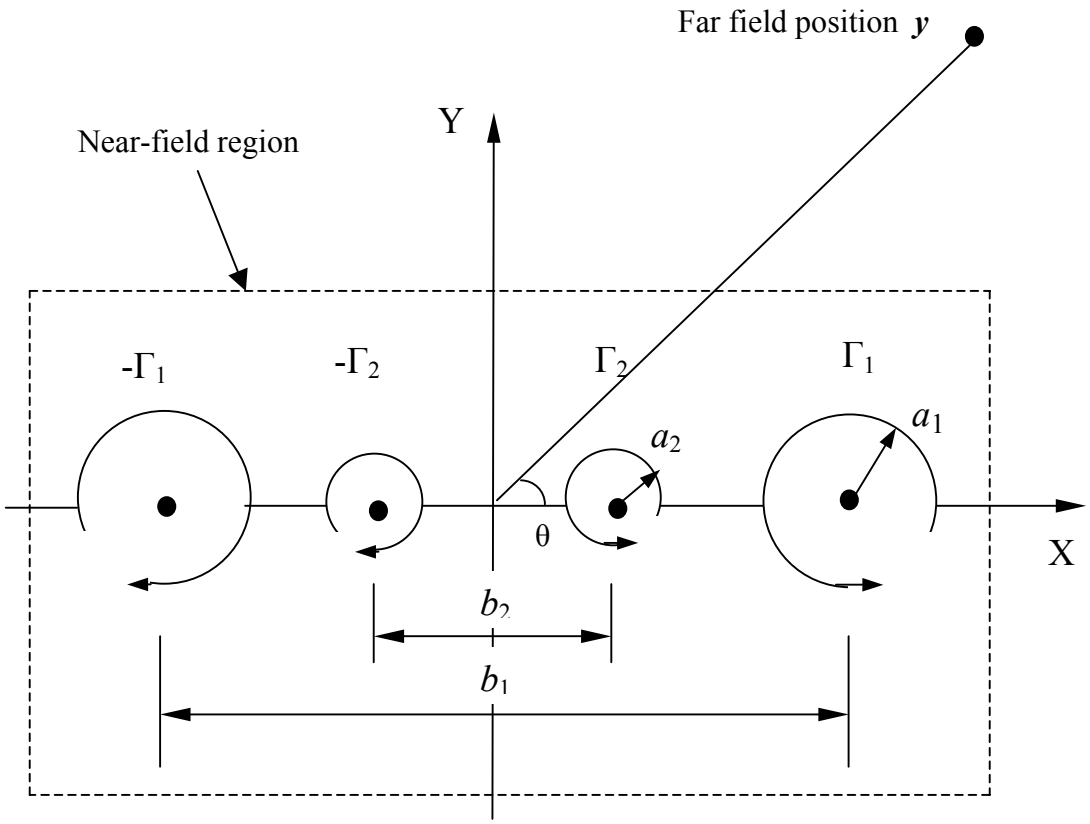

Figure 3.1 Illustration of the initial setup of the multiple vortex pair system.

In the following numerical results, Section 3.3.1 presents a result of two identical co-rotating vortices. The initial configuration of the vortex pair is the same as that in Fig. 2.1 while here the sign of circulation of the two vortices is the same. Section 3.3.2 describes a result related to two vortex pairs. The initial configuration is illustrated in Fig. 3.1.

3.3 Simulation Results

3.3.1 Two Identical Co-rotating Vortices

The merger of two identical co-rotating vortices is sometimes termed symmetric vortex merger (Melander et al. 1988, Waugh 1992). These cases are studied here to elucidate the effect of distance between the two vortices on the peak acoustic frequency resulting from the vortex

core rotation. Figure 3.2 is for a case when the distance, G, between the two co-rotating vortices is 0.5, with the ratio $\beta = G/a = 11.9$. Figure 3.2 shows the time histories of the source terms, Q_1 and Q_2. It shows that the two source terms are of the same amplitude with a phase shift. There are obviously two major frequency contents. The low frequency component is related to the circular motion of the vortex centers around one another, and the high frequency component is related to the core rotation with respect to its own vortex center. Figure 3.2(b) is the spectrum of the acoustic pressure magnitude. The two peak frequencies are clearly shown, with one at 0.1 and the other at 3.51. The angular speed for the circular vortex center motion, when point vortices are assumed, has an analytical expression of ω/β^2, and the acoustic pressure caused by that motion has a frequency of $2*\omega/(2\pi\beta^2) = \omega/(\pi\beta^2)$ (Howe 2003). For the parameters in this case, such a frequency is therefore approximately 0.1. The high frequency is close to the theoretical value of a single Kirchhoff vortex of 3.79.

When $G = 0.126$, with the ratio $\beta = G/a = 3$, within the theoretical merging criterion for co-rotating vortices (Saffman 1980), the two vortices are so close to each other that the vortex coalescence occurs. Figure 3.3 contains four snap shots of vorticity counters during the vortex coalescence. It can be seen that the two vortices follow the three-phase merging as stated by Orlandi (2007): first diffusion, convection, and second diffusion. Figure 3.3, at $t = 10\Delta t$, shows mostly the first diffusion, and later the contours at $t = 20\Delta t$ and $60\Delta t$ are depictions of the convective merging process, and finally at $t = 900\Delta t$ the snapshot represents a merged vortex to continue on to the second diffusion phase. This merging process is also represented in the histories of the source terms in Figure 3.4(a) where there is a transient process before the signal becomes periodic. Again as in Figure 3.2(a), the two source terms have approximately same behavior with a phase shift. The Fourier transformation in Figure 3.4(b) is processed after the

source terms become periodic. There is only one significant peak at the frequency of 3.04, close to but lower than the original single Kirchhoff vortex sound frequency. This is due to the enlarged core region of the final vortex as a result of the vortex coalescence.

A case with $G = 0.147$ results in $\beta = G/a = 3.5$, which is a little larger than the theoretical merging distance for co-rotating vortices with uniform core vorticity (Saffman 1980), but smaller than the merging distance for vortices with non-uniform core vorticity (Meunier et al. 2002). In this case, the vortex merging reaches a critical stage where the two vortices re-split again after touching, as shown in the snapshots of contours in Figure 3.5. This phenomenon was observed by Tsuboi and Oshima (1985). As in the non-merging case, there is an angular speed for the circular vortex center motion.

For the parameters in this case, this frequency is approximately 1.24. The high frequency, due to vortex core self rotation, still exists and is approximately 3.2, a bit lower than that of a single Kirchhoff vortex of 3.79. These two frequency components can be observed both in the time history of the quadrupole source terms, Figure 3.6(a), and in the far-field pressure spectrum, Fig. Figure 3.6(b).

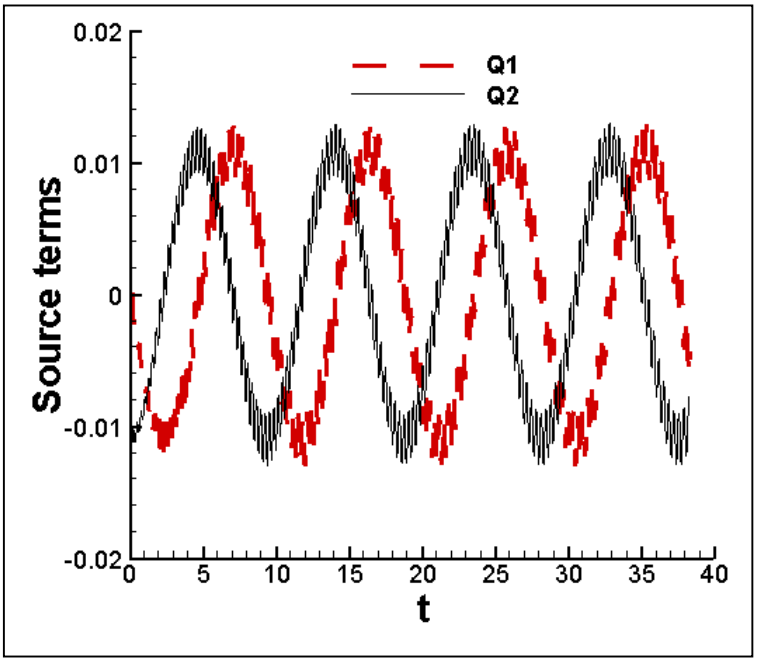

(a)

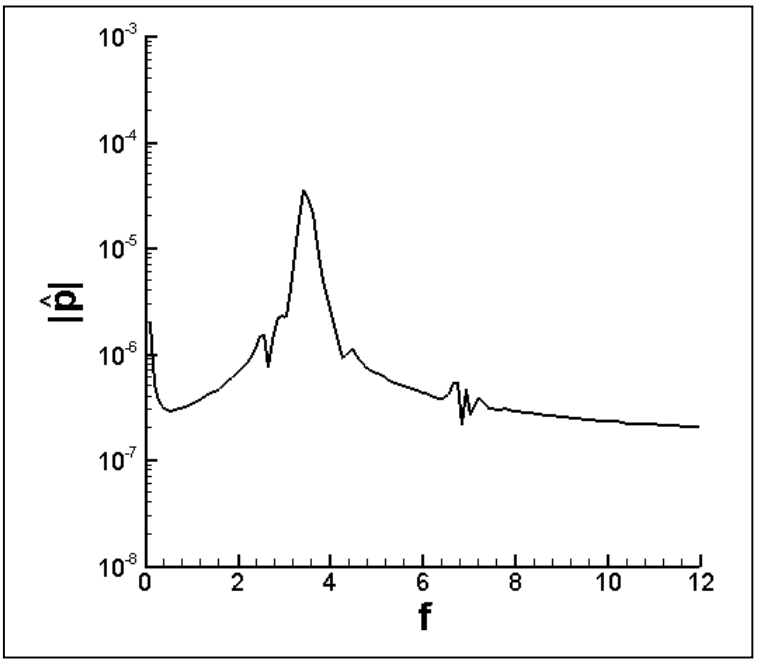

(b)

Figure 3.2 β = 11.9. (a) History of the quadrupole source terms in Eq. A11 in Appendix A generated by two identical co-rotating vortices. (b) Spectrum of sound pressure magnitude in the frequency domain.

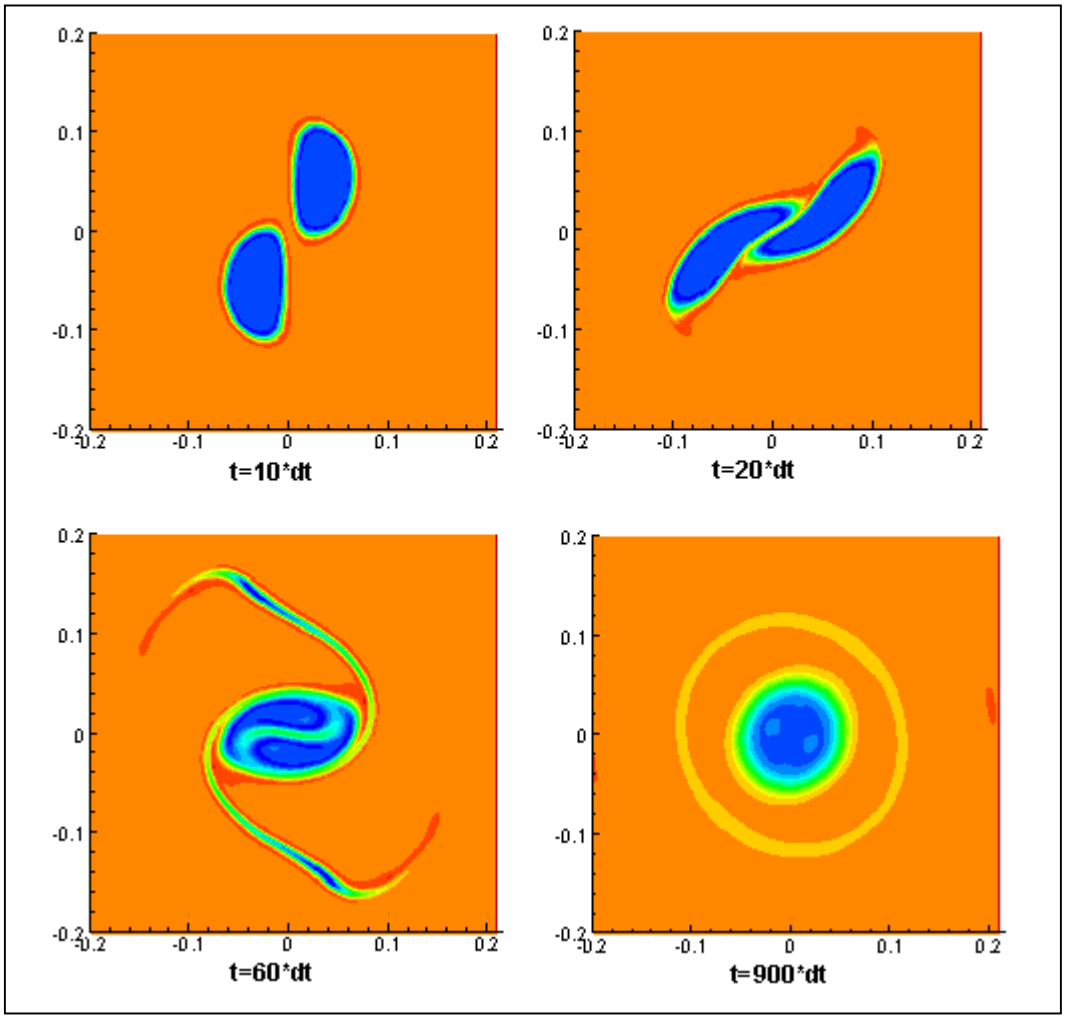

Figure 3.3 Snap shots of vorticity contours during the vortex merging process for $\beta = 3$.

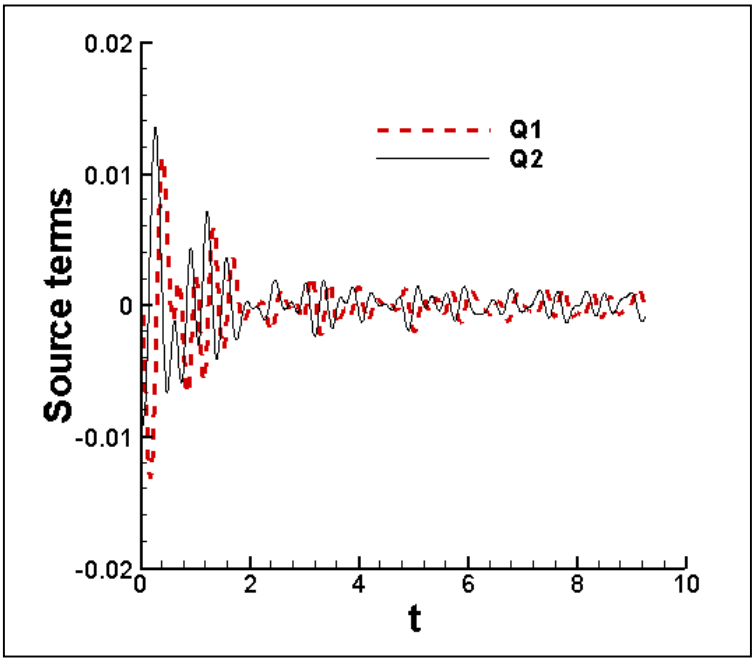

(a)

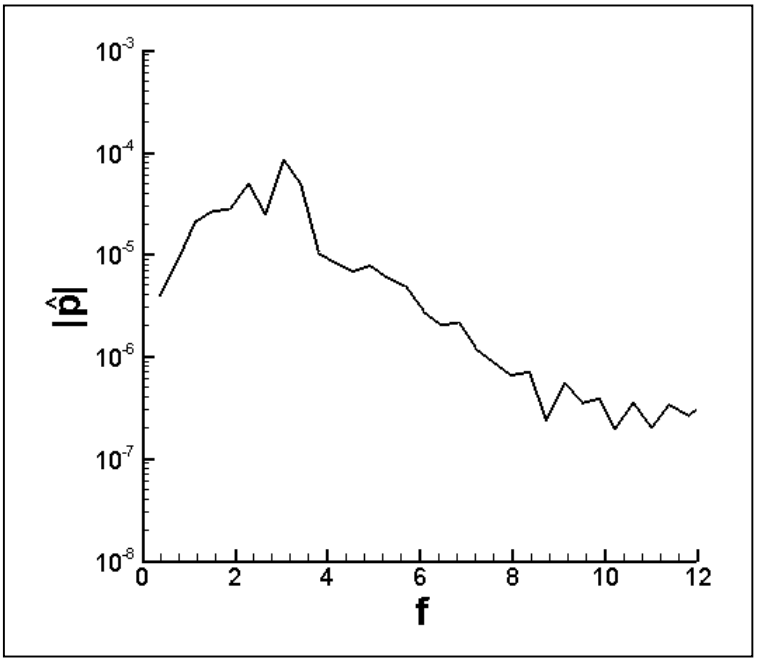

(b)

Figure 3.4 β = 3. (a) History of the quadrupole source terms in Eq. A11 in Appendix A generated by two identical co-rotating vortices. (b) Spectrum of sound pressure magnitude in the frequency domain.

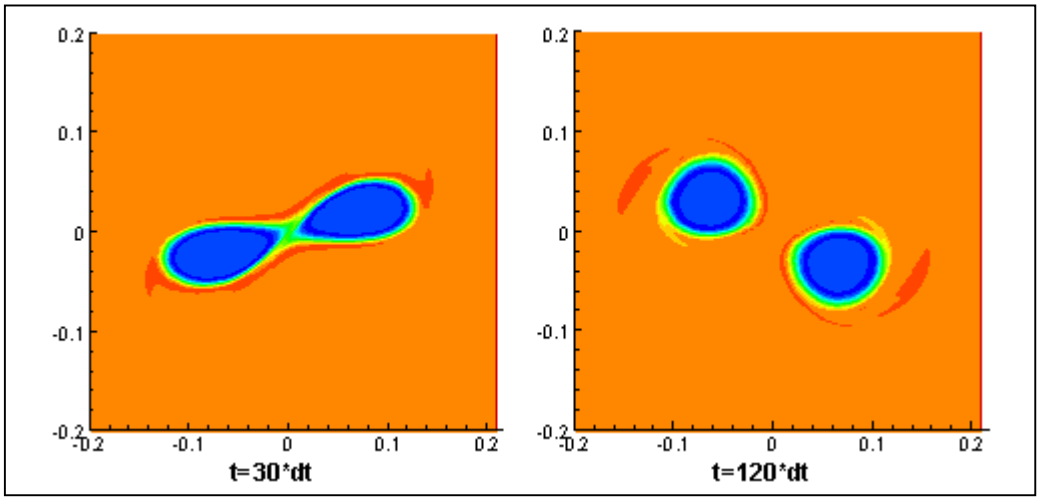

Figure 3.5 Snap shots of vorticity contours during the vortex merging process for β = 3.5.

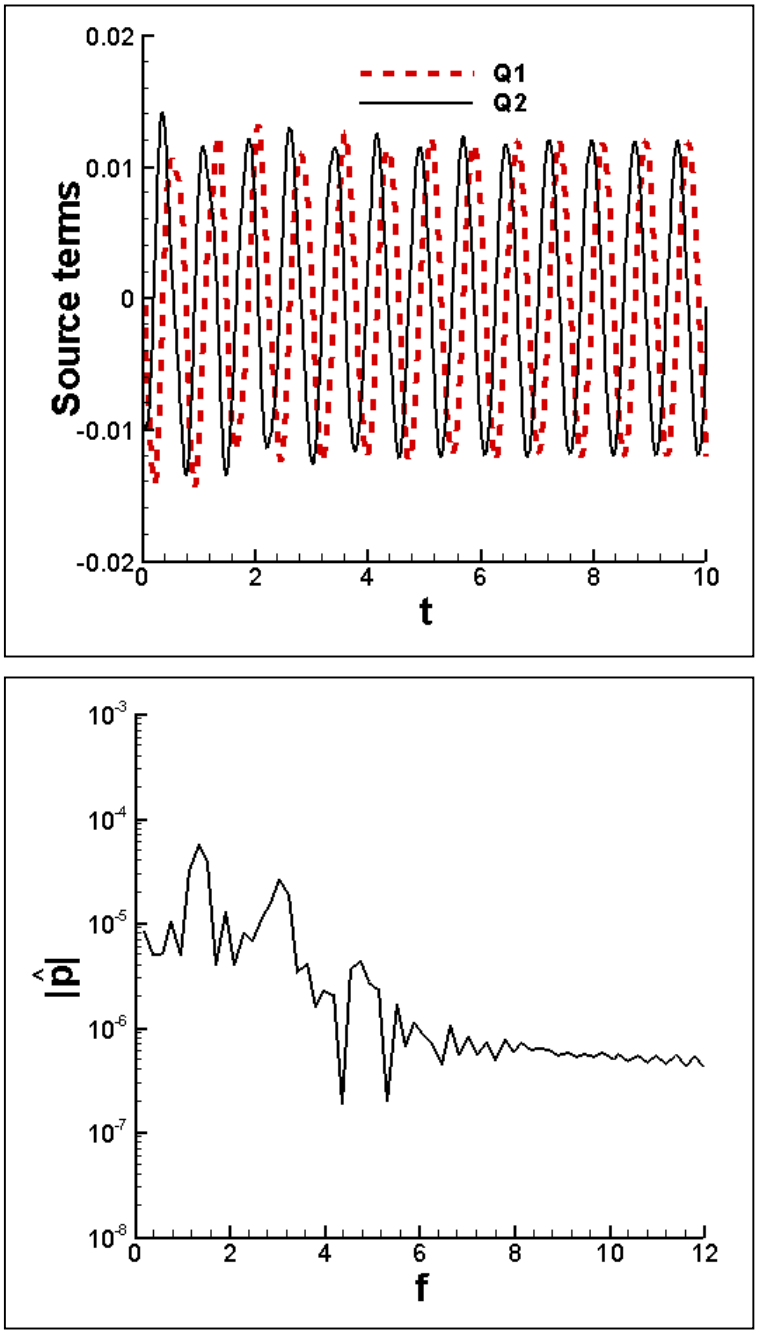

(a)

(b)

Figure 3.6 β = 3.5. (a) History of the quadrupole source terms in Eq. A11 in Appendix A generated by two identical co-rotating vortices. (b) Spectrum of sound pressure magnitude in the frequency domain.

3.3.2 Two Vortex Pairs

The same computational algorithm has been extended to simulate multiple vortex pairs. Two counter-rotating vortex pairs are simulated, with the initial configuration illustrated in Figure 3.1, which approximately represents an aircraft wake with multiple vortices. In the case of one inner and one outer counter-rotating vortex pairs, the Q_1 term turns out to be zero because of the vorticity symmetry in the flow field.

Two non-merging cases are first presented. The same characteristic parameters are used as in Section 2.3.3. The vortex span of the outer vortex pair, b_1, is 2. Figure 3.8 is for the case with $b_2/b_1 = 0.5$, $\omega_1 = \omega_2 = 47.69$, $\Gamma_2/\Gamma_1 = 0.5$, $(a_2/a_1)^2 = 0.5$, and $a_1 = 0.042$. That is, the vorticity is the same in the two vortex pair, and the circulation of the inner pair is half of that of the outer pair. Because of the smaller core size of the inner vortex pair, the grid size is reduced to $\Delta x = \Delta y = 1.5 \times 10^{-3}$ to accommodate the resolution requirement. Figure 3.9 is for the case with $b_2/b_1 = 0.5$, $\omega_1 = 47.69$, $\omega_2 = \omega_1/2$, $\Gamma_2/\Gamma_1 = 0.5$, $a_2/a_1 = 1$, and $a_1 = 0.042$. This is when the vorticity and circulation for the inner pair is both half of those of the outer pair, with the core size of the two pairs remaining the same. In these cases, the distance between the two co-rotating vortices on each side is relatively large and therefore no merging occurs.

Figure 3.8(a) compares the histories of the quadruple source term, Q_2 (since Q_1=0), using the point vortex method and the vortex particle method. In the point vortex method, each vortex of the four vortices in the vortex system is represented by one point vortex. Therefore, the motion captured by the point vortex method is only from each nominal vortex center. Figure 3.8(a) shows that it is close to the vortex centroid motion of low frequency in the result by the vortex particle method. On top of the low frequency component, there is a high-frequency component caused by the vortex core vorticity. Figure 3.8(b) indicates that the low peak

frequency is at 0.09, and the high peak frequency is at 3.61, again close to that of a single Kirchhoff vortex with vorticity of 47.69.

For two identical co-rotating vortices, the frequency for the motion of the vortex center can be calculated as (Mitchell et al. 1995, Howe 2003)

$$f = \frac{\Gamma}{\pi^2 b^2}. \tag{3.2}$$

For two uneven, co-rotating point vortices ($\Gamma_1 > \Gamma_2$), the rotation is illustrated in Figure 3.7. The two vortices have the same rotating center O. Their rotating radius is denoted by R_1 and R_2, respectively. The time period for the rotations is

$$T = \frac{4\pi^2 R_1^{\,2}}{\Gamma_1} = \frac{4\pi^2 R_2^{\,2}}{\Gamma_2},\ R_1 + R_2 = b. \tag{3.3}$$

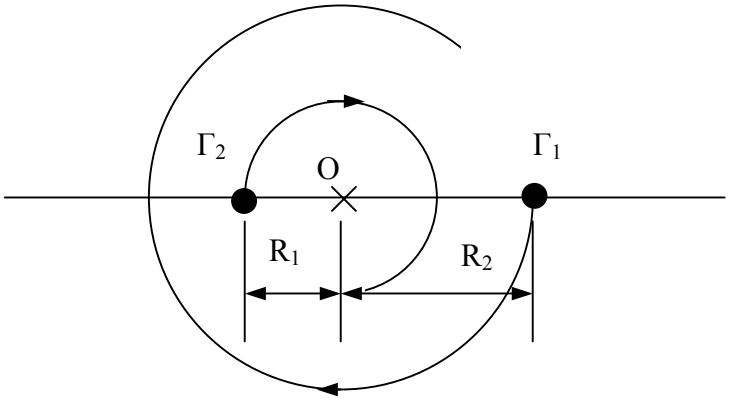

Figure 3.7 Illustration of two uneven wake vortices.

Correspondingly, the frequency for the motion of the vortex center can be calculated as

$$f = \frac{\Gamma_1 + \Gamma_2 + 2\sqrt{\Gamma_1 \Gamma_2}}{4\pi^2 b^2}. \tag{3.4}$$

Clearly, when $\Gamma_1 = \Gamma_2 = \Gamma$, the above frequency f is equal to that in Eq. 3.2 caused by two identical co-rotating vortices. For the parameters in this case (Figure 3.8), the theoretical value of this frequency is 0.08, very close to the simulated value of 0.09.

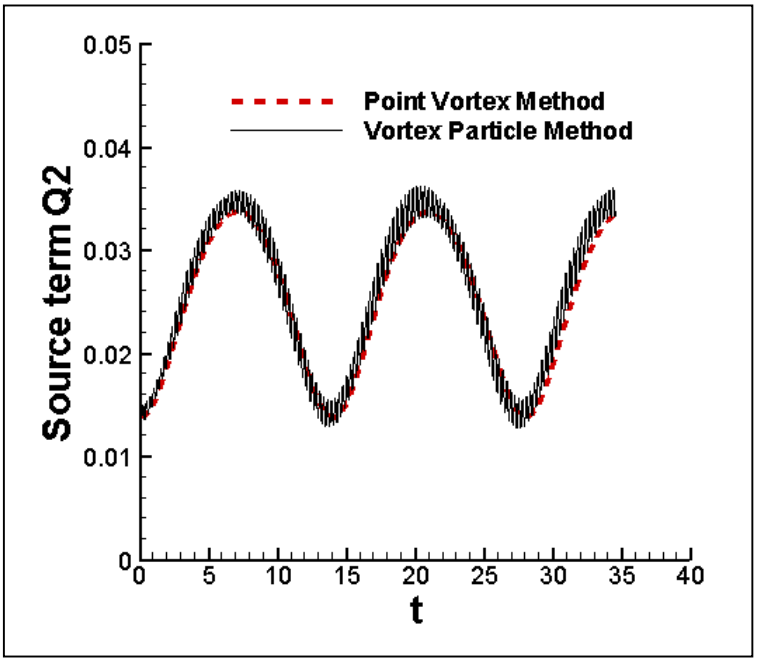

(a)

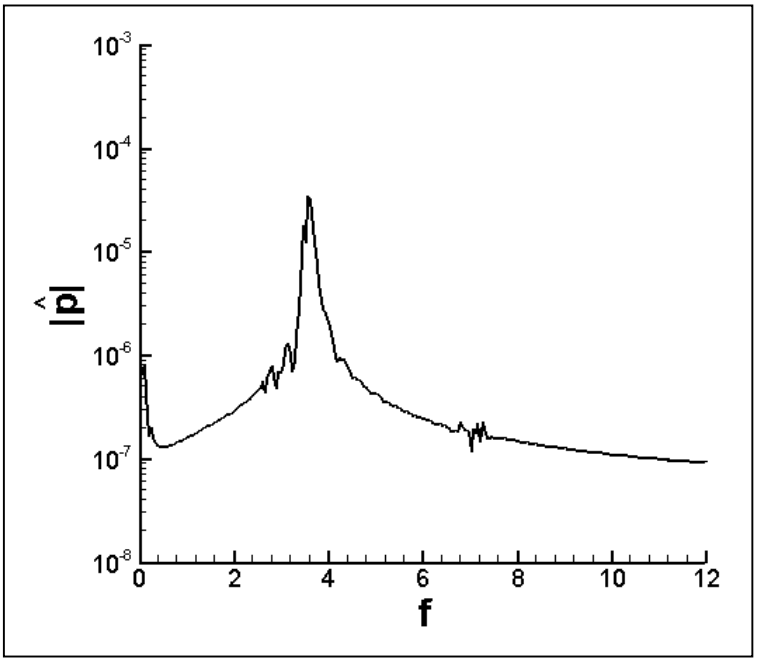

(b)

Figure 3.8 Two vortex pairs with the same vorticity and 1:2 ratio of circulation without merging. (a) History of the quadrupole source term Q_2. (b) Spectrum of sound pressure magnitude in the frequency domain.

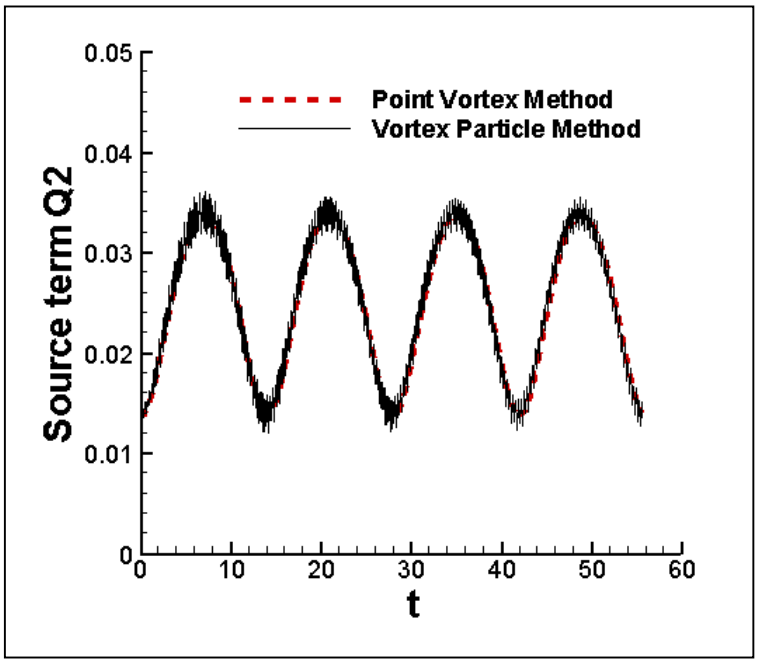

(a)

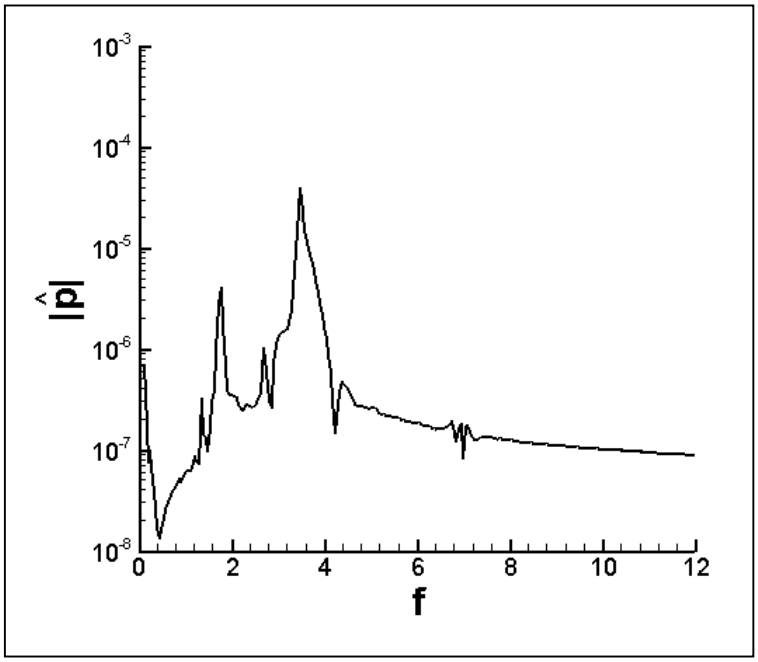

(b)

Figure 3.9 Two vortex pairs with 1:2 ratio in both the vorticity and circulation without merge. (a) History of the quadrupole source term Q_2. (b) Spectrum of sound pressure magnitude in the frequency domain.

In Figure 3.9, because there are two different vorticity values in two vortex pairs, there are two high-frequency components with one at 3.46 and the other at 1.76, each corresponding to the vorticity values of 47.69 and 23.845 respectively. The low frequency component remains at 0.09 as in the case in Figure 3.8, because the ratio of circulation Γ_1, Γ_2 and the ratio of distances b_1, b_2 in the vortex system in this case are the same as those in Figure 3.8.

We now present two cases with vortex merging at one side of the two-vortex-pair system that becomes a one-vortex-pair system after merging. The initial vorticity, separation distance b_1, and core sizes are the same as the two non-merging cases in Figure 3.8 and Figure 3.9, except that the distance ratio of b_2/b_1 varies to create merging.

The first case is the same case as that in Figure 3.9, that is, the two vortex pairs have 1:2 ratios in both vorticity and circulation. Therefore, the core sizes of the vortices are the same, with $a_1 = a_2 = 0.042$. The distance ratio, b_2/b_1, is specified as 0.874, resulting in $\beta = 3$ for the two co-rotating vortices at the same side of the vortex pair system. Figure 3.10 is the source term history and the spectrum of the far-field pressure. It can be seen that there is one peak at a frequency of 3.42, close to that with the higher vorticity value among the two vortices. The low frequency corresponding to the lower vorticity value disappears.

The second case is the same case as in Figure 3.8, that is, the two vortex pairs have 1:2 ratios in circulation, but the vorticity level is the same in the two. Therefore, the core sizes follow a ratio of $(a_2 / a_1)^2 = 0.5$. Since the core sizes are different for the co-rotating vortices at one of the vortex pair system, the average core size is used as a nominal core size to determine the β value. In order to keep the β value approximately equal to 3, the distance ratio is changed to $b_2/b_1 = 0.898$ accordingly. Figure 3.11 is the source term history and the spectrum of the far-field pressure for this case. It can be seen that there is a peak at a frequency of 3.23, lower than the

original Kirchhoff core frequency. This can be explained by the contour plot of the two cases after merging in Figure 3.12. A larger core is shown in the same vorticity case than that in the same core size case, resulting in a lower frequency of pressure fluctuation. Also since the eccentricity in the same core size case is larger, it causes higher fluctuation in the source term in Figure 3.10 than that in Figure 3.11.

3.3.3 Summary and Discussion

In a system with multiple vortices, there are identifiable frequencies when no merging occurs, each of which can be attributed to either the vorticity in the vortex cores or to the motion of the center of the vortices. When two identical vortices are getting closer to each other, the low frequency related to the rotation motion of the vortex center becomes higher, and the high frequency related to the core self-rotation tends to decrease although not significantly. After vortex merging, there is only one frequency resulting from the merged core rotation. In a multiple vortex pair system such as those in aircraft wakes, the above-described behaviors do not seem to change in spite of the induction from the mirror image of the vortices.

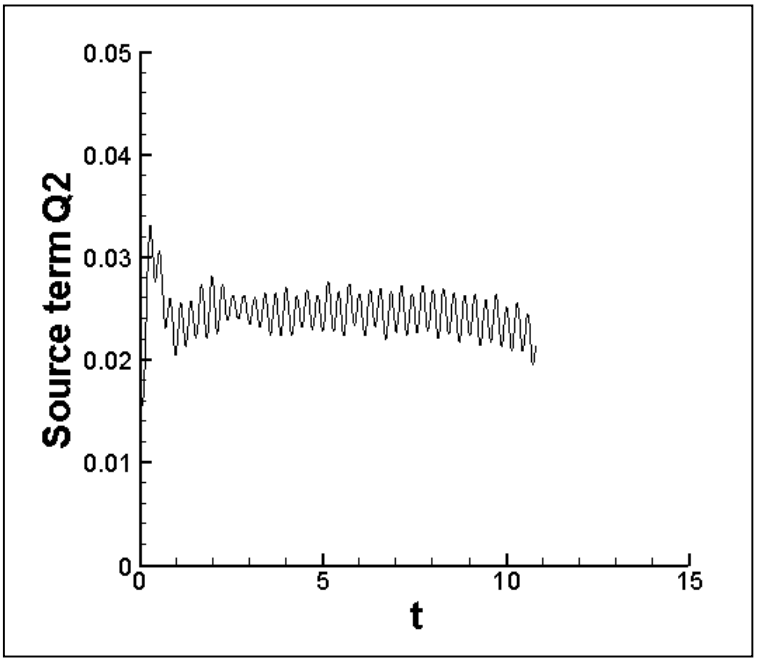

(a)

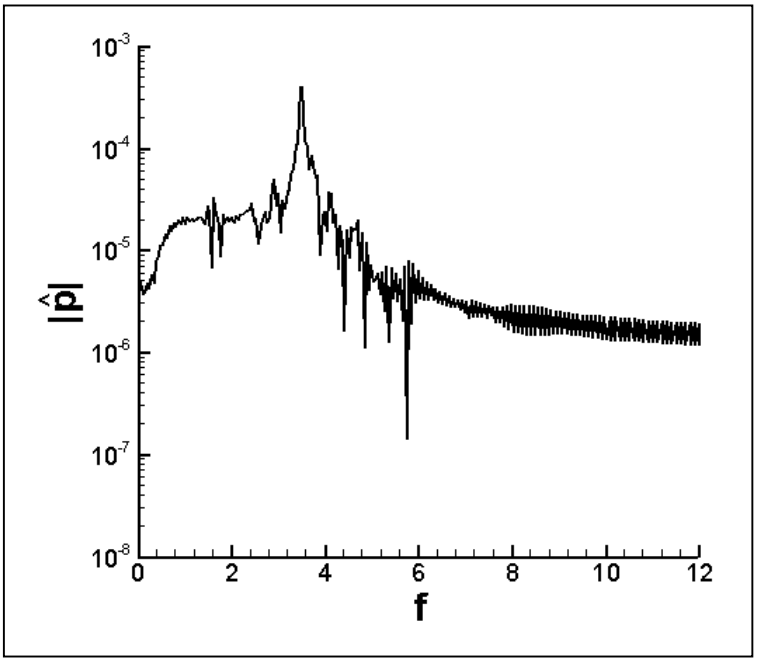

(b)

Figure 3.10 Two vortex pairs with 1:2 ratio in both the vorticity and circulation with merge. (a) History of the quadrupole source term Q_2. (b) Spectrum of sound pressure magnitude in the frequency domain.

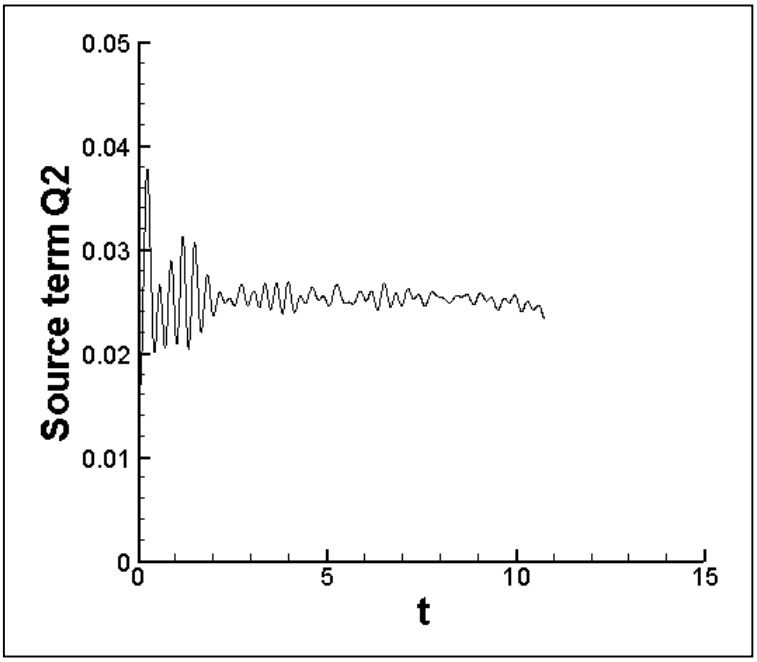

(a)

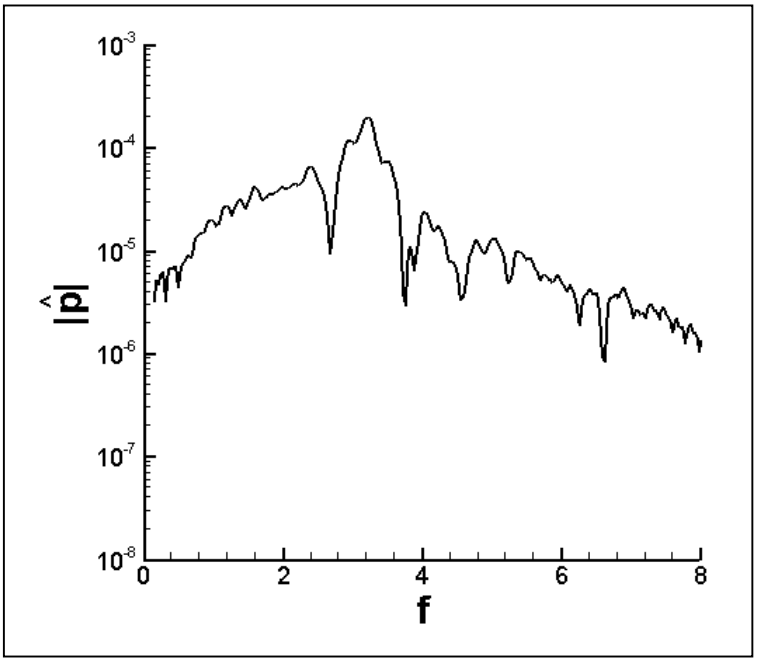

(b)

Figure 3.11 Two vortex pairs with the same vorticity and 1:2 ratio in circulation, with merge. (a) History of the quadrupole source term Q_2. (b) Spectrum of sound pressure magnitude in the frequency domain.

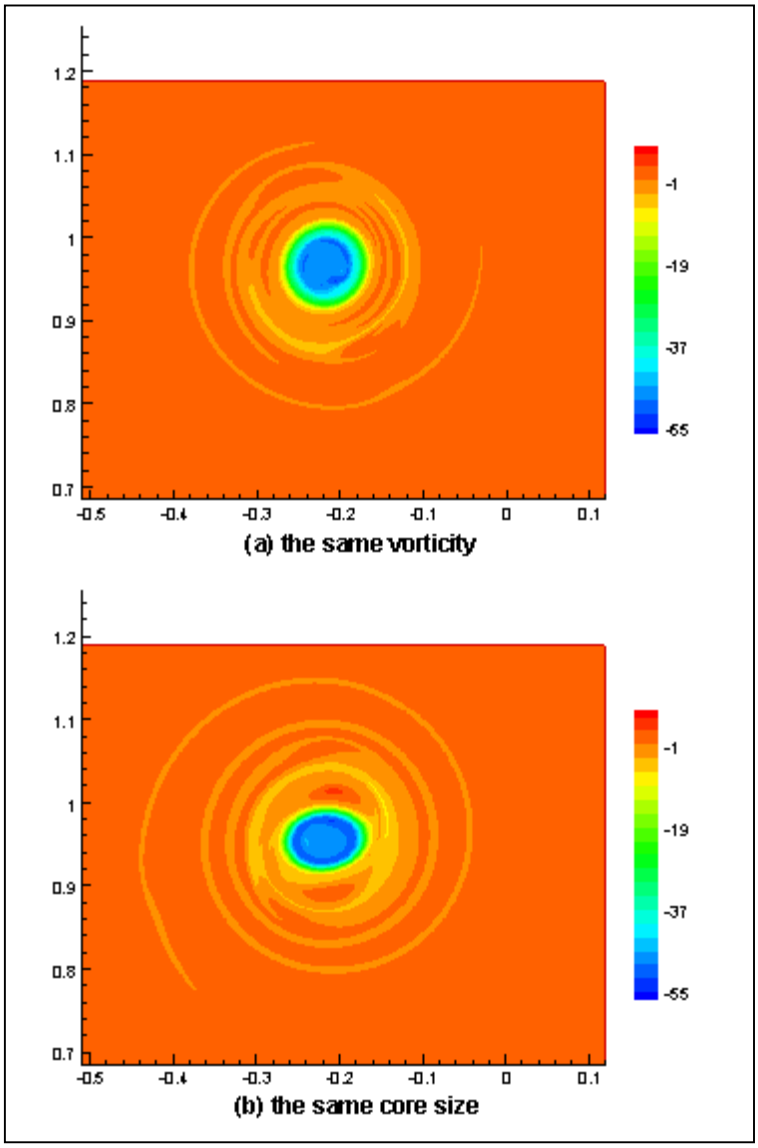

Figure 3.12 Vorticity contours after merging for the cases of co-rotating vortex merge in a two-vortex-pair system. (a) same vorticity; (b) same core size.

4 A Modification of the Three-dimensional Vortex Particle Method with an Application to a Perturbed Vortex Ring

In Chapters 2 and 3, when investigating sound emission from wake vortices, we neglected the stretching effect in the axial direction for the wake vortex system, in order to focus on vortex core behaviors. In this chapter, the stretching effect is considered. Correspondingly, a three-dimensional vortex particle method (Winckelmans and Leonard 1993, Winckelmans et al. 2005) is introduced and modified to simulate the vortices with the stretching effect. Sound produced by a perturbed vortex ring is investigated, mainly based on the 3-D vortex particle method. In addition, both inviscid and viscous interactions are considered and effects of turbulence are simulated using hyper-viscosity sub-grid-scale (SGS) models for Large Eddy Simulation (LES).

4.1 Fundamentals of 3D Vortex Particle Methods

In the vortex particle method, the Navier-Stokes or Euler equations are re-formulated in terms of vorticitiy and discretized. The vorticity-containing particles, instead of the pressure-velocity field, are tracked in a Lagrangian reference frame. The advantages of this approach stem from the Lagrangian discretization that naturally concentrates computational elements into the regions of high vorticity with a rigorous treatment of boundary conditions at infinity, and from the Lagrangian transport that minimizes numerical diffusion. The development and application of vortex methods for incompressible three-dimensional flow are described in several reviews [e.g., Leonard (1980), Winckelmans et al. (1993), Winckelmans et al. (2005)] and a book by Cottet and Koumoutsakos (2000)].

However, in many cases, the vortex particle approximation does not implicitly guarantee the solenoid of the discretized vorticity in space and time for three-dimensional incompressible flow. Neither do they necessarily preserve flow invariants such as linear impulse and energy. Consequently, the accumulation of errors leads to the eventual blow-up of the simulations at long times. Pedrizzetti (1992) devised a linear filtering feedback procedure that reconstructed a divergence-free vorticity field from the non-solenoidal computations in the context of singular particles. Winckelmans and Leonard (1993) reconstructed a solenoidal vorticity field by solving a system of equations for vorticity based on the original particle approximation. These relaxation schemes enforced vorticity field that remained close to $\boldsymbol{\omega} = \nabla \times \mathbf{u}$. But the schemes of relaxation introduced additional numerical diffusion when improvement of the effect of the stability, to some extent, was observed.

An efficient and non-diffusive projection under the VIC (Vortex In Cell) framework was used by Winckelmans (2005) to study wake vortex long- and short-wavelength instability. In his numerical simulation, a VIC method is implemented to ensure that the particle field is divergence free. At each time step, this method requires projection of the particle strengths onto the grid, and the projection of the particles of grid-solved velocity and its gradient back into the particles. Because of the Poisson equation, $\nabla^2 \Psi = -\boldsymbol{\omega}$, one must either assume periodic problems or provide proper boundary conditions on the sides. This is the weak point of the VIC approach.

In this chapter, we explore a different approach from regular three-dimensional vortex particle methods. An additional term, $\mathbf{u}(\nabla \cdot \boldsymbol{\omega})$ (called the divergence term), is considered in the original vorticity transport equation. This term, theoretically equal to be zero, was omitted by most of the methods in the literature. This term is found to properly resolve the perturbation or

fluctuation part in the three-dimensional flow while it has no influence on the mean flow. A kernel based on a deterministic treatment (Eldrege et al. 2002) is used to approximate the divergence term. A hyper-viscosity SGS model (Winckelmans et al. 2005) is also implemented for turbulent flow.

The present method is tested with an application to a perturbed vortex ring. A vortex ring can be thought of as a doughnut-shaped (toroidal) region of azimuthal vorticity. The stability of vortex rings is one of the important problems in hydrodynamic stability. In the early states the unstable mode grows linearly; then non-linear effects become significant as the perturbation becomes large. Eventually the instability leads to breakdown of the vortex ring and into a turbulent ring. Widnall and Sullivan (1973) proposed a linear long-wavelength analysis of a vortex ring with invariant cores. When the self-induced rotation of vortex perturbation balances the rotation induced by the mean velocity of the ring, a mode becomes unstable and the energy of perturbation is expanded in stretching the vortex perturbation. For a ring with a non-deformable core (assuming vortex core size is much smaller than both the local radius of curvature and the wavelength of any perturbation along the filament), the perturbation of the vortex ring is taken as sinusoidal displacements in both the radial and axial directions. They found the most unstable wave number $n = k*R/a,\ k = 1.44$ corresponding to asymptotic results (R/a is the ratio of ring radius to core radius). In their analysis of short wavelength instability, Widnall et al. (1974, 1977) took a slender ring with deformable core into account. They supposed that the instability of the vortex ring to short wave perturbation around the azimuth occurs whenever there is a balance between the self-induced rotation of the waves and the net translational velocity induced owing to the ring strain field. For the slender vortex ring, the most unstable wave number

happens at $n = 2.5*R/a$ for the second radial mode with constant vorticity inside the core (Widnall and Sullivan 1973).

In addition to the theoretical studies of azimuthal instability, there are encouraging prospects for numerical simulation in the area. Knio and Ghoniem (1990) constructed a 3-D vortex method (vortex filament) for simulation of inviscid incompressible flow, and calculated linear growth of azimuthal instability waves for a perturbed vortex ring with non-deformable core and deformable core. Their results agree with the linear theory of stability of Widnall and Sullivan (1973) and Widnall et al. (1974). Whether in the simulation of a thin tube model or vortex torus, they both observed the generation of hairpin vortex structures at the edge of the core, and the shape of the turbulent vortex ring agrees with experimental observation (Lugt 1983, Dyke 1982). Shariff et al. (1994) studied the instability of a viscous vortex ring with a thicker core, with the Reynolds number as high as 5500, by aid of the finite-difference method. In their analysis, multiple bands of wave numbers are amplified, each band having a distinct radial structure. They also found, a viscous correction factor for the peak inviscid growth rate. Their computations were also carried on to the nonlinear growth rate before it could run out of resolution.

4.2 Basic Formulation of 3D Vortex Particle Method

As mentioned in most references related to vortex methods, the evolution of particle position and vorticity for three-dimensional incompressible flow follows (also see Section 2.1 for details)

$$\frac{d\mathbf{x}_p}{dt} = \mathbf{u}(\mathbf{x}_p, t) = \sum_q \mathbf{K}_\sigma(\mathbf{x}_p - \mathbf{x}_q) \times \alpha_q(t), \tag{4.1}$$

$$\frac{d\boldsymbol{\omega}_p}{dt} = (\boldsymbol{\omega}_p \cdot \nabla)\mathbf{u}_p + \nu\nabla^2\boldsymbol{\omega}_p . \tag{4.2}$$

In the regularized version (to avoid singularity) of the vortex particle method, the particle representation of the vorticity field is taken as (Knio and Ghoniem 1990, Winckelmans et al. 1993, Winckelmans et al. 2005)

$$\boldsymbol{\omega}(\mathbf{x},t) = \sum_p \boldsymbol{\alpha}_p \xi_\sigma(\mathbf{x}-\mathbf{x}_p), \tag{4.3}$$

where $\xi_\sigma(\mathbf{x}) = \sigma^{-3}\xi(|\mathbf{x}|/\sigma)$, σ is the blob radius of a regularized particle. $\xi(\mathbf{x})$ is a smooth cutoff or blob function that satisfies $\int \xi(\mathbf{x})d\mathbf{x} = 1$, and $\int x_1^{\alpha 1} x_2^{\alpha 2}\xi(\mathbf{x})d\mathbf{x} = 0$ ($\alpha_1, \alpha_2 \geq 0, \alpha_1 + \alpha_2 \leq r$, r is the order of accuracy). $\mathbf{K}_\sigma$ is a modified Biot-Savart kernel. A more complete discussion of choosing *r*, constructing ξ and $\mathbf{K}_\sigma$ is presented by Beale and Majda (1985).

In our implementation, $\xi(\mathbf{x})$ is a second-order Gaussian function (Winckelmans et al. 2005),

$$\xi(r) = \frac{1}{(2\pi)^{3/2}}\exp(-r^2/2), \tag{4.4}$$

$$\mathbf{K}_\sigma(\mathbf{x}) = -\frac{\mathbf{x}}{4\pi|\mathbf{x}|^3} Q(|\mathbf{x}|/\sigma), \tag{4.5}$$

where $Q(r) = 4\pi\int_0^r \xi(t)t^2 dt = erf(r/\sqrt{2}) - (2/\pi)^{1/2} r\exp(-r^2/2)$ and

$$erf(s) = \frac{2}{\sqrt{\pi}}\int_0^s \exp(-\upsilon^2)d\upsilon$$

To evaluate the viscous term $\nabla^2\boldsymbol{\omega}$, several techniques have been proposed (Cottet and Koumoutsakos 2000). Random-walk methods move the elements in a Brownian motion fashion and re-sampling methods act on the strengths of the elements by sampling the exact solution of the viscous diffusion of singularities at the particle location. Our approach follows the method of

Degond and Mas-Gallic (1989), which is known as the particle strength exchange (PSE) scheme. It is based on an integral representation of the Laplace operator. One can have

$$\nabla^2\boldsymbol{\omega} = \frac{2}{\sigma^2}\int \eta_\sigma^{lap}(\mathbf{x}-\mathbf{y})(\boldsymbol{\omega}(\mathbf{y})-\boldsymbol{\omega}(\mathbf{x}))d\mathbf{y} = \frac{1}{\sigma^2}\eta_\sigma^{lap}(\mathbf{x}-\mathbf{x}_q)(\boldsymbol{\omega}_q-\boldsymbol{\omega})V_q\,, \qquad (4.6)$$

where $\eta^{lap}(r) = -\dfrac{\xi'(r)}{r} = \xi(r)$ and $\eta_\sigma^{lap}(\mathbf{x}) = \sigma^{-3}\eta^{lap}(|\mathbf{x}|/\sigma)$

Since the strength of each particle can be expressed as $\boldsymbol{\alpha}_p = \int_{V_p}\boldsymbol{\omega}dV = \boldsymbol{\omega}_p V_p$, the evolution of vorticity strength may read as

$$\frac{d\boldsymbol{\alpha}_p}{dt} = (\boldsymbol{\alpha}_p\cdot\nabla)\mathbf{u}_p + \frac{2\nu}{\sigma^2}\sum_q \eta_\sigma^{lap}(\mathbf{x}_p-\mathbf{x}_q)(V_p\boldsymbol{\alpha}_q - V_q\boldsymbol{\alpha}_p)\,. \qquad (4.7)$$

Notice that the method converges for regular vorticity fields as the number of particles is increased, provided that the cores of neighbor blobs or particles maintain overlapping. Here, we use $\sigma = h$ (Winckelmans et al. 2005), where h is the spacing size, to ensure the "communication" of information between the particles.

In the present implementation of the vortex particle method for three-dimensional flows, periodic redistribution is also needed to maintain convergence requirements (Beale and Majda 1985). In Section 2.1 we discussed the redistribution in detail. In the 3-D vortex particle method, particles are periodically redistributed or remeshed to a regular lattice ($h\times h\times h$) in order to maintain the convergence requirement of vortex methods that preserve particle overlap (Beale and Majda 1985). Here, the redistribution of particle strength is performed by

$$\tilde{\boldsymbol{\alpha}}_p = \sum_q W\left(\frac{\tilde{X}_p - X_q}{h}\right)\boldsymbol{\alpha}_q\,, \qquad (4.8)$$

where h is the size of a regular redistribution lattice. One of the most widely used interpolation kernels, $M_4^{'}$ (Cottet and Koumoutsakos 2000) is used in this study. It is given by

$$M_4^{'}(U) = \begin{cases} 1 - 5/2U^2 + 3/2U^3 & if\ 0 \le U \le 1 \\ (1-U)(2-U)^2/2 & if\ 1 \le U \le 2 \\ 0 & otherwise \end{cases}. \tag{4.9}$$

For 3D, $W(U,V,W) = M_4^{'}(U)M_4^{'}(V)M_4^{'}(W)$.

4.3 Treatment of Vorticity Divergence

As discussed in the paper by Winckelmans and Leonard (1993), the particle field (Eq. 4.3), which is not generally divergence-free, is used to represent the divergence-free field:

$$\nabla \cdot \tilde{\boldsymbol{\omega}} = \sum_p \nabla(\zeta_\sigma(\mathbf{x} - \mathbf{x}_p)) \cdot \boldsymbol{\alpha}_p \neq 0 \quad . \tag{4.10}$$

We use $\tilde{\boldsymbol{\omega}}$ to differentiate the original particle field $\boldsymbol{\omega} = \nabla \times \mathbf{u}$, which is divergent-free. It is clear the divergence-free problem can be relaxed by the diffusion term under low Reynolds flow (Ploumhans et al. 2002). However, for high Reynolds flow or inviscid flow, one cannot run a long time simulation due to the non-solenoidal vorticity problem.

As a result, we use a modification of the vorticity transport equation that takes a different approach from those in the literature (such as linear filtering procedure by Pedrizzeti 1992 and reconstruction of particle field by Winckelmans and Leonard (1993). For 3-D incompressible viscous flow, we take a curl of the Navier-Stokes momentum equation $\partial \mathbf{u}/\partial t + \mathbf{u} \cdot \nabla \mathbf{u} = -\nabla p/\rho + \nu \nabla^2 \mathbf{u}$ to get

$$\frac{d\boldsymbol{\omega}}{dt} = (\boldsymbol{\omega} \cdot \nabla)\mathbf{u} - \boldsymbol{\omega}(\nabla \cdot \mathbf{u}) + \mathbf{u}(\nabla \cdot \boldsymbol{\omega}) + \nu \nabla^2 \boldsymbol{\omega}, \tag{4.11}$$

where $(\boldsymbol{\omega}\cdot\nabla)\mathbf{u}$ is the stretching term, which is evaluated by directly differentiating the velocity kernel (Eq. 4.1) for the current trend (Anderson and Greengard 1985). Here the terms $\boldsymbol{\omega}(\nabla\cdot\mathbf{u})$ and $\mathbf{u}(\nabla\cdot\boldsymbol{\omega})$ are left intact intentionally and is discussed below. Although the vorticity field is not divergent-free, the velocity field (Eq. 4.1) is divergent-free since it is the curl of a stream function, which can be proved by

$$\nabla\cdot(\sum_{q}\mathbf{K}_{\sigma}(\mathbf{x}_{p}-\mathbf{x}_{q})\times\boldsymbol{\alpha}_{q}(t))=0\,, \tag{4.12}$$

where the term $\boldsymbol{\omega}(\nabla\cdot\mathbf{u})$ in Eq. 4.6 can be removed; however, because of $\nabla\cdot\tilde{\boldsymbol{\omega}}\neq 0$, $\mathbf{u}(\nabla\cdot\boldsymbol{\omega})$ should be kept in the equation for the evolution of vorticity.

Gharakhani (1997) pointed out the term $\mathbf{u}(\nabla\cdot\boldsymbol{\omega})$ must be included to keep the correct balance of Eq. 4.6. By taking the divergence of Eq. 4.6, he thought that the rate of change of the divergence of vorticity is zero everywhere in the field when the term is included while the rate remains zero only on the Lagrangian path of the elements when the term is discarded. He also reported the test problem of a self-propelling vortex ring with very long-time stability. According to Gharakhani (1997), this is one way to maintain the solenoidality of the vorticity field for inviscid flow.

Actually, we found that the term not only acts to maintain the divergent-free field, and it also helps resolve a perturbed field. The perturbation part will be gone and only the steady part of the flow in a perturbed vortex ring is captured if we neglect the term. In other words, the simulation of a steady self-propelling vortex ring is not influenced by the inclusion of the term while the simulation of a perturbed or turbulent phenomena is very sensitive to the term. In the following numerical experiments, we prove this viewpoint in detail with an application to a vortex ring.

To evaluate the divergence of vorticity, one easy way is to take the divergence of the particle approximation, Eq. 4.3, directly as follows

$$\nabla \cdot \boldsymbol{\omega}_p = \sum_q \nabla \xi_\sigma(\mathbf{x}_p - \mathbf{x}_q) \cdot \boldsymbol{\omega}_q V_q = \frac{-1}{\sigma^2} \sum_q (\mathbf{x}_p - \mathbf{x}_q) \eta_\sigma^{lap}(\mathbf{x}_p - \mathbf{x}_q) \cdot \boldsymbol{\omega}_q V_q . \qquad (4.13)$$

It is pointed out in Eldredge et al. (2002) and Cottet and Koumoutsakos (2000) that applying the derivative operator directly to the blob function would be analogous to the method of Fishelov (1990) in evaluating the viscous term $\nabla^2 \boldsymbol{\omega}$ for incompressible flow, which is derived from the approximation $\nabla^2 \boldsymbol{\omega} = \omega * \nabla^2 \xi_\sigma$, and lacks the conservation properties of PSE (Particle Strength Exchange). Similarly, the result of Eq. 4.13 also lacks the conservation properties of PSE.

A conservative scheme is obtained based on the deterministic treatment of derivatives of Eldredge et al. (2002):

$$\frac{\partial \omega_\mathbf{i}}{\partial x_i} = \frac{1}{\sigma} \sum_q (\omega_{iq} + \omega_{ip}) V_q \eta_\sigma^i(\mathbf{x}_p - \mathbf{x}_q) , \qquad (4.14)$$

where the kernel η_σ^i satisfies the momentum condition $\int x_i \eta_\sigma^i(\mathbf{x}) = -\sigma$. To figure out the kernel, we can look back to the momentum condition in evaluating the viscous term $\int x_i x_j \eta_\sigma^{lap}(\mathbf{x}) d\mathbf{x} = \delta_{ij} \sigma^2$. Therefore, if the template $\eta_\sigma^i(\mathbf{x}) = A \frac{x_i}{\sigma} \eta_\sigma^{lap}(|\mathbf{x}|)$ is chosen, one can easily find A = -1. This results in the following conservative scheme for the divergence term

$$\nabla \cdot \boldsymbol{\omega}_p = \frac{-1}{\sigma^2} \sum_q (\mathbf{x}_p - \mathbf{x}_q) \eta_\sigma^{lap}(\mathbf{x}_p - \mathbf{x}_q) \cdot (\boldsymbol{\omega}_q + \boldsymbol{\omega}_p) V_q . \qquad (4.15)$$

If one compares Eq. 4.8 and Eq. 4.10, it is easily found that the correction term $\frac{-1}{\sigma^2}\sum_q (\mathbf{x}_p - \mathbf{x}_q)\eta_\sigma^{lap}(\mathbf{x}_p - \mathbf{x}_q)\cdot\boldsymbol{\omega}_p V_q$ is missing in Eq. 4.8, which therefore fails to be conservative.

It should be pointed out that a conservative scheme of evaluating the gradient of a function is mentioned by Winckelmans (2004) when he considers the source term involving $\nabla(T - T_o)$ in the vorticity equation and uses the fact that $\int (\mathbf{y} - \mathbf{x})\eta_\sigma^{lap} d\mathbf{y} = 0$:

$$\nabla f_p = \frac{1}{\sigma^2}\sum_q (\mathbf{x}_q - \mathbf{x}_p)\eta_\sigma^{lap}(\mathbf{x}_p - \mathbf{x}_q)(f_q + f_p)V_q . \qquad (4.16)$$

With this knowledge, one also can easily obtain the conservative scheme of divergence term Eq. 4.10.

It is noted, however, the scheme does not provide an exactly zero divergence in regions where particles have the same strength.

4.4 Hyper-viscosity Sub-grid Scale Model

Our numerical experiments also show that, even with the proposed additional term, simulation of an inviscid perturbed vortex ring still suffers the problems of divergence-not-free for a long-time simulation. This is mainly because the small dissipation produced by the particle redistribution operation is not sufficient to diffuse the numerical error.

Winckelmans (2005) proposed a hyper-viscosity SGS model when he performed a simulation of wake vortex instability,

$$\frac{d\boldsymbol{\omega}}{dt} = (\boldsymbol{\omega}\cdot\nabla)\mathbf{u} - \frac{C}{t_o}(h^2\nabla_h{}^2)^{\mathbf{2}}\boldsymbol{\omega} . \qquad (4.17)$$

In his numerical simulation, a VIC method (vortex-in-cell) is implemented to ensure that the particle field is divergence free. At each time step, this method requires projection of the particle strengths onto the grid, and the projection of the particles of grid-solved velocity and its gradient back into the particles. As the Poisson equation $\nabla^2\Psi = -\boldsymbol{\omega}$ states, one must either assume periodic problems or provide proper boundary conditions on the sides. This is the weak point of the VIC approach. In his simulation, the second term in the right side of Eq. 4.12 is obtained by iterating twice a grid-evaluated Laplacian. No additional details of the SGS model are given in the literature.

However, in our view, replacing ∇^2 of the diffusion term with $-\nabla^4$ is equivalent to replacing υ with an eddy viscosity. A variant of the eddy-viscosity model replaces derivatives in the dissipative terms with high-order operations. The approach is called hyper-viscosity because it enhances the damping of motion as the length scale decreases.

Furthermore, in our implementation, the SGS term is still calculated based on the PSE schemes: first, $\mathbf{f} = \nabla^2\boldsymbol{\omega}$ is evaluated according to the laplacian kernel for viscous term, and then $\nabla^2\mathbf{f}$ is evaluated.

4.5 Numerical Analysis of Divergence Term with the Application to a Vortex Ring

4.5.1 Propagation of a Steady Viscous Ring

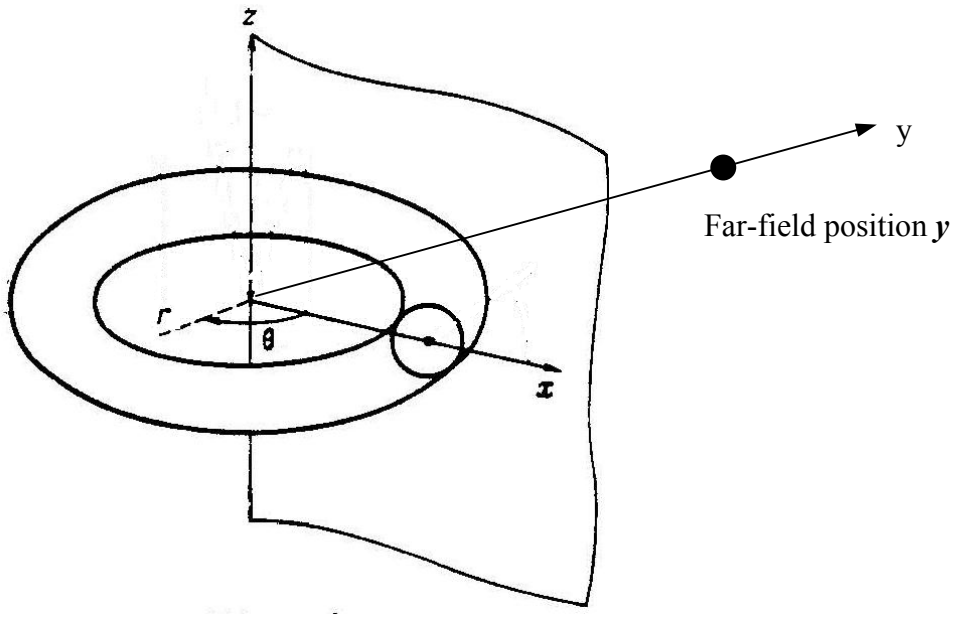

Figure 4.1 An illustration of a vortex ring

The first example is a single viscous ring at $\mathrm{Re}_\Gamma = \Gamma / \nu = 500$ by Wee and Ghoniem (2006). The ring of radius R and core radius a are initially placed at the $z = 0$ plane. The ring has unit circulation and unit radius, i.e., $\Gamma = 1$ and $R = 1$. The core of the ring is represented as

$$\omega_\theta = \frac{1.2564\Gamma}{\pi a^2} \exp\left\{-1.2544 \frac{z^2 + (r-R)^2}{a^2}\right\}, \tag{4.18}$$

This is the expression for a second-order Gaussian core. $r = \sqrt{x^2 + y^2}$.

In our numerical simulation, $h = 0.1$ and $\Delta t = 0.1$. The results are illustrated in Figure 4.2. It should be noted that the data from the literature is re-shifted back to match our time scale.

From the figure, we can see that the speed of the vortex ring centroid in our simulation is lower than that in the literature. However, the evolution of the circulation matches with the literature very well. This is because our numerical simulation is performed at coarse resolution, which more strongly affects convection than diffusion.

As a validation, a simulation without the divergence term is also performed. The result of speed and circulation is almost identical with that of divergence term. By measuring the divergence term, it is found that the magnitude is very small so that it can be neglected compared to the stretching term. The test shows, for a steady vortex ring, the difference of $\tilde{\boldsymbol{\omega}}$ and $\boldsymbol{\omega} = \nabla \times \mathbf{u}$ can be neglected.

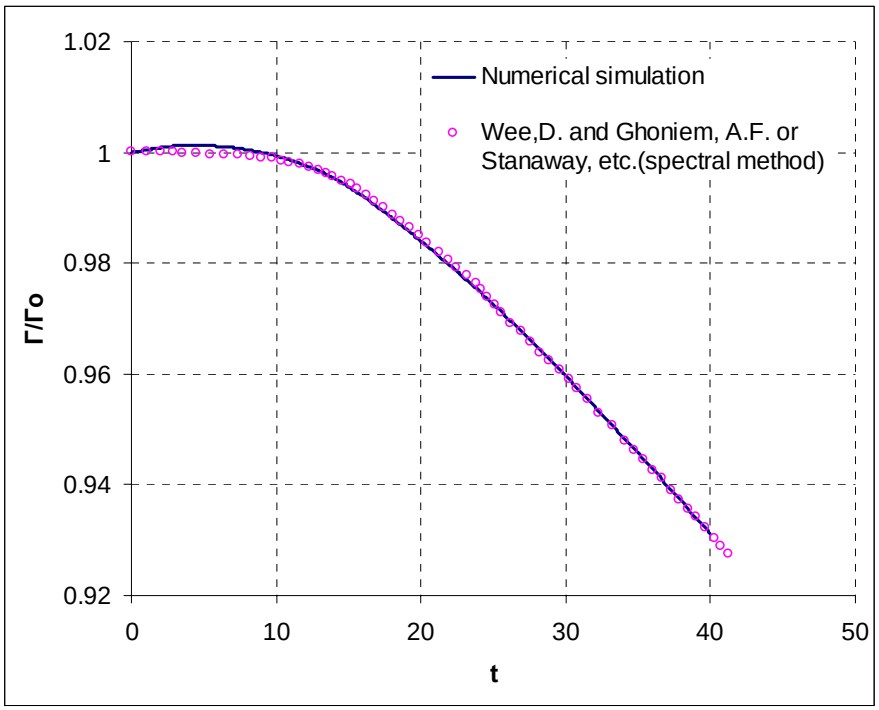

(a)

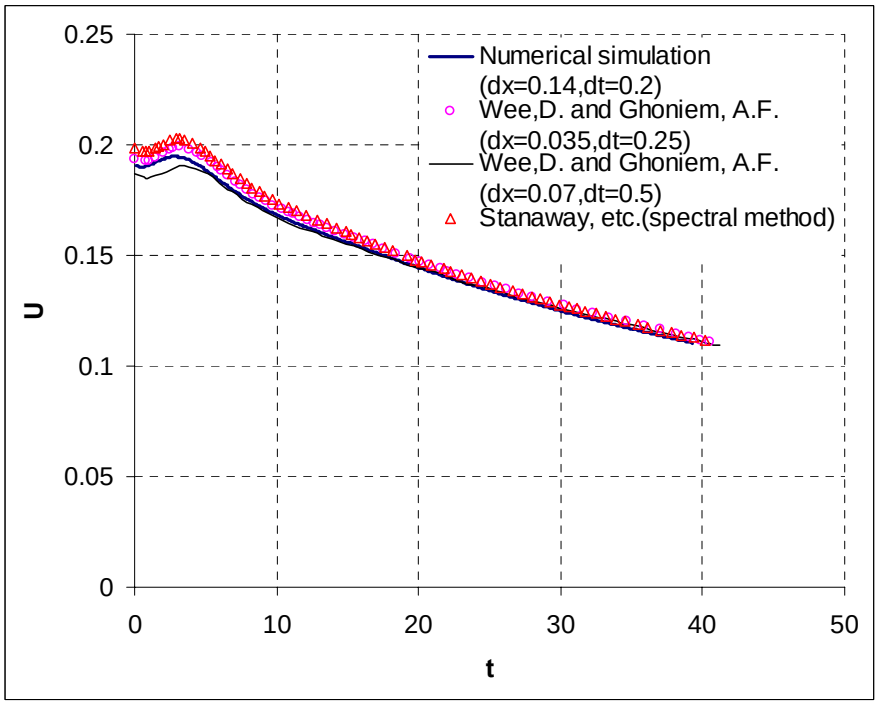

(b)

Figure 4.2 (a) Circulation of the vortex ring verses time. (b) Speed of the vortex ring verses time.

4.5.2 Growth of a Perturbed Inviscid Vortex Ring

The second example is a perturbed 'inviscid' fat vortex ring, which was used by Gharakhani 2003 to study turbulence model (LES). In his simulation, by applying the eddy diffusivity model, he observed the growth of the perturbation for a long time. Therefore, he used 'inviscid' to emphasize that the simulation is not truly inviscid.

The vortex ring is initially centered at (0,0,0), with azimuthal core vorticity distribution

$$\omega_\theta = \frac{\Gamma}{2.836a^2}\exp\left\{-\frac{r_d^{\,3}}{a^3}\right\}, \tag{4.19}$$

This is the expression for a third-order Gaussian core. r_d is the position with respect to the vortex core center (in the azimuthal plane). $a = 0.45R$ is the vortex core size and R is the unperturbed ring radius. Vorticity is normalized to yield circulation $\Gamma = 2$. The ring is initially perturbed around the ring azimuth using

$$R_o = R(1 + A\sin(n\theta)), \tag{4.20}$$

where R_o is the distance from the core center to the origin. The wave number is set to $n = 7$, which coincides with the wave number of the most unstable azimuthal bending mode (Knio and Ghoniem 1990). The perturbation amplitude is set to $A = 0.05$.

The initial ring is discretized using the uniform grid of mesh size $h/R = 0.1375$ and $\Delta t\Gamma / R^2 = 0.175$. All the parameters are the same as those in the paper of Gharakhani 2003.

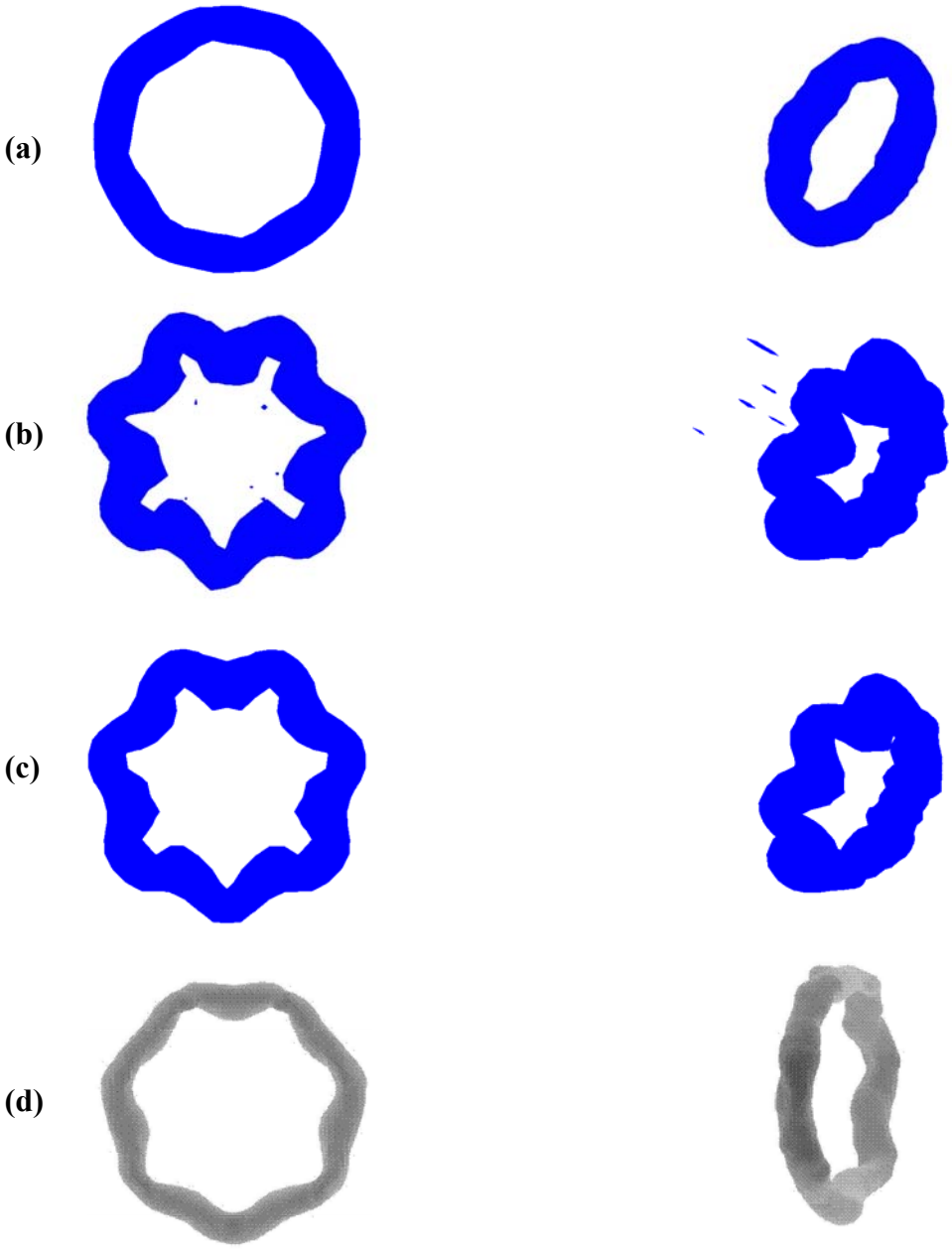

Figure 4.3 Bottom and perspective views of ISO-vorticity surface of magnitude $|\omega|R^2/\Gamma = 1.43$ **at time** $t\Gamma/R^2 = 17.5$ **(a) Numerical simulation without divergence term and without SGS model. (b) Numerical simulation with divergence term and without SGS model (c) Numerical simulation with divergence term and SGS model. (d) Taken from Gharakhani 2003.**

Figure 4.3 shows the ISO-surface of vorticity magnitude $|\omega|R^2/\Gamma = 1.43$ at time $\Delta t\Gamma/R^2 = 17.5$. These calculations are based on the same initial conditions as described previously. The simulations are intended to test the effect of the divergence term and hyper-viscosity SGS model. For comparison, the numerical results from the paper of Gharakhani (2003) are also plotted here.

When Figure 4.3 (a) and (b) are compared, it is clear that the divergence term $\mathbf{u}(\nabla \cdot \boldsymbol{\omega})$ is nevertheless required for the perturbed phenomena and it helps resolve the unresolved small fluctuation. Neglecting the term in the simulation, we only capture mean flow such as what is shown in Figure 4.3 (a).

The comparison between Figure 4.3 (b) and (d) tells us that at the same time level, the extent of growth based on the condition of (b) is much stronger than that based on the condition of (d). In the paper of Gharakhani 2003, he pointed out that turbulent diffusion of LES is so high that it inhibits the growth of the streamwise vortices substantially. This is true. Our simulation in Figure 4.3 (b) is implemented in truly inviscid flow; therefore, the growth occurs without any inhibition (except a little bit by remeshing). However, the growth causes some problems such that numerical error is visible in the result (spots in Figure 4.3 (b), which will make numerical simulation unstable. The implementation of hyper-viscosity successfully removes the problems while maintaining almost the same growth rate as that without the SGS model, which is shown in Figure 4.3 (c).

It is worth noting that the mechanism of maintaining vorticity solenoidal in the paper of Gharakhani 2003 is different from our current scheme. In that paper, Gharakhani claimed that the vorticity redistribution method of particle insertion strategy tends to maintain the stability and accuracy of the predictions of the perturbed vortex ring with the consideration of LES. It is

unclear whether the VRM helps to resolve the small scale of perturbation or LES does. In our current method, it is apparent that the divergence term $\mathbf{u}(\nabla \cdot \boldsymbol{\omega})$ helps to resolve the fluctuations in the phenomena while the hyper-viscosity SGS model helps maintain the numerical stability for a long-time simulation. In the simulation of wake vortex instability by Winckelmans (2005), the small scale of fluctuation is captured through VIC method while SGS model to maintain a long time simulation.

This can be further confirmed through comparing Figure 4.4 and Figure 4.5. Specifically, in Figure 4.4 (without SGS model), early sign of breakdown of the unstable vortex ring can be observed at $t\Gamma / R^2 = 24.5$ while the sign of breakdown for the case with SGS model occurs after $t\Gamma / R^2 = 28$ (Figure 4.5). Actually, the numerical error appearing in Figure 4.4 accelerates the breakdown of the vortex ring before it reaches the same extent of growth physically as Figure 4.5 does. The instability caused by small-scale numerical error is hard to discern through the illustration of averaged kinetic energy or linear impulse. The curve of kinetic energy of Figure 4.6 tells us that the simulation without the SGS model is stable before the vortex ring breaks up at $t\Gamma / R^2 = 24.5$ and the simulation with the SGS model is also stable until the vortex ring breaks down at $t\Gamma / R^2 = 35$. Figure 4.7 is the illustration of linear impulse. As Gharakhani (2003) discussed, the thick solid line indicates the solution without LES eventually blows up while the dash line shows the solution with VRM LES is stable and conserves linear impulses quite well. Our current simulation results using the SGS model are depicted by the solid line, which also indicated our solution is stable until $t\Gamma / R^2 = 35$. The simulation without the SGS model also conserves the linear impulse until it breaks down at $t\Gamma / R^2 = 24.5$. It is unclear why the simulation result with VRM LES of Gharakhani (2003) stops at $t\Gamma / R^2 = 17.5$.

As mentioned previously, the selected wave number n = 7 corresponds to the most unstable mode according to the numerical analysis of the growth rate by Knio and Ghoniem 1990, which agrees with the linear instability analysis of the third order radial mode for a perturbed vortex ring by Widnall (1973). The numerical identification of the most unstable wave number can also be performed based on the comparison of the kinetic energy for each wave number. Figure 4.8 depicts the kinetic energy in different azimuthal modes under the same SGS constant Ch^4 / t_o = 2.5e-5. They are all dissipated slightly by frequent global remeshing and the implementation of hyper-viscosity SGS model. The process of dissipation helps to maintain the stability of operation. Mode n = 7 has the greatest oscillatory behavior, indicating n = 7 is the most amplified wave mode for the particular core size and the third-order Gaussian core, which is in good agreement with Widnall linear instability analysis and also consistent with the numerical results of Knio and Ghoniem (1990).

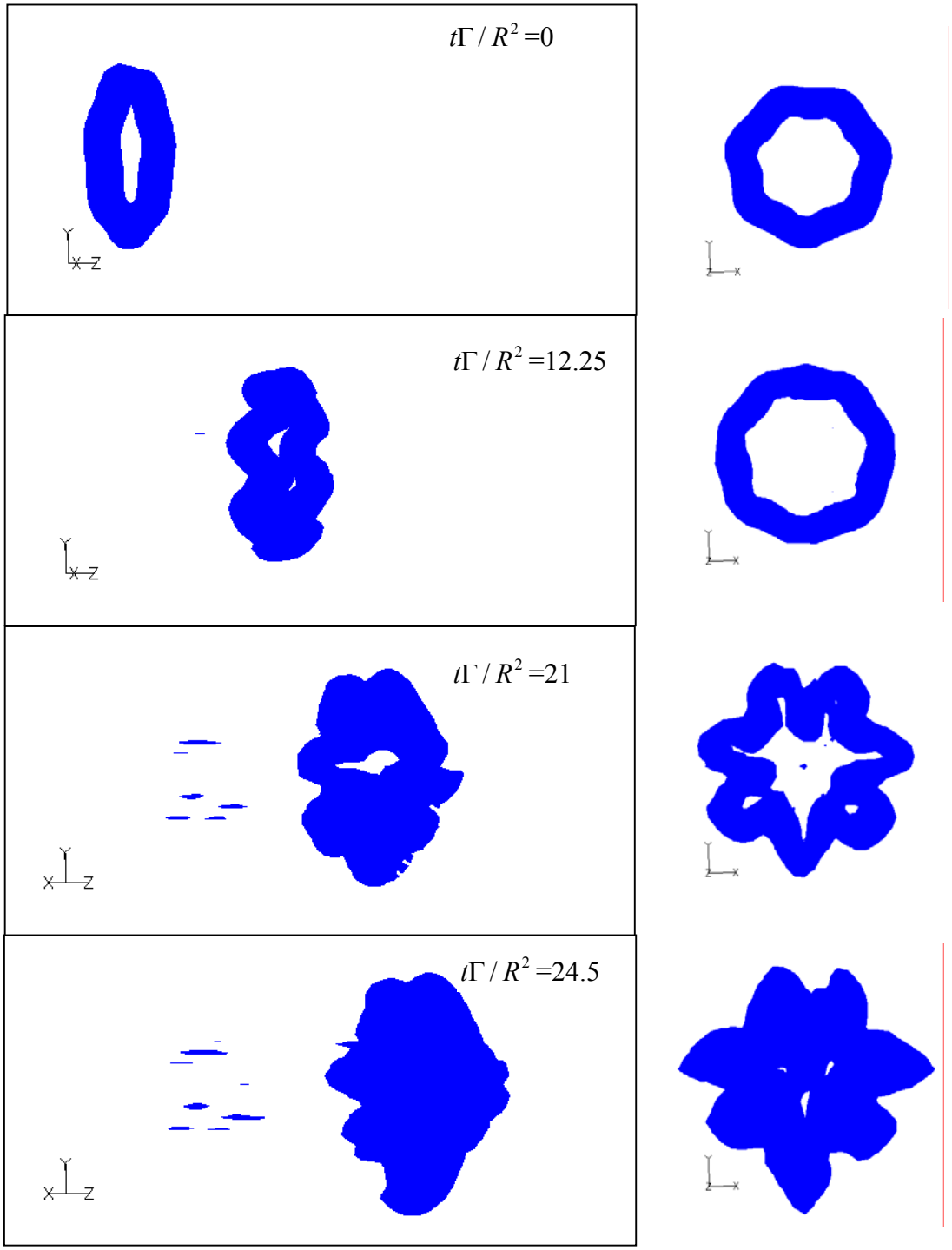

Figure 4.4 Perspective (Left) and Bottom (Right) views of ISO-vorticity surface of magnitude $|\omega| R^2 / \Gamma = 1.43$ at time $t\Gamma / R^2$ = 0, 12.25, 21 and 24.5 without the SGS model

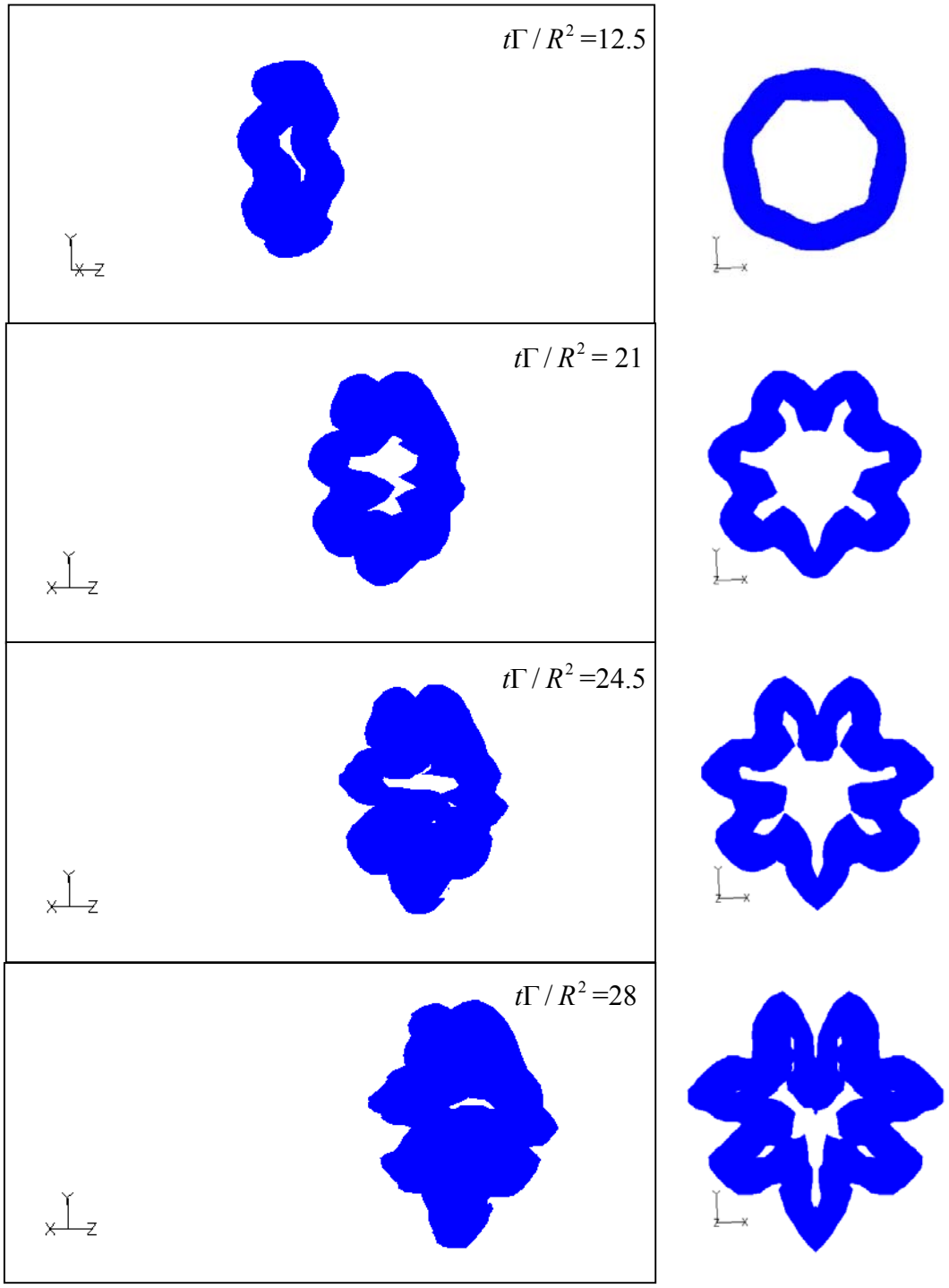

Figure 4.5 Perspective (Left) and Bottom (Right) views of ISO-vorticity surface of magnitude $|\omega|R^2/\Gamma = 1.43$ at time $t\Gamma / R^2$ = 12.25, 21, 24.5, 28 (from top to bottom) with SGS model

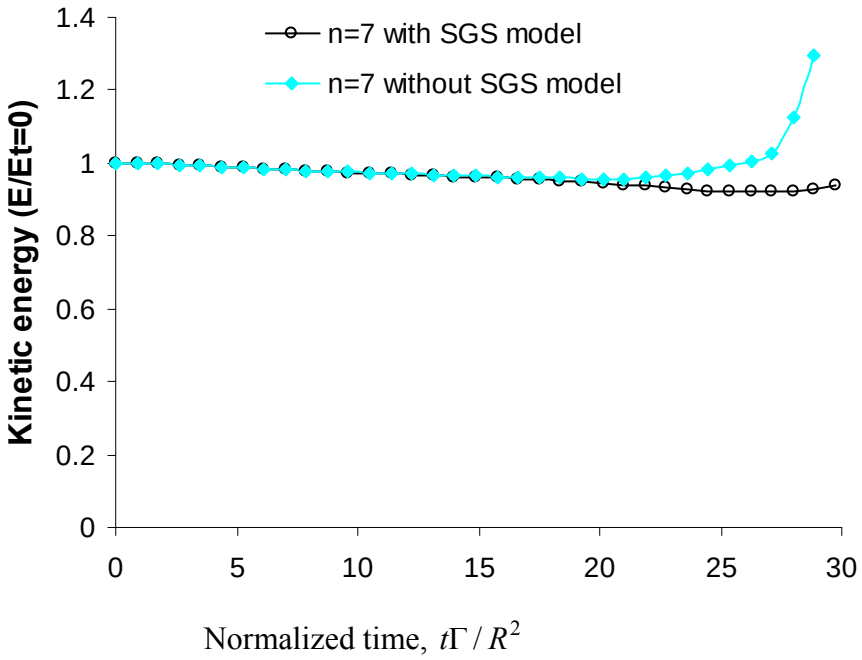

Figure 4.6 Kinetic energy ($E/E_{t=0}$) of a perturbed vortex with wave number n = 7.

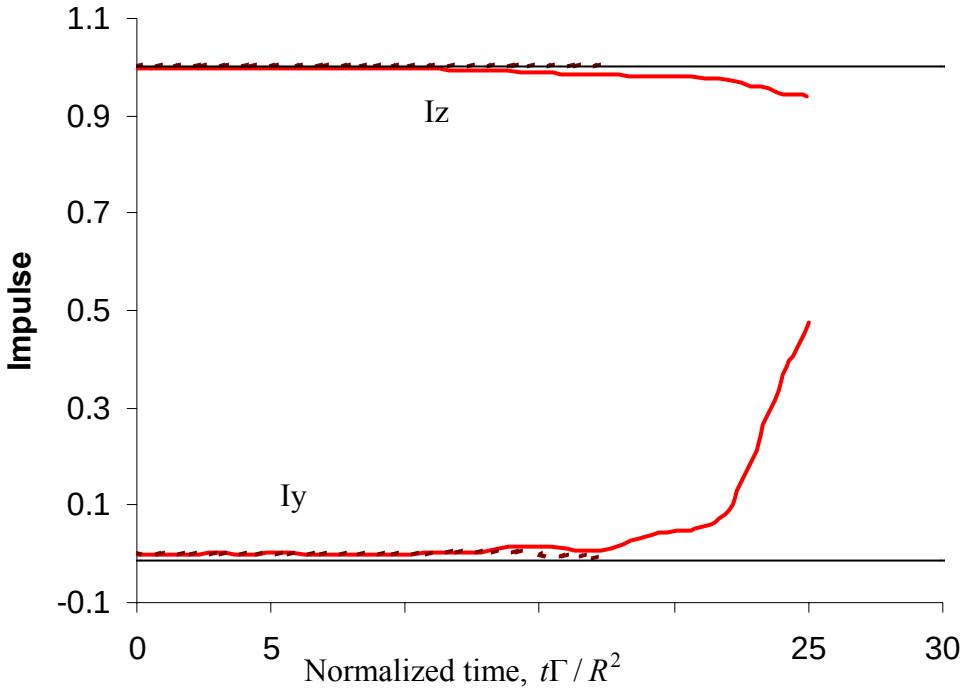

Figure 4.7 Linear impulses of a perturbed vortex with wave number n = 7 in the streamwise (Iz) and cross-stream (Iy) directions (solid) with comparisons of Gharakhani 2003 (dashed: VRM LES, thick solid: No LES).

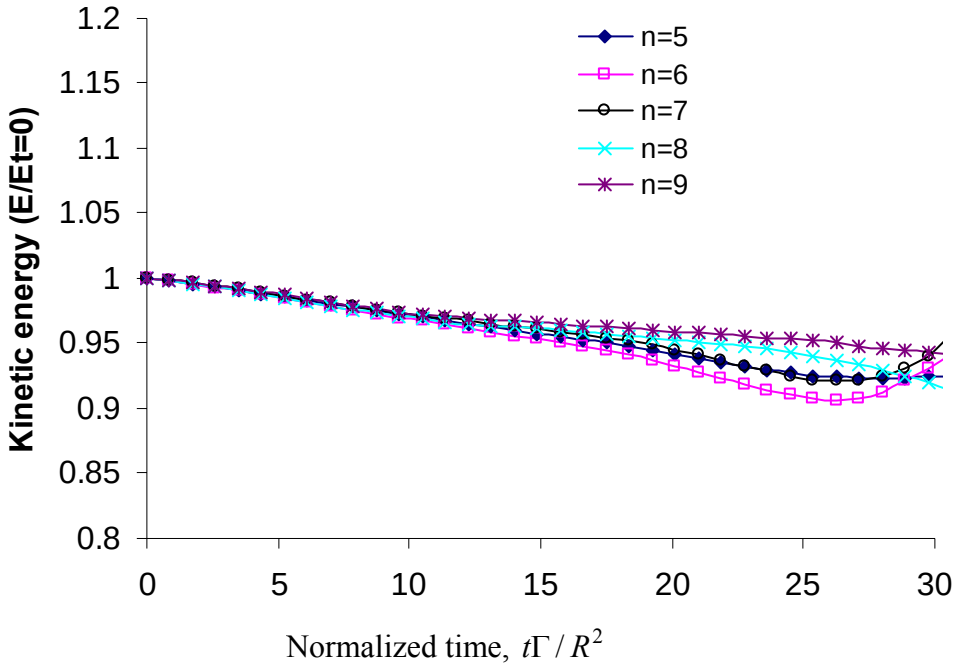

Figure 4.8 Kinetic energy ($E/E_{t=0}$) of a perturbed vortex with different wave numbers.

4.5.3 Growth of a Perturbed Vortex Ring with Viscous Effects

In the following example, we will study the instability of a perturbed vortex ring with a viscous effect. Saffman (1978) has shown that the vortex ring instability is dependent on the Reynolds number. When the Reynolds number is sufficiently small, the vortex ring will remain laminar. Previous studies (Rosenfel et al. 1998) have shown that the limiting Re for the vortex ring instability is in the range of 1000 to 1800, depending on the formation conditions.

The example is a viscous perturbed vortex with the same vorticity distribution as described in the preceding section (third order Gaussian distribution). The core radius to ring radius is a/R = 0.275, the amplitude of perturbation A = 0.02, wave number n = 12 and the Reynolds number based on the ring circulation is $\mathrm{Re}_\Gamma = \Gamma / \nu = 2200$. Vorticity is normalized to yield circulation $\Gamma = 1$. The present ring parameters are the same as those in Mansfield et al.

(1999), and the wave number n = 12 corresponds to the most amplified mode of the Widnall instability for the third-order Gaussian core distribution at this particular core size (Widnall and Tsai 1977, Knio and Ghoniem 1990).

Mansfield et al. (1999) simulated the evolution of the perturbed vortex ring with the inclusion of the LES turbulence model. A Lagrangian vortex particle method is also used in the paper. The difference between his method and our current scheme is that, in the paper of Mansfield et al. (1999), the computations incorporate a mesh redistribution algorithm, which creates new elements in regions of high strain and locally redistributes the vorticity field into a smaller number of elements when particles tend to cluster. Instead, global remeshing is used in our scheme. In his results, the growth is not too much but can be discernible. He attributed the small deformation to the ring remaining laminar within the duration of the computation because the indication of the almost constant dynamic model coefficient and the constant turbulent eddy viscosity is that the single, isolated ring is not turbulent. The small growth is not due to the inhibiting of the LES turbulence model.

However, our current method of adding the divergence term into regular three-dimensional particle method captures the substantial growth of the perturbed vortex ring under the moderate Reynolds number $\mathrm{Re}_\Gamma = 2200$, and the extent of growth is very clear in Figure 4.9 (without SGS model) and Figure 4.10 (with SGS constant Ch^4 / t_o = 2.5e-6) [for a comparison, surface of constant vorticity magnitude is plotted at the same time interval as that of Mansfield et al. (1999)]. Besides, an illustration of kinetic energy is plotted in Figure 4.11. Our numerical results of kinetic energy both without SGS model and with SGS model seem lower than that of Mansfield et al. (1999), and a possible reason is due to frequent global remeshing in our method, which dissipates the kinetic energy together with the molecular viscosity. The fact that lower

kinetic energy and the stronger extent of growth indicates the additional divergence term is very necessary for the three-dimensional particle method to simulate the perturbed phenomena. Neglecting the term, the fluctuation can't be correctly captured because of divergence-not-free, which is a weak point for the approximation of particle method.

As for the acting role of the SGS model, it is apparent when comparing the ISO surface of Figure 4.9 and Figure 4.10. The SGS model plays the role of smoothing the results by removing the unfavorable stuff and inconsistent directional growth caused by the spatial coarse resolution. Furthermore, the implementation of the SGS model doesn't modify the correct results, which is validated through the illustration of kinetic energy of Figure 4.11. These results agree well with the intention of the starting SGS model.

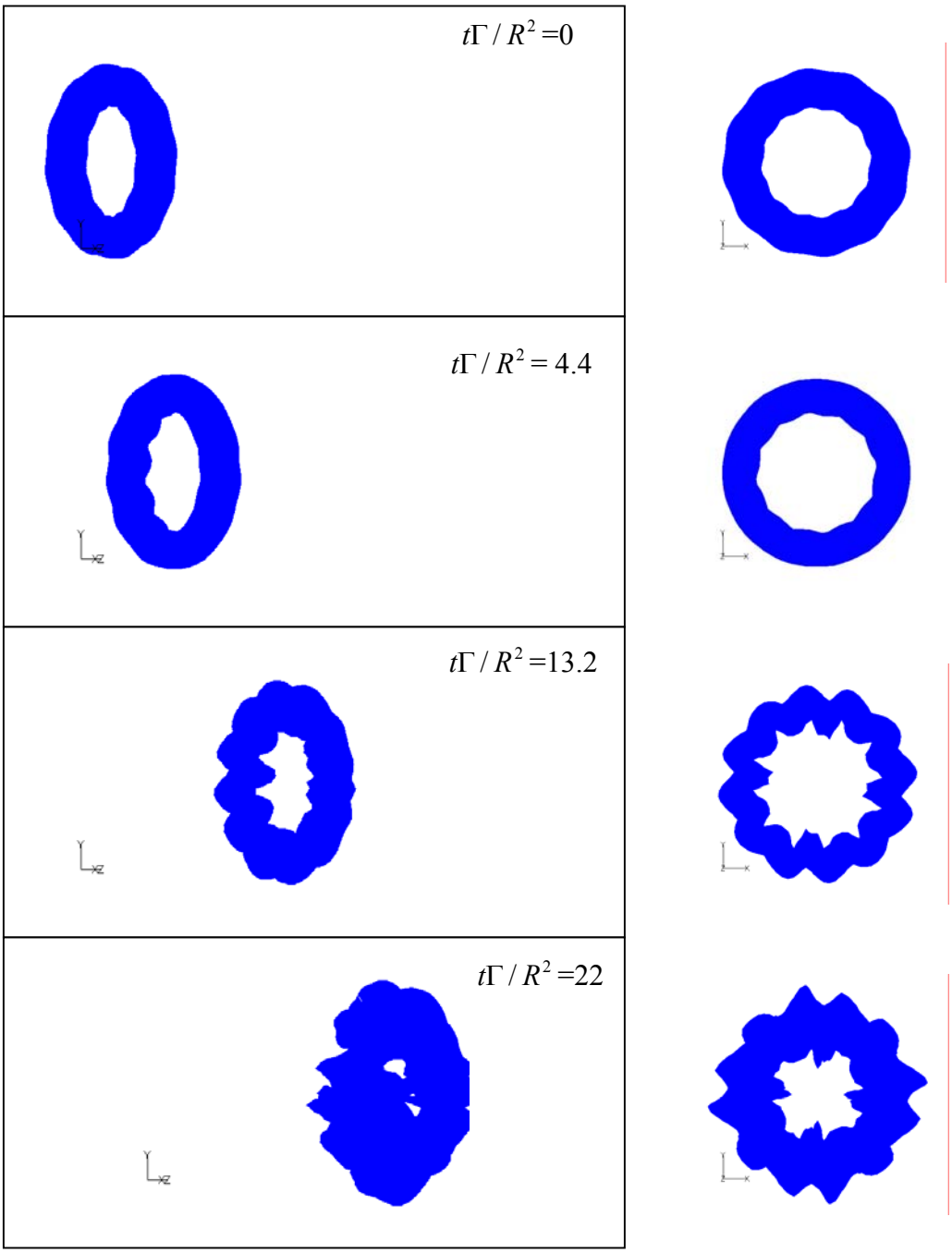

Figure 4.9 Bottom and perspective views of ISO-vorticity surface of magnitude $|\omega| R^2 / \Gamma = 1.82$ **at time** $t\Gamma / R^2$ **= 0, 4.4, 13.2, 22 (from top to bottom) without SGS model**

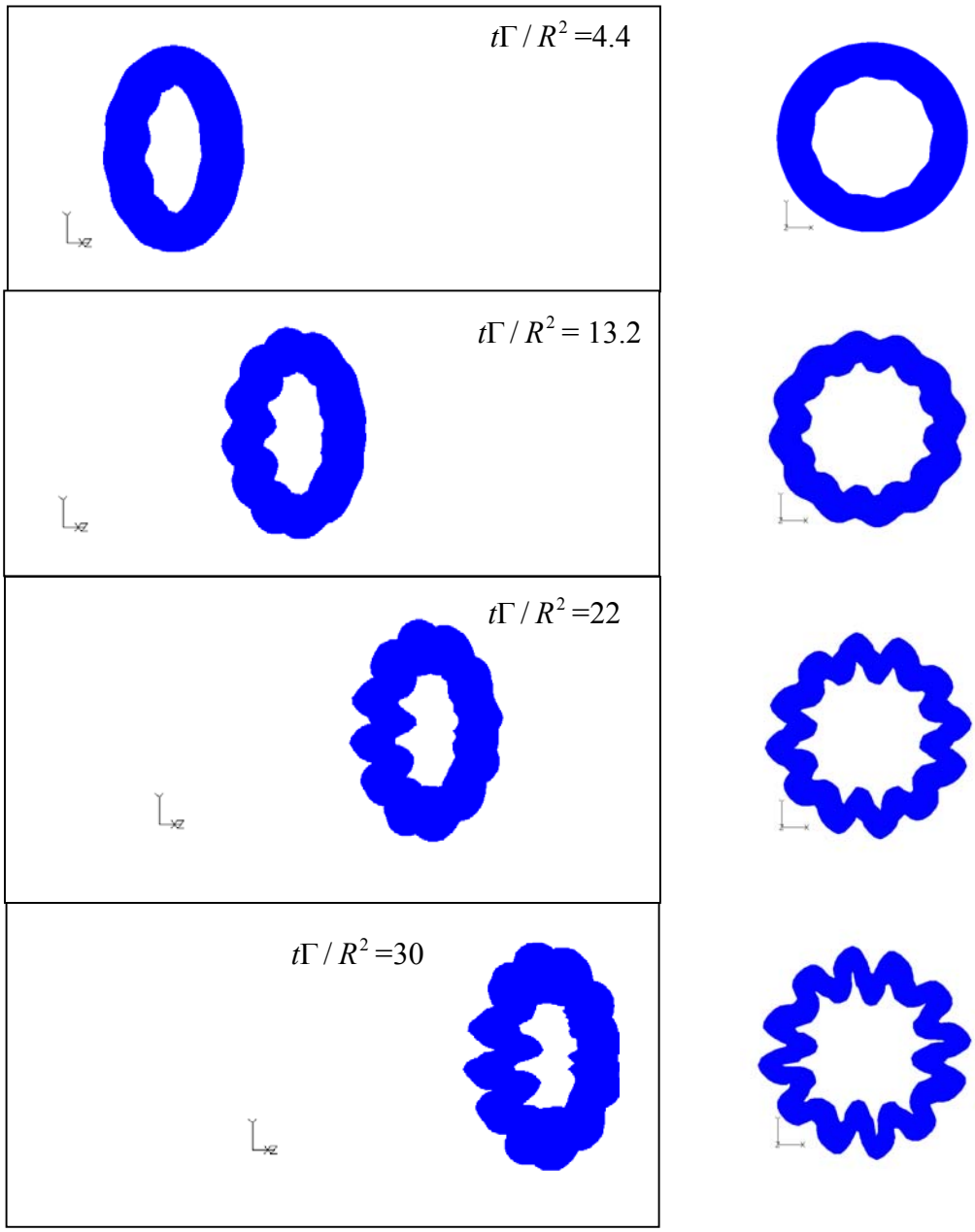

Figure 4.10 Bottom and perspective views of ISO-vorticity surface of magnitude $|\omega|R^2/\Gamma = 1.82$ **at time** $t\Gamma / R^2$ **= 4.4, 13.2, 22, 30 (from top to bottom) with SGS model**

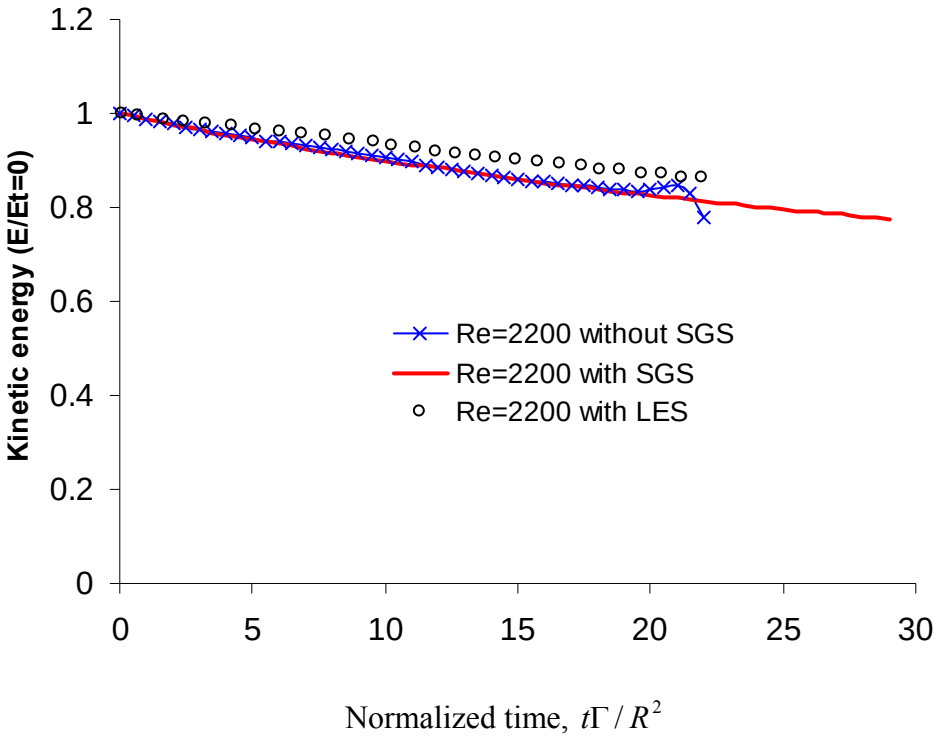

Figure 4.11 Kinetic energy ($E/E_{t=0}$) of a perturbed vortex with wave number n = 12. Re=2200 with LES is the result of Mansfield et al. (1999).

4.6 Formulation of Vortex Sound for Three-dimensional Flow

Computational techniques for flow-generated sound can be classified into two categories. One is to perform direct numerical simulation (DNS) to resolve all flow scales including the small dissipative scales. However, because of its high computational cost, its use is limited to simple flow configurations at low to moderate Reynolds numbers. Another way is to obtain far-field sound by integral or numerical solutions of acoustic analogy equations using computed source field data. The method assumes that the flow is at low fluctuating Mach numbers, and the sound waves do not affect the flow in any significant way.

The first acoustic analogy was due to Lighthill (1952) who rearranged the exact continuity and momentum equations into a wave equation with a source term on the right-hand side. Howe (1975) presented the acoustic perturbation p for quadrupole source at a point y as

$$p = \frac{\rho_o}{4\pi c^2 |\mathbf{y}|^3} \frac{\partial^2}{\partial t^2} \int (\mathbf{y} \cdot \mathbf{x}) \mathbf{y} \cdot (\boldsymbol{\omega} \times \mathbf{u})(\mathbf{x}, t - \frac{|\mathbf{y}|}{c}) d\mathbf{x}, \tag{4.21}$$

where $\boldsymbol{\omega} \times \mathbf{u}$ is the source term, which enables the acoustic field to be found by integration only over regions where voriticity is nonzero.

Actually, Mohring (1978) presented the acoustic perturbation in a form that does not contain the flow velocity for a quadrupole source

$$p(\mathbf{y}, t) = \frac{\rho_0}{12\pi c_0^2 |\mathbf{y}|^3} \frac{\partial^3}{\partial t^3} \int (\mathbf{y} \cdot \mathbf{x}) \mathbf{x} \cdot (\boldsymbol{\omega} \times \mathbf{y})(\mathbf{x}, t - |\mathbf{y}| / c_0) d\mathbf{x}, \tag{4.22}$$

Or

$$p(\mathbf{y}, t) = \frac{\rho_0 y_i y_j}{12\pi\, c_0^2 |\mathbf{y}|^3} \frac{d^3}{dt^3} Q_{ij}(t - |\mathbf{y}| / c_o), \tag{4.23}$$

where Q_{ij} is given by the second-order moments of voriticity

$$Q_{ij}(t) = \int x_i (\mathbf{x} \times \boldsymbol{\omega})_j (\mathbf{x}, t) d\mathbf{x}. \tag{4.24}$$

For the vorticity field with the particle discretization, the approach of the current work will be to derive appropriate formulation for the discrete vortex system. In our numerical simulation, the formulation of Howe (1975) is employed, which takes the following discretized form using particle approximation:

$$p = \frac{\rho_o}{4\pi c^2 |\mathbf{y}|^3} \frac{\partial^2}{\partial t^2} \sum_p (\mathbf{y} \cdot \mathbf{x_p}) \mathbf{y} \cdot (\boldsymbol{\alpha_p} \times \mathbf{u_p}). \tag{4.25}$$

The acoustic pressure of an inviscid vortex ring with a Kirchhoff elliptic core has an analytical solution given by (Howe 2003)

$$p \approx \frac{\rho_o U^4}{8\pi^3 c_o^2} \frac{R(3\cos^2\theta - 1)}{|\mathbf{x}|} \frac{a-b}{a+b} \cos[\frac{2\Gamma}{\pi(a+b)^2}(t - \frac{|\mathbf{x}|}{c_o})]. \qquad (4.26)$$

In the following numerical cases, the variables are made dimensionless using a characteristic length R and vortex circulation Γ such that

$$\tilde{a} = a/R,\ \tilde{t} = t\Gamma/R^2,\ \tilde{\alpha} = \alpha/(\Gamma R),\ \tilde{p} = pR^2/(\rho\Gamma^2),\ M = \Gamma/(c_o R). \qquad (4.27)$$

Therefore, the acoustic equation at far-field may be rewritten as

$$p = \frac{M^2}{4\pi|\mathbf{y}|^3} \frac{\partial^2}{\partial t^2} \sum_p (\mathbf{y}\cdot\mathbf{x_p})\mathbf{y}\cdot(\boldsymbol{\alpha}_\mathbf{p} \times \mathbf{u_p}). \qquad (4.28)$$

The simulated results using the vortex particle method and the far-field formula are compared in Figure 4.12. It can be seen that the agreement is excellent, showing that the far-field formula is correctly implemented.

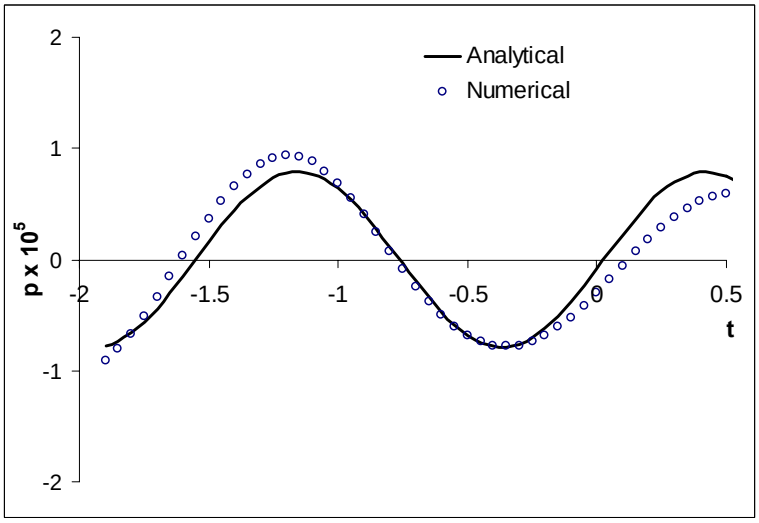

Figure 4.12 Comparison of far-field pressure between numerical simulation and analytical result for an unperturbed inviscid vortex ring with an elliptic core.

4.7 Acoustic Sound Radiated From a Perturbed Vortex Ring

When a vortex ring is perturbed, the local unsteady motion of the vortex ring appears due to the imbalance between the self-induced perturbation wave rotation and the mean induced vortex ring velocity. Therefore, a perturbed vortex ring is expected to radiate sound. Leung et al. (2001) investigated the evolution and sound radiation of a slender vortex ring with weak perturbation in free space by using the vortex filament method. The slender vortex ring with invariant vortex core has the characteristics of linear long wave instability when subject to weak sinusoidal perturbations (Widnall and Sullivan 1973). In the results of Leung et al. (2001), both stable and unstable evolutions radiate sound in the far field. In addition, they found that a stable perturbed vortex ring radiated stronger sound than an unstable one. Obviously, the sound they observed came from the weak perturbation.

In the present research of acoustic sound radiated from a perturbed vortex ring, the vortex core, which is represented by a number of particles, are deformable. Sound radiated from a perturbed vortex ring with a deformable core is expected to be different from what was described by Leung et al. (2001).

The current case involves an inviscid perturbed vortex ring with the same vorticity distribution as described in the preceding section (third order Gaussian distribution) with the same parameters: $a/R = 0.275$, $R = 1$, $\Delta x = 0.07$, $\Delta t = 0.05$, $\Gamma = 1$. But here the disturbance amplitude is set as $A = 0.03$. This case was used by Knio and Ghoniem (1990) to study the dynamics of a perturbed vortex ring. Their results show that when n is equal to 8 or 9, the evolution of the perturbed vortex ring is stable while it is unstable when n is equal to 11 or 12. In the following study of acoustic sound radiated by a perturbed vortex ring, these wave numbers

are chosen. Also note that the far-field position $\boldsymbol{y}$ (0,100,0) is chosen for the calculation of acoustic sound produced by the perturbed vortex ring (see Figure 4.1).

Figure 4.13 and Figure 4.16 present the results of the time history of far-field pressure for a perturbed vortex ring with different wave numbers. Stage I is a transient period, which is not included in the spectral analysis. Detailed acoustic analysis is performed at Stage II. In this stage, it is clear that the magnitude of pressure for wave number n = 8, 9 is bigger than that for n = 11,12. Actually, from Figure 4.18, one can find that the perturbation with wave number n = 12 grows in the radial direction causing substantial non-uniform deformation around the ring, and the growth is almost at an exponential rate while the growth with n = 8 is negligible. However, it seems that the vortex ring with the most unstable mode only radiates weaker sound in the far field than the ring with the stable mode. When the evolution reaches Stage III, the perturbed vertex ring with n = 11,12 breaks into turbulence and the magnitude of pressure increases quickly. During this stage, the current numerical scheme becomes unstable. Figure 4.14 compares the results of the time history of far-field pressure with the different time step size under inviscid flow. Evidently, with reduced time step size, the far-field pressure still increase quickly at the stage III, which indicates that the simulation indeed becomes numerically unstable at the stage. However, the difference between the two results is negligible before t = 14, indicating the stage II is reliable for acoustic analysis. In addition, the curve of the kinetic energy in Figure 4.15 also validates the conclusion. After t = 14, the kinetic energy starts to grow bigger. This is also an indication that the scheme becomes numerically unstable.

To understand more about Stage II, a simulation with Re = 2200 is implemented. In Figure 4.13, because the growth rate is reduced due to the viscous effect, the stage II has longer time history. From the longer time history, one can be sure that the vortex ring under the most

unstable wave number radiates weak sound. However, for n = 8, 9, the vortex ring appears to be stable. Obviously, the local unsteady periodic motion of the perturbed vortex ring still continues even under the stable mode.

An analysis of frequency is performed in Figure 4.17. In this figure, both the stable motion with n = 8 and the most unstable motion with n = 12 radiate two distinct peaks in the frequency domain. It is apparent that the magnitude of pressure at the higher-frequency peak for n = 12 is smaller than that for n = 8. This agrees with the observations by Knio and Ghoniem (1990) and Leung et al. (2001) that the perturbation at the most unstable mode only generates weak sound in the far field of a vortex ring. Therefore, the higher-frequency peak is related to the forced perturbation. The lower-frequency peak in the figure should be related to the deformation of the vortex core. As we know, an unperturbed vortex ring with an elliptic core is able to radiate sound. The vortex core of the perturbed vortex ring is mostly deformed into an elliptic-like core due to the perturbation around azimuthal direction. In Figure 4.19, contours of ω_y in the y = 0 symmetry plane at time $t\Gamma / R$ = 11 for a perturbed vortex ring are compared for the cases of wave number n = 8 and n = 12. When the vortex ring is under the most unstable mode, the core deformation is large. This provides the explanation that the magnitude of pressure at the lower-frequency peak in Figure 4.17 for n = 12 is bigger than that for n = 8.

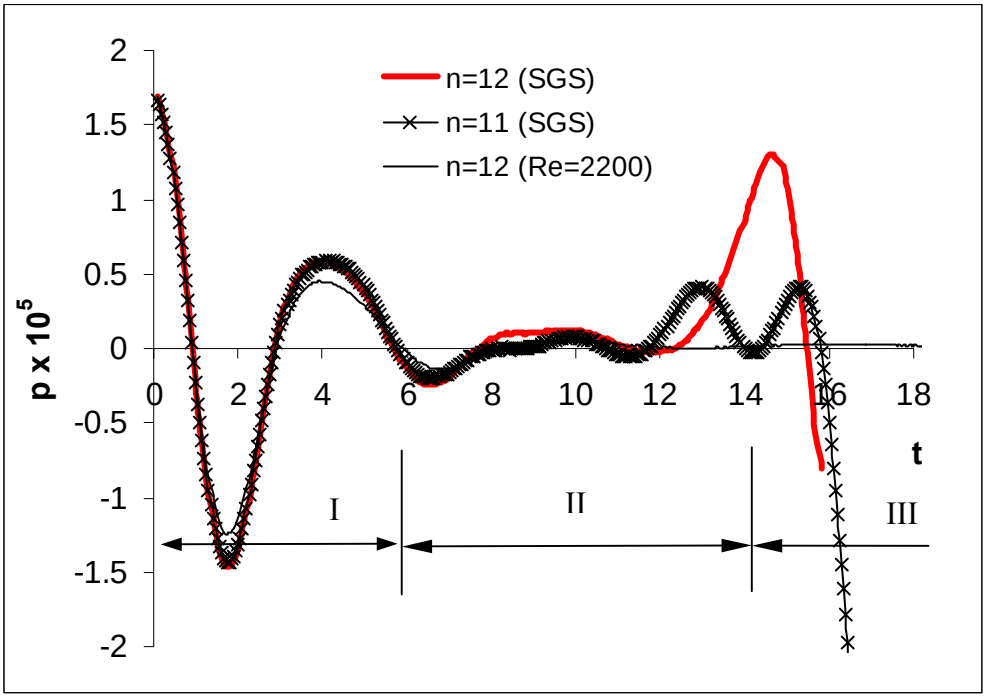

(a)

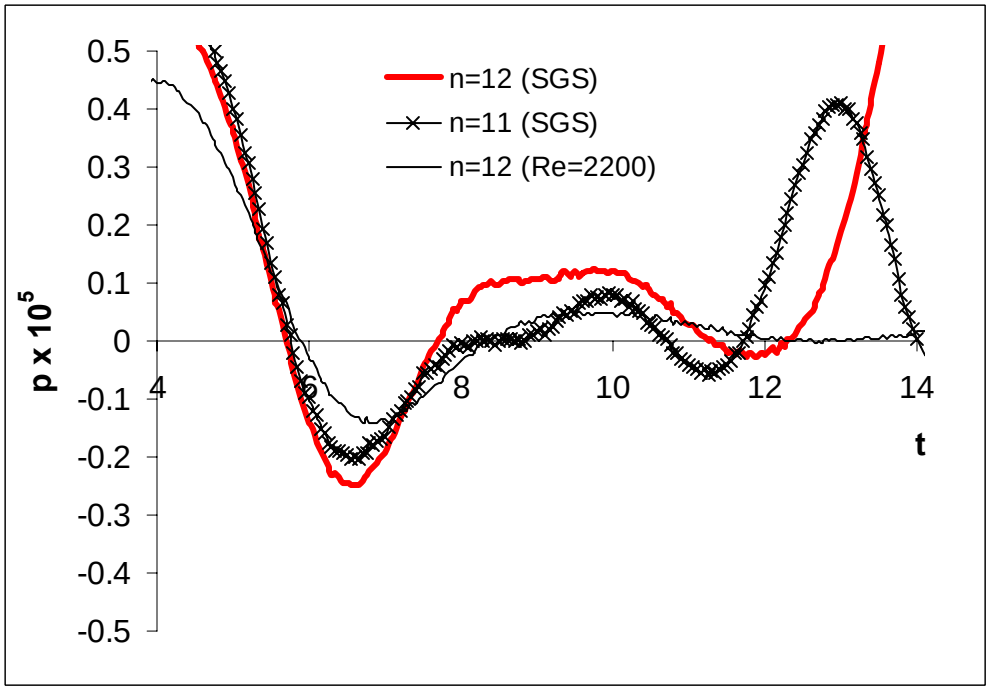

(b)

Figure 4.13 Far-field pressure in the time domain for a perturbed vortex ring with unstable evolutions: (a) time history from 0 to 20; (b) time history from 4 to 14

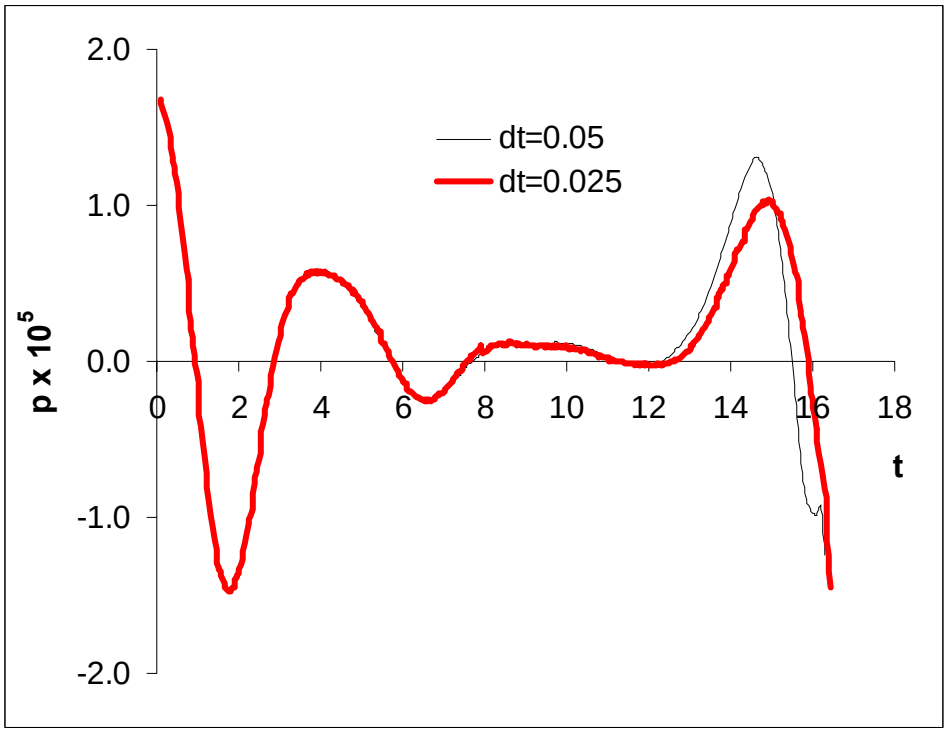

Figure 4.14 Far-field pressure in the time domain for a perturbed vortex ring (*n* = 12)

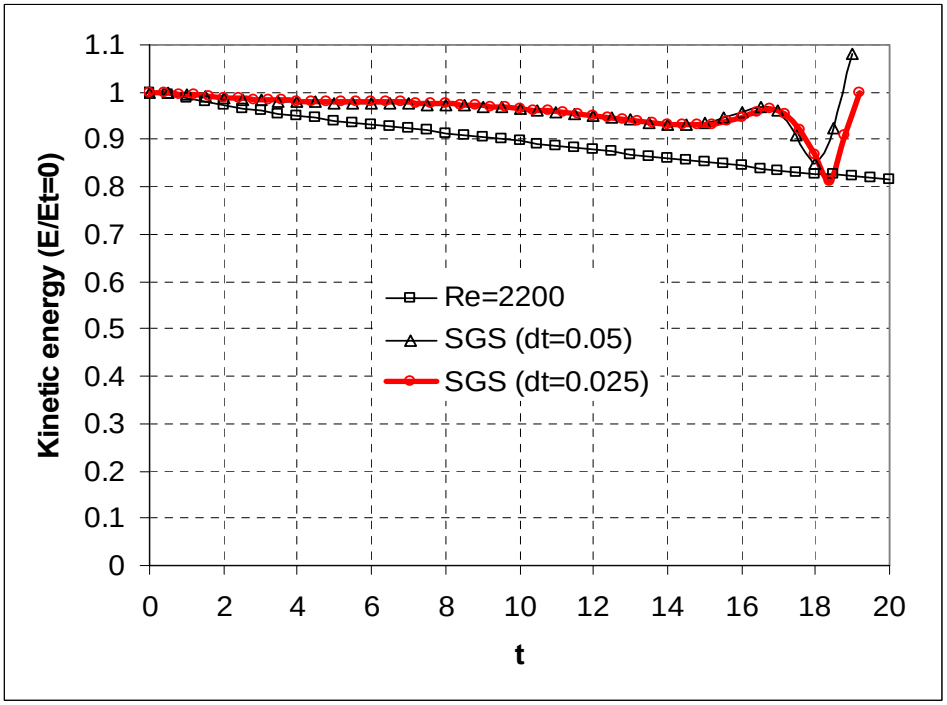

Figure 4.15 Kinetic energy ($E/E_{t=0}$) of a perturbed vortex with wave number *n* = 12.

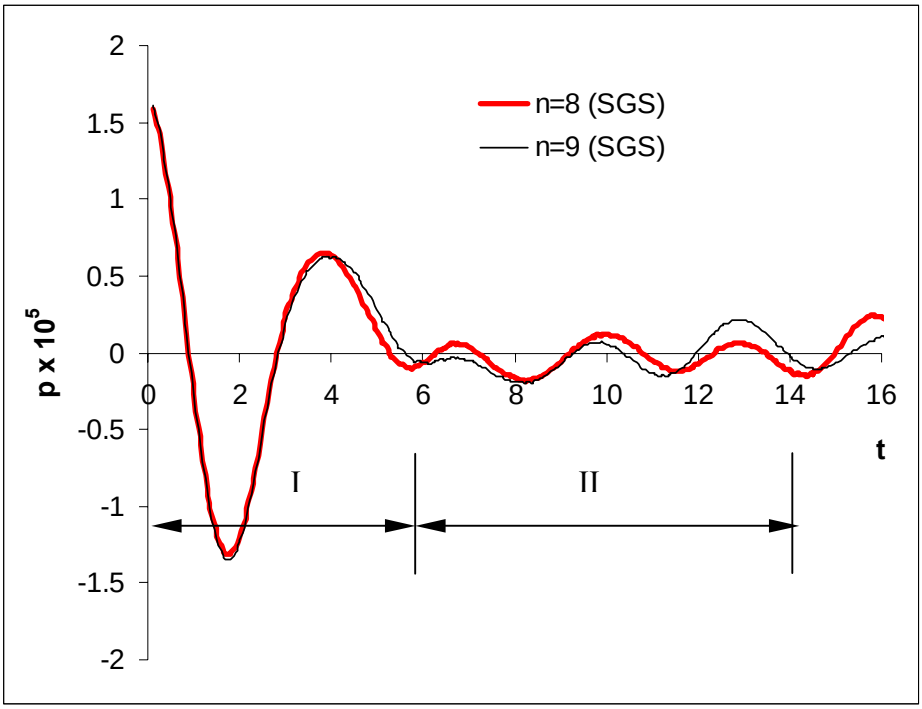

Figure 4.16 Far-field pressure in the time domain for a perturbed vortex ring with stable evolutions

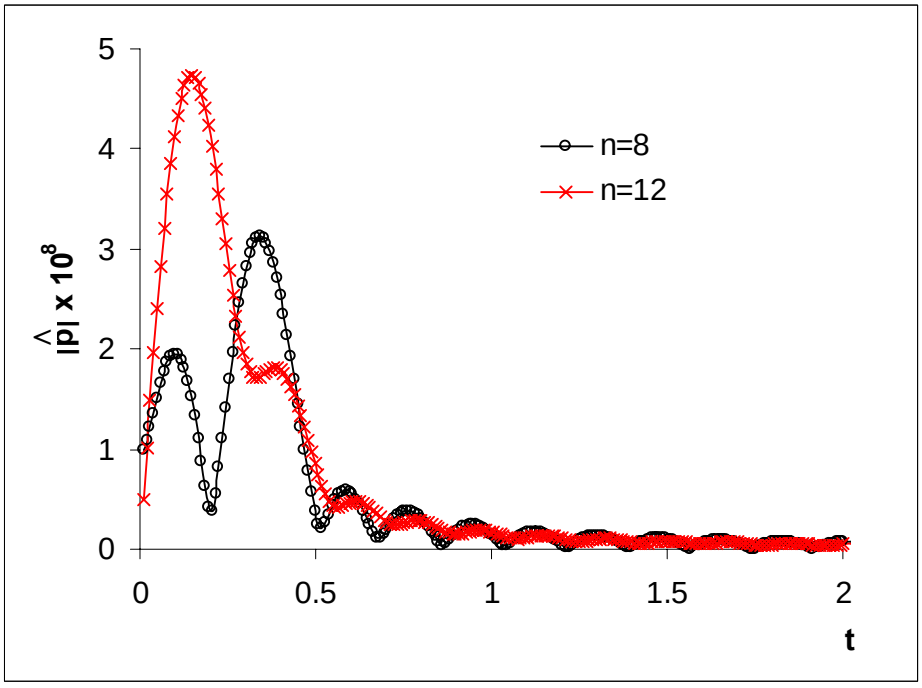

Figure 4.17 Far-field pressure in the frequency domain for a perturbed vortex ring

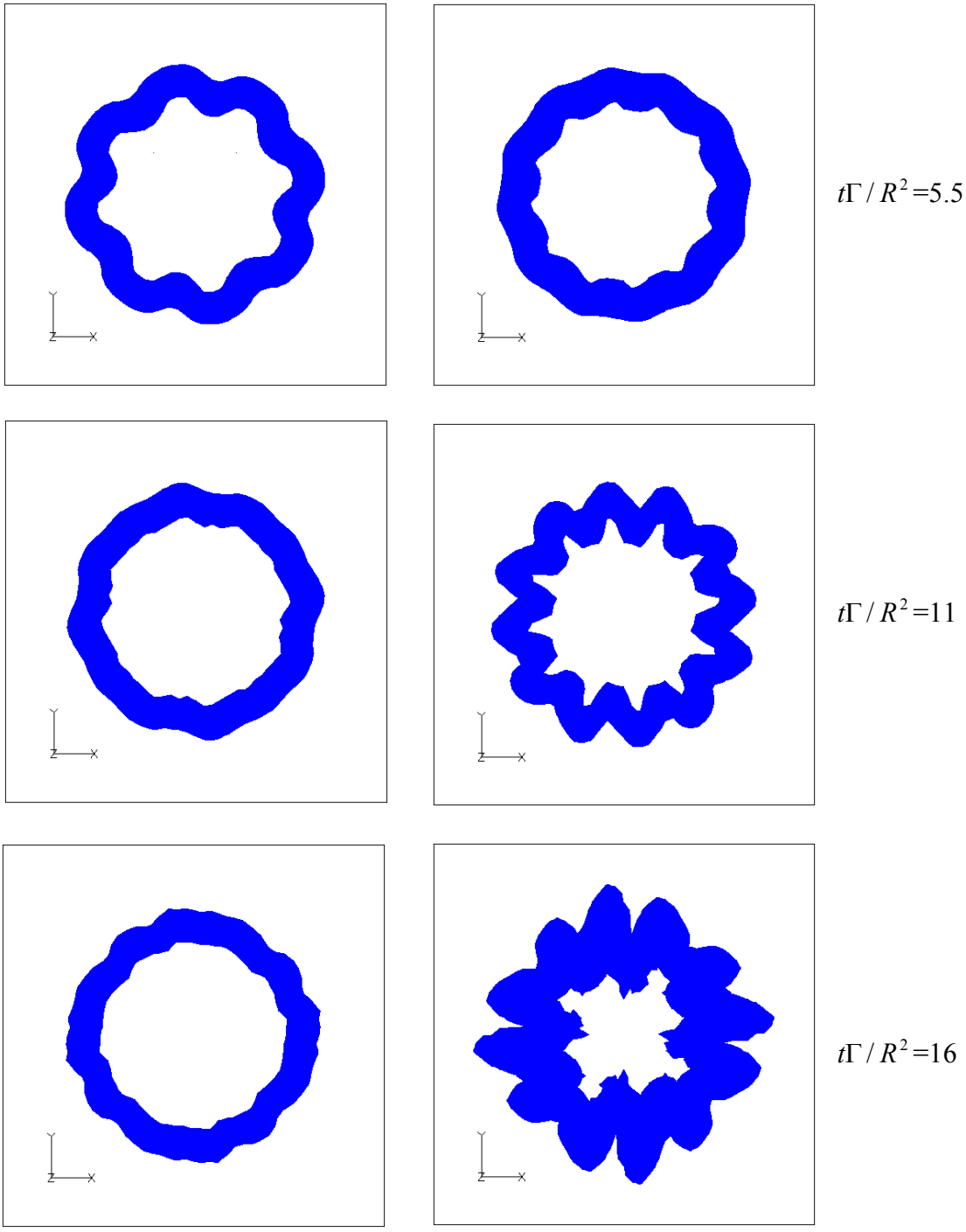

Figure 4.18 Bottom views of ISO-vorticity surface of magnitude $|\omega|R^2/\Gamma = 3$ at time $t\Gamma / R^2$ = 5.5, 11 and 16 with SGS model: (a) wave number *n* = 8;(b) wave number *n* = 12

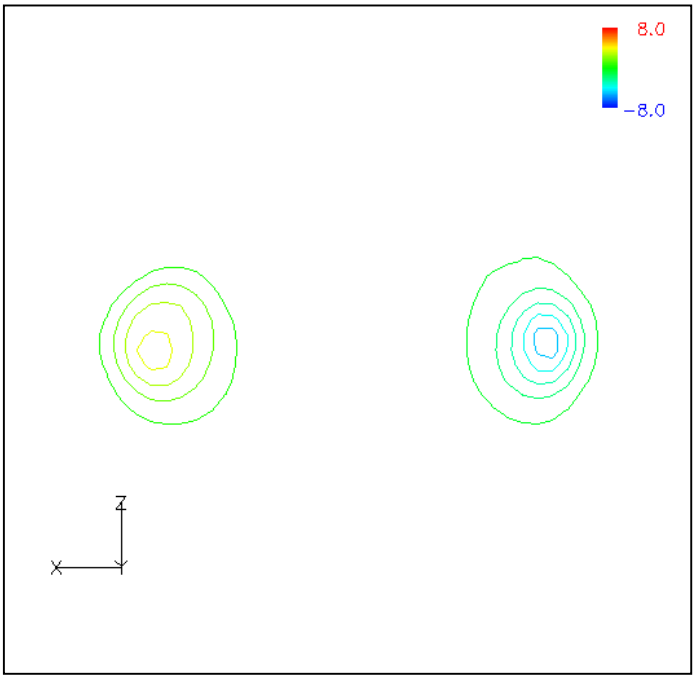

(a)

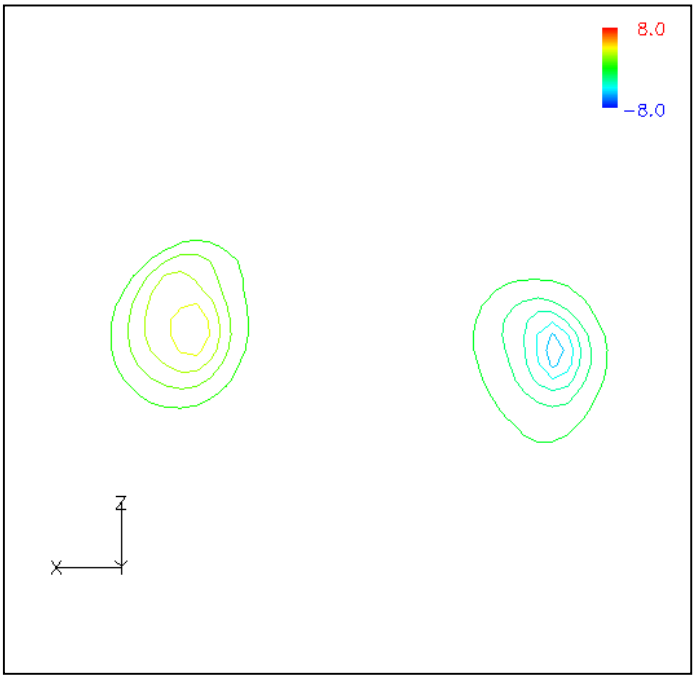

(b)

Figure 4.19 Contours of ω_y in the y=0 symmetry plane at time $t\Gamma / R^2$ = 11 for a perturbed vortex ring: (a) wave number *n* = 8; (b) wave number *n* = 12

4.8 Summary and Discussion

In this work, a traditional three-dimensional vortex particle is modified to simulate a perturbed vortex ring under inviscid and viscous conditions. The addition of the divergence term $\mathbf{u}(\nabla \cdot \boldsymbol{\omega})$ is nevertheless required to help capture the small magnitude produced by fluctuated phenomena. The scheme combines a hyper-viscosity sub-grid scale model to remove the effect due to coarse spatial resolution and smooth the numerical results. At the same time, the SGS model also compensates for the insufficiently small dissipation produced by the global remeshing for the purpose of diffusing the numerical error due to divergence-not-free problems. Because of that, the numerical simulation could be run for a long time. The numerical result of a perturbed vortex ring for inviscid flow and viscous flow validates the above conclusions.

Sound radiated by a perturbed vortex ring is also discussed in this chapter. A steady vortex ring with a Gaussian core does not radiate any sound. When a perturbation is imposed at the azimuthual direction of the vortex ring, two distinct peak frequencies appear for both the stable mode and unstable mode. The higher-frequency peak is related to the forced perturbation. The lower-frequency peak is related to the deformation of vortex core. As we know, an unperturbed vortex ring with elliptic core is able to radiate sound. Mostly, the vortex core of the perturbed vortex ring is mostly deformed into an elliptic-like core due to the perturbation around azimuthal direction. A stable perturbed vortex ring tends to radiate stronger sound than an unstable one at the higher frequency peak.

5 Dynamics and Sound Production by Wake Vortex

It has been shown that vorticity in a vortex core relates to the frequency of a significant sound peak from an aircraft wake vortex pair, in which each of the vortices is modeled as an elliptic core Kirchhoff vortex. This has been studied in Chapter 2 for a counter-rotating pair and in Chapter 3 for a multiple vortex system. Also, a perturbed vortex ring has been found to radiate acoustic sound, which is discussed in Chapter 4.

In three-dimensional wake vortices, sinusoidal instabilities at various length scales result in significant flow structure changes in these vortices, and thus influence their radiated acoustic signals. In this study, a modified three-dimensional vortex particle method coupled with the SGS model, which were described in Chapter 4, is used to simulate the incompressible vortical flow – wake vortex. The flow field, in the form of vorticity, is employed as the source in the far-field acoustic calculation using a vortex sound formula that enables computation of acoustic signals radiated from an approximated incompressible flow field.

Because the counter-rotating vortex pair represents one of the simplest flow configurations for the study of elementary vortex interactions and these vortices due to their strength and longevity can be dangerous to other aircraft that follow, cases of a pair of counter-rotating vortices are studied in this chapter when they are undergoing both long-wave and short-wave instabilities. Both inviscid and viscous interactions are considered and the effects of turbulence are simulated using sub-grid-scale models.

5.1 Dispersion Relations

It has been observed (Scorer and Davenport 1970) that the vortex wake does not decay by viscous diffusion, but instead develops a sinuous instability that leads to the formation of vortex rings. Two kinds of instabilities are known to occur in vortex systems: a long-wavelength and a short-wavelength instability. The long-wave instability leads to the connection of the vortices and to changes in the flow topology (Crow 1970), whereas the short-wave instability distorts the vortices (Tsai and Widnall 1976).

The long wavelength is typically of the order of the distances between the different vortices of the wake, which was analyzed first by Crow (1970) on a single pair of trailing vortices. Using a linear perturbation analysis of a pair of trailing vortices, Crow (1970) found that the wavelength of the most unstable mode of instability could be found from the ratio of the radius (r_c) of the vortex cores to their separation distance (b_o). Although both long-wave and short-wave instabilities are shown in Crow's analysis, it is was pointed out later by Widnall et al. (1974) that the short-wave results are spurious because the expression for the self-induced rotation of these perturbations, used in Crow' calculations, is asymptotically valid for long waves only. The evolution of the sinusoidal instabilities leads to vortex reconnection to form vortex rings. Once the rings have formed, the wake quickly degenerates into a harmless smaller-scale turbulence. The persistence of coherent flow depends mainly on the growth rate of the instability that precedes the formation of vortex rings.

The short wavelength instability results from the stretching of perturbations whose wavelength is typically of the order of the vortex core radius. The short wave instability was discovered simultaneously by Moore and Saffman (1975) and Tsai and Widnall (1976). Later, this kind of instability was observed in both laboratory experiments (Leweke and Williamson

1998, Ortega et al. 2003) and in numerical simulations (Orlandi et al. 1998, Nomura et al. 2006). They identified this phenomenon as a manifestation of a cooperative elliptic instability, which has a length scale comparable to the vortex core size and a growth rate that can exceed that of the Crow instability. The growth of the short wavelength gives rise to secondary transverse vortex structures, which lead to rapid pinch-off of vortices and transition to turbulence.

A numerical analysis of dispersion relations using the thin-tube vortex method by Zheng (2002) was introduced here in order to set stable and unstable cases for further study of the two kinds of instabilities when using vortex particle methods. In the thin-tube vortex simulation (Zheng 2002), it was assumed the vortex core doesn't change its size and structure during the simulations. It was also assumed that in the thin-tube vortex method the core vorticity changes due to the stretching and shrinking of the vortex segment.

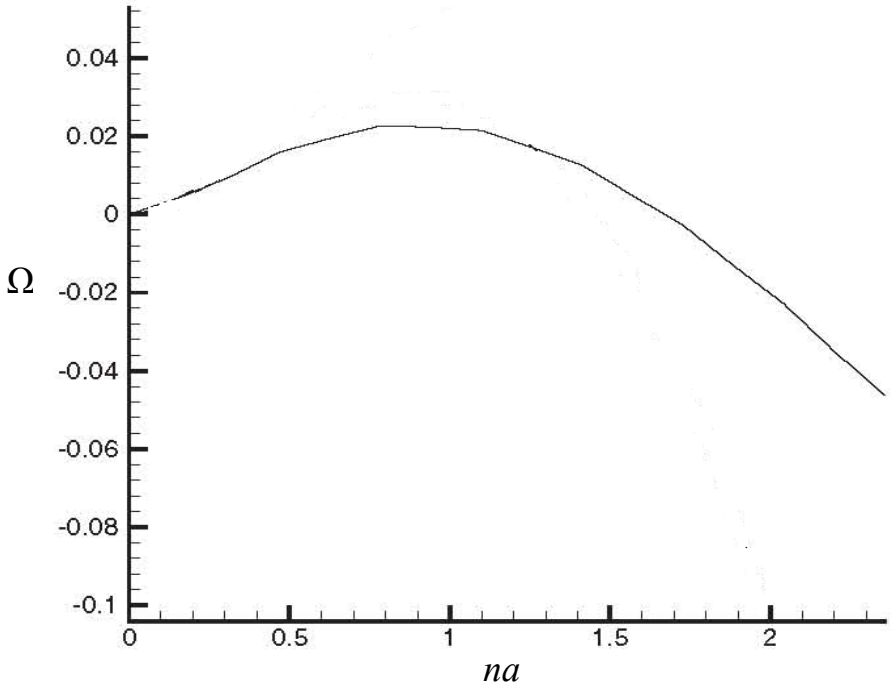

Figure 5.1 Dispersion relations using a thin-tube vortex method (Zheng 2002).

In Crow's paper, because of a dispersion relation, around the zero self-induction frequency is the region where the unstable sinusoidal wave can possibly develop. Based on these analyses and assumptions, Zheng (2002) observed that a second zero of the rotating frequency is na = 1.72 (see Figure 5.1), which may be viewed as short wave instability. Note that in Figure 5.1, n is the wave number and a is the vortex core size. Regarding long-wave instability, it is obvious that the first zero (at na = 0) is where the instability occurs. This is illustrated and proved by the numerical result of the thin-tube method in Figure 5.1. Therefore, the setting of $na \to 0$ should be viewed as long wave instability. In the following section, n = 7 and a = 0.25 (the wave length is 0.898) is configured to perform a numerical simulation of short wavelength instability for a counter-rotating vortex pair while n = 0.75 and a = 0.25 (the wave length is 8.38) is studied as a numerical simulation of long wavelength instability for the vortex pair.

Zheng (2002) also compared his numerical result of dispersion relations with the long wave instability analysis of Crow (1970) and the short-wave instability analysis of Moore and Saffman (1975). The reader may refer to the paper of Zheng (2002) for more details.

In the following sections, the long- and short-wave sinusoidal perturbations are simulated to investigate the influence from the dispersion relations.

5.2 Description of Numerical Cases

The study of elementary vortex flows has received much attention over the last decade. In order to understand the importance of these structures and their behavior, it is very necessary to analyze their elementary dynamics in simple flows containing a single vortex or a small number of interacting vortices. A pair of counter-rotating parallel vortices, which is the object of this study, is one of the most basic examples of such flows. The classic configuration of the counter-rotating pair or vortex tubes is presented in Figure 5.2. The circulation of each tube of axis Oz is

Γ_o, and the spacing is b_o. The radius of each tube for which the distribution of vorticity is Gaussian or constant is a. The case is periodic in the two ends along the z axis. In the x and y directions, the exact far-field boundary condition is applied.

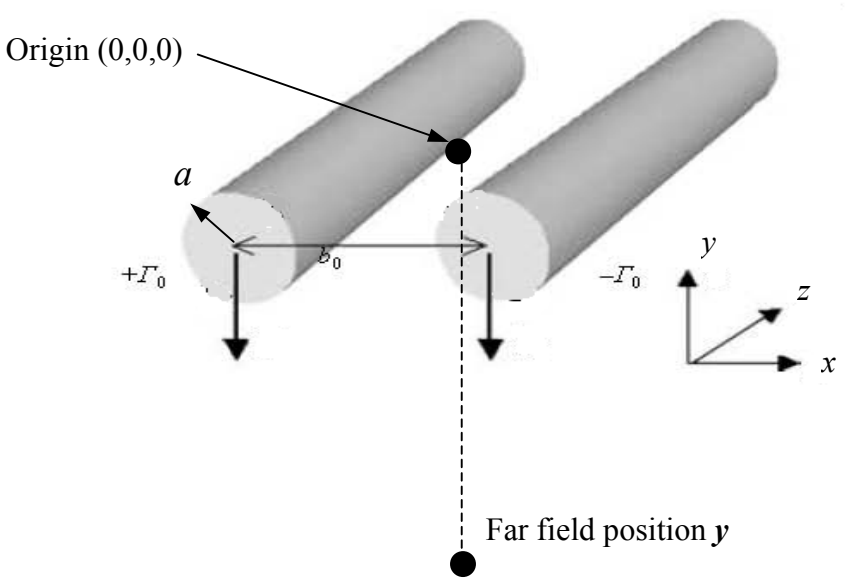

Figure 5.2 Illustration of a counter-rotating wake vortex pair

The vortex pair is initially perturbed with a sinusoidal displacement in two directions x, y and the amplitude of the symmetrical perturbation is A

$$x_c = b_o / 2 + A\sin(nz) \quad y_c = A\sin(nz), \tag{5.1}$$

$$x_c = -b_o / 2 - A\sin(kz) \quad y_c = A\sin(kz), \tag{5.2}$$

where n is the wave number. Since the x and y directions are specified with the same disturbances, the initial planar standing-wave angle, defined as $\theta = \tan^{-1}(A_y / A_x)$, is 45°.

The wake vortex may be initialized with a Gaussian vorticity distribution at $r_c(x_c, y_c)$,

$$\omega_z = \frac{\Gamma}{\pi a^2}\exp\left\{-\frac{(r - r_c)^2}{a^2}\right\}. \tag{5.3}$$

The vorticity distribution may also be viewed as the Kirchhoff vortex, which is a patch of constant vorticity, ω_z, inside the ellipse and zero voriticity outside. It is an exact solution of the 2-D, incompressible, and inviscid flow equations (Lamb 1975). An almost circular Kirchhoff vortex has the ellipse defined by the polar equation for the radius of the vortex core as

$$R = a(1+\varepsilon\cos(2\theta)), \tag{5.4}$$

where the long axis of the ellipse is $a(1+\varepsilon)$, the short axis is $a(1-\varepsilon)$. The ellipse rotates at an angular velocity of $\omega/4$, which generates a quadrupole-type sound at a frequency of $\omega/4\pi$ when the single vortex is under 2D flow (Howe 2003). The reader can refer to Section 2.4.1 for more description about the Kirchhoff vortex.

In the following numerical cases, the variables are made dimensionless using a characteristic length b_o and vortex circulation Γ such that

$$\tilde{a} = a/b_o,\ \tilde{t} = t\Gamma/b_o^{\,2},\ \tilde{\alpha} = \alpha/(\Gamma b_o),\ \tilde{p} = pb_o^{\,2}/(\rho\Gamma^2),\ M = \Gamma/(c_o b_o). \tag{5.5}$$

Therefore, the acoustic equation at far field may be rewritten as

$$p = \frac{M^2}{4\pi|\mathbf{y}|^3}\frac{\partial^2}{\partial t^2}\sum_p (\mathbf{y}\cdot\mathbf{x_p})\mathbf{y}\cdot(\boldsymbol{\alpha}_\mathbf{p}\times\mathbf{u_p}). \tag{5.6}$$

In the following numerical calculation of far-field acoustics, the near field region containing the wake vortex is a source region and the far-field position $\boldsymbol{y}$ is (0,100,0) (see Figure 5.2).

5.3 Computational Formulation

In order to investigate the sound generation by aircraft wake vortices, engineering models of the phenomena based on the Lagrangian discrete vortex method are developed. Since these phenomena are inherently vortical in nature and the noise sources are mainly vorticity-generated

pressure waves, the vortex method is therefore particularly well suited and very efficient in describing the fundamental fluid mechanics. As a result of a compact vorticity source, the flow field can be split into an inner and an outer domain, and the flow within the outer domain can be considered irrotational. Furthermore, to compute far-field noise, the assumption that compressibility effects remain small enough and Mach number is low ($M << 1$) is often introduced.

The fundamental of the three-dimensional vortex particle method was described in Section 4.1 and Section 4.2. Below is a summary of the method to be used to simulate wake vortex flow:

$$\frac{d\mathbf{x}_p}{dt} = \mathbf{u}(\mathbf{x}_p, t) = \sum_q K_\sigma(\mathbf{x}_p - \mathbf{x}_q) \times \alpha_q(t), \tag{5.7}$$

$$\begin{aligned} \frac{d\boldsymbol{\alpha}_p}{dt} &= (\boldsymbol{\alpha}_p \cdot \nabla)\mathbf{u}_p + \mathbf{u}_p(\nabla \cdot \boldsymbol{\omega}_p)V_p + \\ &\frac{2\nu}{\sigma^2}\sum_q \eta_\sigma^{lap}(\mathbf{x}_p - \mathbf{x}_q)(V_p\boldsymbol{\alpha}_q - V_q\boldsymbol{\alpha}_p) - V_p\frac{C}{t_o}(h^2\nabla_h{}^2)^2\boldsymbol{\omega} \end{aligned}. \tag{5.8}$$

5.4 Periodic Boundary Condition for the Three-dimensional Flow

Although the vortex particle method includes the far-field boundary condition automatically, it is necessary to impose a periodic boundary condition on the direction of the vortex axes (the z axis). For wake vortices with the initialization of sinusoidal perturbations along the vortex axis, a common approach is to truncate the domain at a long distance where the end effects on the center portion become minimal. However, such an approach would only allow vortex evolution short in duration without getting errors at the center portion. In addition, a long distance in the axial direction wastes a lot of computational resources. Therefore, the periodic boundary condition needs to be specified at both ends of the longitudinal direction. The Biot-

Savart integration, thus, has to be carried over an infinite number of periodic images. This can be done analytically in two dimensions (Pozrikidis 2001). However, no such analytical expressions for the three-dimensional flow are known.

In the study of sinusoidal instability in a counter-rotating vortex pair using the thin-tube vortex method (vortex filament) by Zheng (2002), the nearest-neighbor-image concept (Ashurst and Meigburg 1988) was implemented to reduce the end effects on the center portion of the domain when time marching proceeds.

Besides, Singer (1995) derived a formulation of periodic boundary condition especially adapted for the Fast Multipole Method (FMM) (Greengard and Rohklin 1987) which decomposes the element population spatially into clusters of particles and build a hierarchy of clusters to form a cluster of the next size up in the hierarchy and so on, reducing an operation count to O(MlogN) from initial O(MN).

Since we do not implement FMM to speed up the numerical calculation, and a MPI parallel algorithm is applied for the purpose instead (see Appendix B for details), the nearest-neighbor-image method is used here to consider the periodic boundary condition along the vortex axes. However, the concept is combined into our current vortex particle method, and not the vortex filament method used in the paper by Zheng (2002). Therefore, there are some differences in the implementation.

The concept can be illustrated in Figure 5.3, in which different images of the particles are taken into account. For example, the particle at Zq has two periodic images at Zq1 and Zq2. To evaluate the velocity of the particle at Zm, the image at Zq1 is taken and the image at Zq2 is not taken because the image at Zq1 is closer to the evaluated particle at Zm than the image is at Zq2.

On the other hand, when the velocity of the particle at Zn is evaluated, the image at Zq2 is used for the same reason.

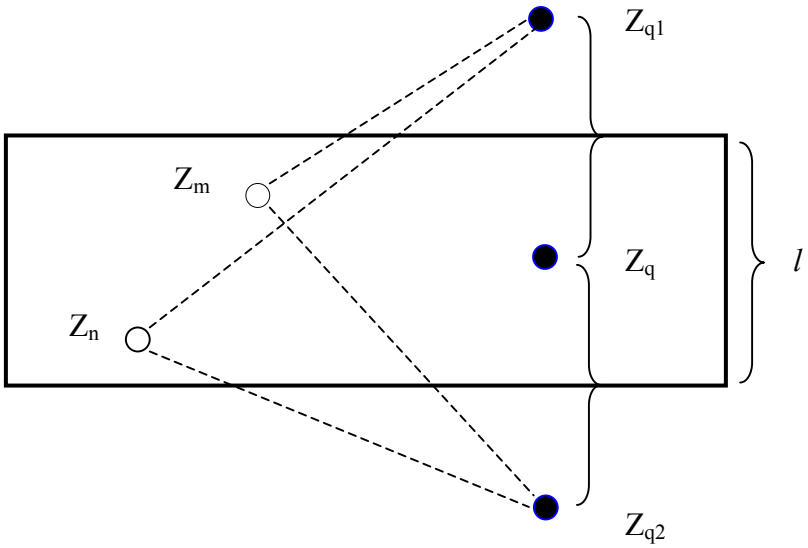

Figure 5.3 Illustration of the nearest-neighbor-image method by Ashurst and Meiburg 1988, where *l* is the simulation domain size at vortex axes (z – axis).

To verify the performance of the nearest-neighbor-image method implemented in the vortex particle method and to determine the necessary number of images required for the simulation, a counter-rotating wake vortex pair is tested. The wake vortex pair is configured with $a/b_o = 0.35,\ b_o = 2,\ \Delta x = 0.14,\ \Delta t = 0.2,\ \Gamma = 1$ and no perturbation is considered for the test.

To verify the performance of the nearest-neighbor-image method implemented in the vortex particle method and to determine the domain length required for the simulation, a non-perturbed, straight counter-rotating wake vortex pair is simulated. The wake vortex pair is configured with $a/b_o = 0.35,\ b_o = 2,\ \Delta x = 0.14,\ \Delta t = 0.2,\ \Gamma = 1$.

When the domain is truncated without considering a periodic boundary condition such as the nearest-neighbor-image method, the tails at the two ends are amplified as the time marching proceeds, as pointed out in Figure 5.4 (b).

The results in Figure 5.4 (a) shows that at any instant, the vortex structure remains unchanged as it is descending down, which means the method does not distort the vortex structure. The translational speed of an infinitely long vortex pair with cut-off function has an analytical solution:

$$V = \frac{\Gamma}{2\pi b_o} f(\frac{b_o}{\sigma}) . \tag{5.9}$$

For a Gaussian core of radius a/b_o = 0.35, the speed V = 0.07935. Test cases with the domain size l = 5.6, 9.8 and 14 result in translational speeds of 0.072, 0.0750 and 0.0758. Therefore, it may be concluded that to achieve an accuracy of $O(10^{-2})$ for the nearest-neighbor-image method, a minimum length of 9.8 is necessary. If the error of 4% is accepted, one may use the length of $l > 5.6$. It should be noted that such a conclusion applies only to current simulated counter-rotating pair structures. Other structures may result in different length requirements for the nearest-neighbor-image method.

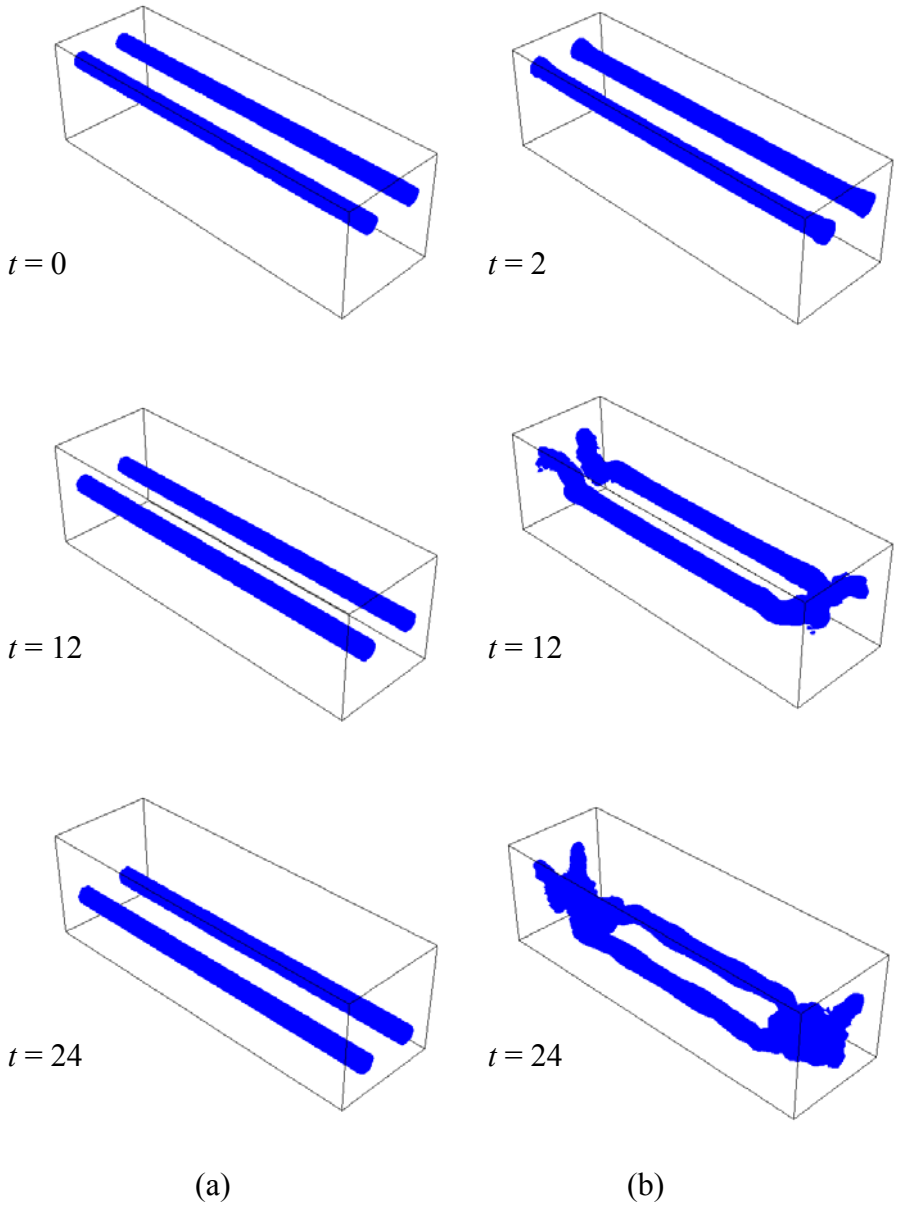

Figure 5.4 ISO surface of vorticity $|\omega| = 3$. (a) With the implementation of nearest-neighbour-image method; (b) Without the implementation of nearest-neighbour-image method;

5.5 Behavior and Acoustics of a Counter-rotating Vortex Pair under Short-Wave Instability

The following numerical discussion describes a counter-rotating vortex pair under short-wave instability. Since the acoustics of a vortex pair are tightly related to its transient behavior, its physical transient behavior is first explored and then the relative acoustics caused by the wake vortex are analyzed in detail.

The wake vortex pair is configured with $a/b_o = 0.25$, $b_o = 1$, $\Delta x = 0.0628$, $\Delta t = 0.05$, $\Gamma = 1$ and is initially perturbed with the disturbance amplitude $A = 0.05$.

5.5.1 Behavior of a Counter-rotating Vortex Pair under Short-wave Instability

The following cases are used to describe the behavior of a counter-rotating vortex pair with a Gaussian distribution core under short-wave instability, in order to understand easily the analysis of sound produced by the wake vortex in the next section. As discussed in Sec. 5.1, the most unstable modes are those for which the self-induced rotation is small or zero. For a vortex pair with $a = 0.25$, the unstable wave number is $n = 7$, which corresponds to a short-wave instability (wavelength is 0.898). The setting of na=1.75 corresponds to a second zero of the rotating frequency in Figure 5.1. Zheng (2002) studied the case using the vortex filament method and concluded that it is a short-wave unstable case. Since peculiar wave shapes emerge due to the overlapping of the vortex after some time interval, the simulation was terminated on purpose in the paper of Zheng (2002).

In Figure 5.5, as the flow with sinusoidal perturbation develops further, secondary structures are produced along the transverse direction and eventually dominate the flow as the primary wake vortex pair merges, breaks down, and is weakened. The phenomenon was also

observed by Leweke and Williamson (1998) and Nomura (2006). One may guess whether the developed secondary structure has any effect on the self-induced core rotation.

Furthermore, for comparison, a case with the wave number $n = 3$ is studied at a physically stable state and the result is illustrated in Figure 5.6. Obviously, when $na = 0.75$, the rotating frequency is 0.02 (see Figure 5.1), which is far from zero and should be viewed as physically stable according to theoretical study. The result agrees well with the study of Zheng (2002).

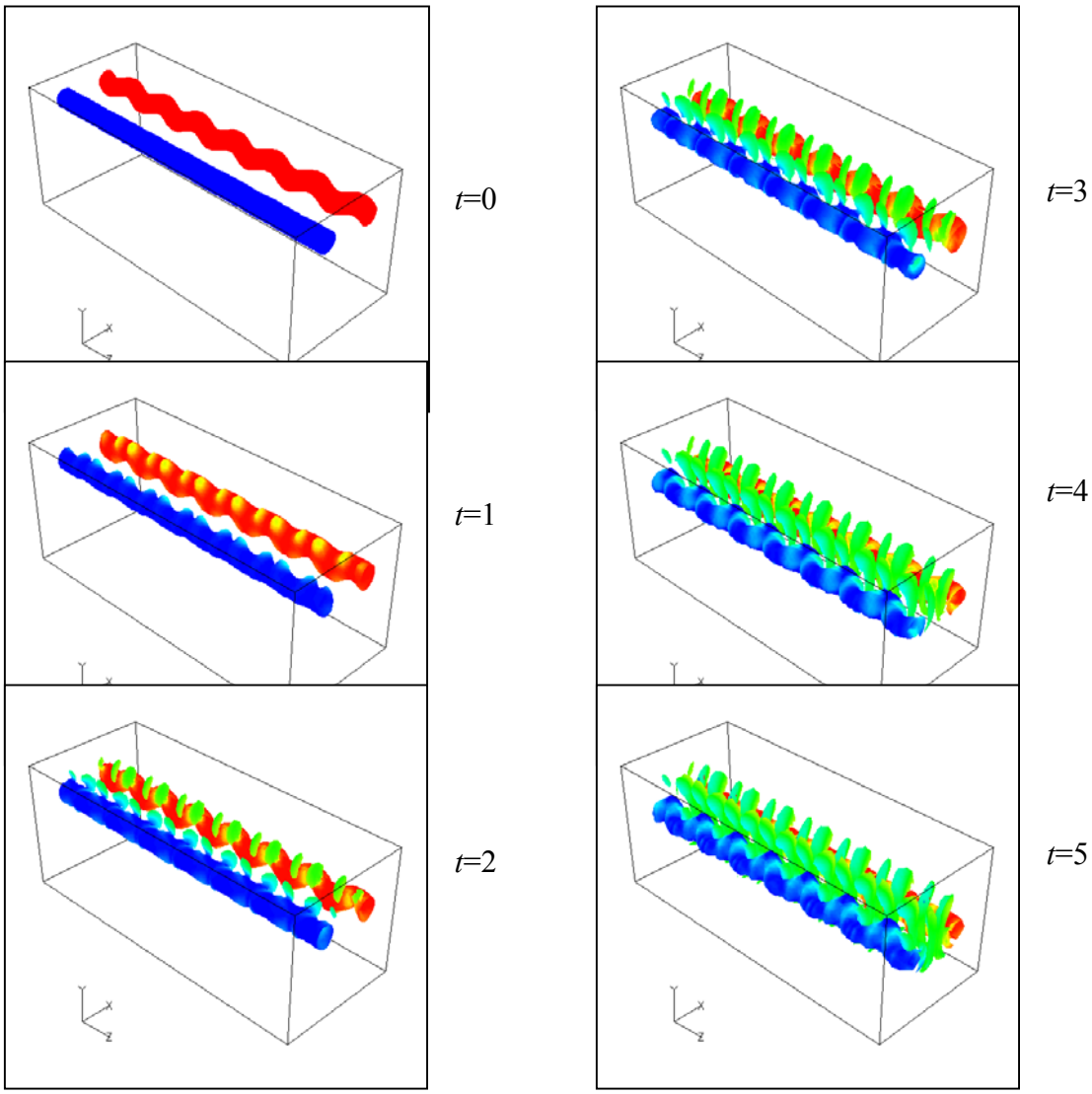

Figure 5.5 ISO surface of vorticity $|\omega| = 3$ for a vortex pair with short wave instability (n = 7) at t = 0, 1, 2, 3, 4 and 5.

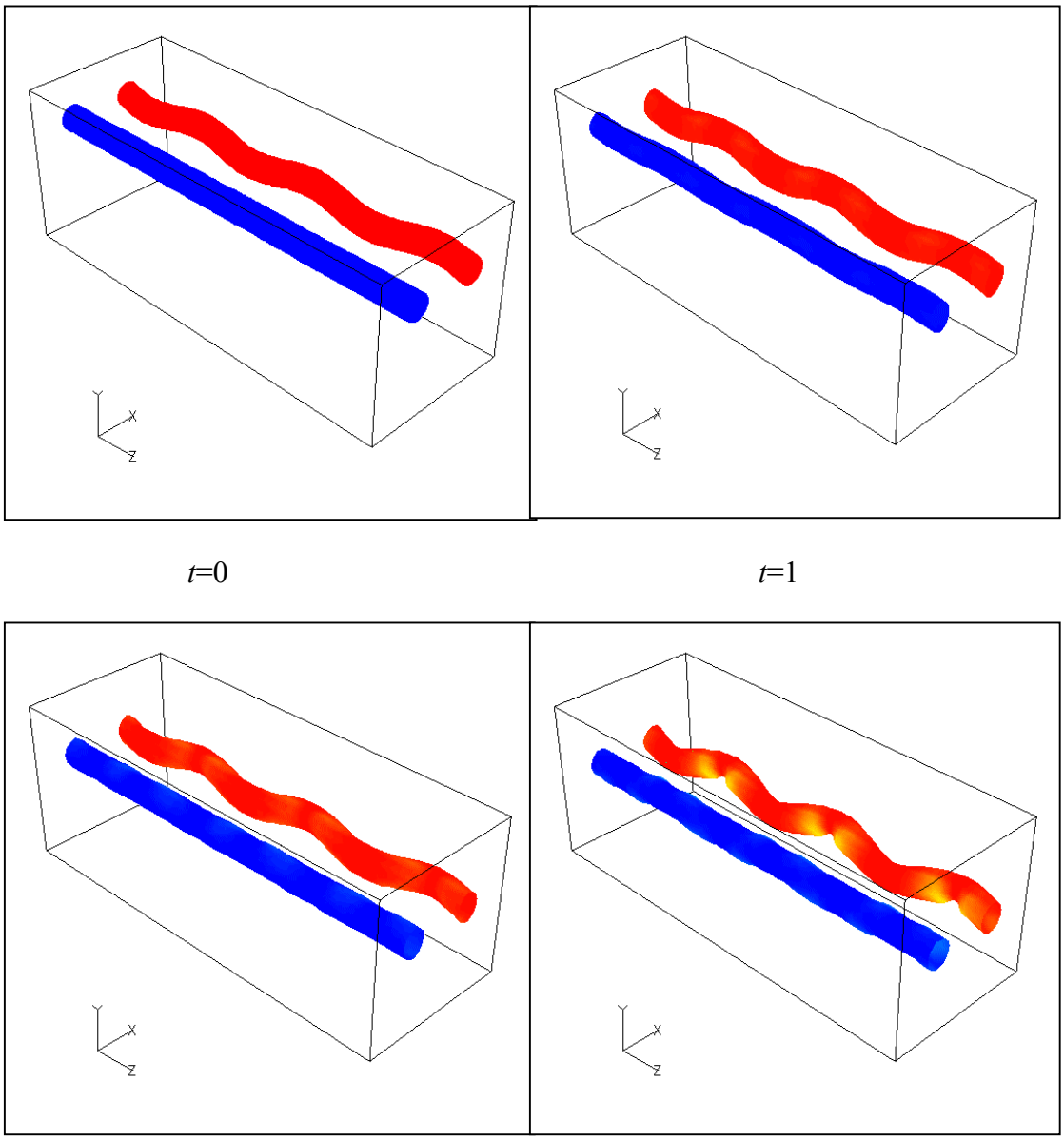

Figure 5.6 ISO surface of vorticity $|\omega| = 3$ for a vortex pair with short wave instability (n = 3) at t = 0, 1, 2 and 3.

5.5.2 Acoustic Sound Produced by a Counter-rotating Vortex Pair under Short-wave Instability

Before we go on to discuss acoustics, it is necessary to look at those factors affecting the vorticity in a vortex core, which is directly related to the frequency from an aircraft wake vortex pair. For a counter-rotating vortex system, the evolution of a vortex is due to the following effects: (i) the self-induced rotation and (ii) the induced velocity fields on this vortex due to the perturbations on the second vortex. The mutually induced velocity fields or mutual instability become strain fields, which drive the vortices together. In the presence of the externally imposed strain field induced by a second vortex, the self-induced rotation of one vortex can be diminished or augmented by the azimuthal velocity component of the strain field. When these two rotational components balance each other, the radial component of the strain field results in the large growth of amplitude and disturbance. The understanding of the mechanism of instability may help to analyze the acoustic sound of wake vortices.

Figure 5.7 and Figure 5.8 are illustrations of far-field pressure in the time domain and the frequency domain for the case of the wake vortex pair with the Gaussian distribution core while Figure 5.9 and Figure 5.10 are illustrations of far-field pressure in the time domain and the frequency domain for the case of the wake vortex pair with an elliptic core. From these figures, it is clear that wake vortices exhibit a periodic motion and produce one or two distinct peak frequencies. This occurs when the core is configured initially either as a round vortex with a Gaussian vorticity distribution or as a Kirchhoff elliptic core with constant voriticity inside the core. When the wake vortex pair occurs without perturbation, only one peak frequency appears. However, when a perturbation is imposed in the field, a higher peak frequency occurs that includes the lower peak frequency.

The initially round Gaussian vortex core is deformed to be an elliptic-like shape quickly because of the vortex stretching in a three-dimensional flow, which can be seen in Figure 5.14(d) and Figure 5.15. However, in a two-dimensional flow, it seems the deformation of the core occurs very slowly (Zheng et al. 2007). From Figure 5.15, the elliptic-like core performs self-rotation periodically. As discussed above, the vorticity in an elliptic core will radiate an acoustic signal. The peak frequency radiated by the elliptic core is almost 0.2 in Figure 5.8. In Figure 5.10, this initially elliptic vortex core rotation peaks approximately at the frequency of a Kirchhoff vortex of $\Gamma/[4\pi^2 a^2(1+\varepsilon)]= 0.37$. Obviously, when the initial round Gaussian vortex is deformed to be an elliptic-like core shape due to the mutual interaction, the core size is bigger than original core size *a*, and the bigger core radiates smaller peak frequency than that radiated from the wake vortices with initially elliptic core *a* (see Figure 5.12). However, the mutual interaction seems not to have a great influence on radiated frequency from the wake vortices with an initially elliptic core (see Figure 5.10). The above peak frequency is directly related to the self-rotation of elliptic core.

When the wake vortex pair with the Gaussian core is initially perturbed with a sinusoidal displacement, the straining field induced by the perturbation is imposed on vortex cores. The imposition causes the shape of the cores to change and results in significant flow structure changes, as well as changes in a significant peak frequency. In Figure 5.8, two kinds of peak frequency occur when the wake vortex system is initialized with perturbation. The lower frequency is related to the self-induced rotation accompanied with a steadily deformed elliptic-core shape due to mutual interaction. The frequency is almost the same as that for an unperturbed vortex pair. It seems that the mutual perturbation has only slightly negligible influence on the self-induced rotation. In Figure 5.16, the vortex cores are firstly deformed into elliptic shapes

and then are twisted and contorted. The gradually changed shape should be attributed to the mutual perturbation. Although the cores are contorted, self-induced rotation still exists. By comparing the iso-vorticity surface in Figure 5.13 (c) and (d) and Figure 5.14 (c) and (d), one may find out that, as the flow with sinusoidal perturbation develops further, secondary structures are produced along the transverse direction and eventually dominate the flow as the primary wake vortex pair merges, breaks down, and is weakened. The developed secondary structures may not affect the self-induced rotation; otherwise, the lower frequency should be different from that for unperturbed wake vortex pair. But the developed secondary structures contort the shape of the cores, as shown in Figure 5.16. It should be noted that for an unperturbed wake vortex pair, the straining field due to unperturbed mutual interaction from each vortex only causes the pair to go straight down, which doesn't produce any acoustic sound. The higher frequency in Figure 5.8 should be related to the contorted vortex core structure and the developed secondary structure due to sinusoidal instabilities. The higher peak frequency (in Figure 5.8, it approximates 0.5) is greater than the theoretical frequency of Kirchhoff vortex of $\Gamma/[4\pi^2 a^2(1+\varepsilon)]$=0.37 and the magnitude of the higher peak frequency is almost the same as the lower peak frequency.

When the wake vortex pair is initialized with a Kirchhoff vortex core (the eccentricity, ε, is 0.1 in the simulation), it can be predicted that the peak sound frequency corresponds to the elliptic core vorticity, a case that has been validated in two-dimensional flows (Zheng et al. 2007). In Figure 5.10, it can be seen, whether or not there are instability waves, this self-induced rotation of elliptic vortex core peaks approximately at the frequency of a Kirchhoff vortex of $\Gamma/[4\pi^2 a^2(1+\varepsilon)]$= 0.37. But when there are instability waves, the wake vortex pair with initially elliptic cores produces a higher frequency than the wake vortex pair with initially Gaussian cores

does. The higher frequency should occur due to the same mechanisms for initially Gaussian distribution core. The higher peak frequency due to mutual perturbation is much greater than the frequency of a Kirchhoff vortex of 0.37 due to the elliptic core, and the magnitude of far-field pressure at the higher peak frequency is almost half of that at the lower peak frequency. However, it should be noted that when the running time is beyond $t = 5$, the simulation becomes numerically unstable, which results largely from increasing of the pressure in Figure 5.9 and increasing of the kinetic energy in Figure 5.11. A corresponding viscous case is tested to make a comparison with the results under invsicd effect. The viscous effect, which smoothes the vorticity distribution, makes the core size increase in time, and reduces the perturbation rate; consequently, the two distinct peak frequencies in Figure 5.10 become smaller than the results under inviscid effect.

As for the higher magnitude of far-field pressure in the elliptic core case, it is attributed to the more concentrated vorticity distribution in an elliptic core than that in a Gaussian core. When a sinusoidal perturbation is considered in the simulation with an elliptic core, strong secondary structures are developed in the transverse direction (see Figure 5.13 (a) and Figure 5.14 (a)). However, the value of the higher peak frequency due to the instability is greater, compared to the value in the Gaussian-distribution-core case. A possible reason is that the highly concentrated vorticity distribution within an elliptic core accelerates the mutual motion caused by the disturbance, compared to the Gaussian core case. Therefore, the higher peak sound frequency is mostly determined by the mutual perturbation and vorticity distribution in the core.

In summary, two kinds of peak frequency exist in the perturbed wake vortex pair system, which are related to two different flow structures. The lower frequency is related to the self-induced rotation, which is not significantly influenced by the disturbance. The higher frequency

is related to core contortion and secondary structure due to mutual perturbation. The perturbation results in significant flow structure changes in the wake vortex system.

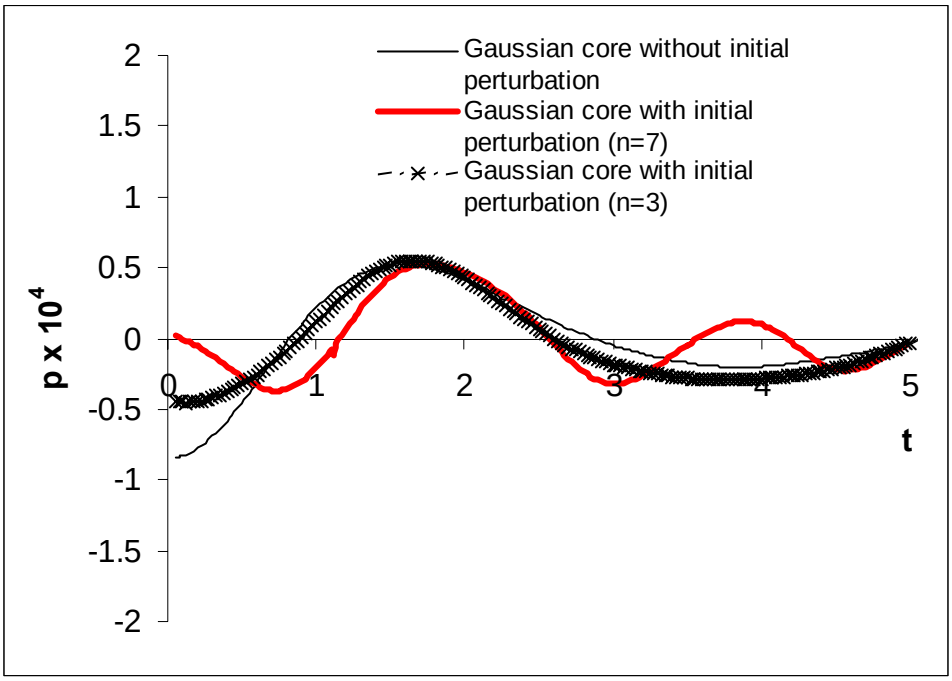

Figure 5.7 Far-field pressure in the time domain for wake vortex pair with Gaussian distribution core

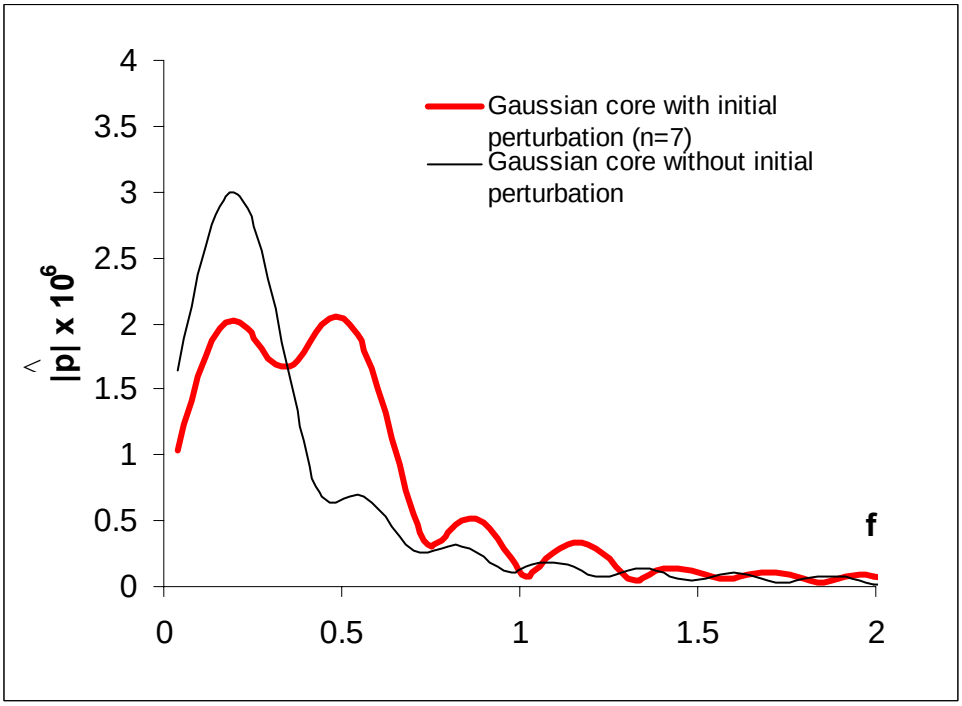

Figure 5.8 Far-field pressure in the frequency domain for wake vortex pair with Gaussian distribution core

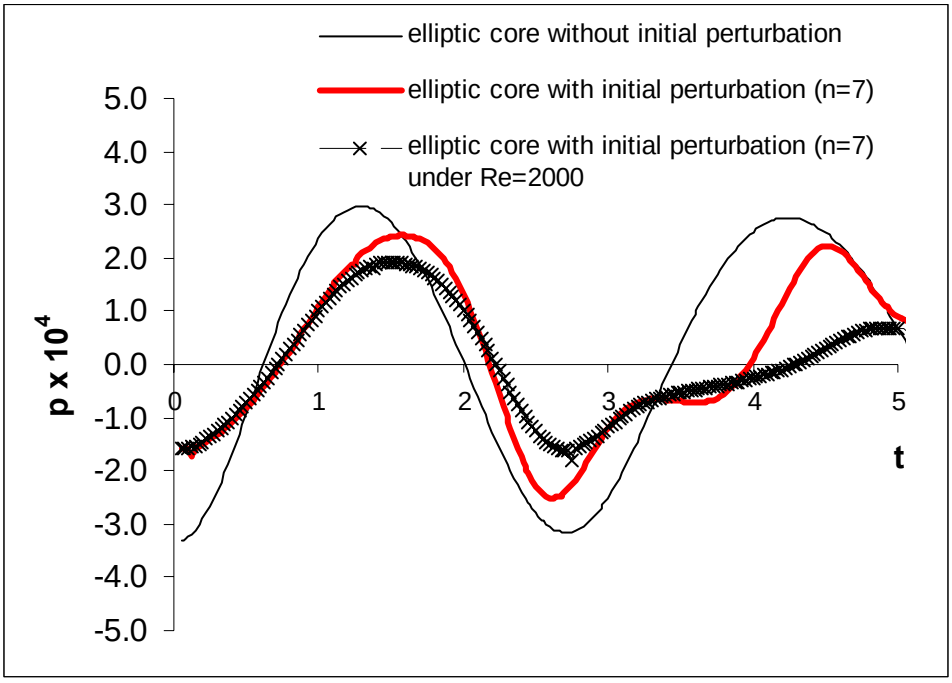

Figure 5.9 Far-field pressure in the time domain for wake vortex pair with elliptic core

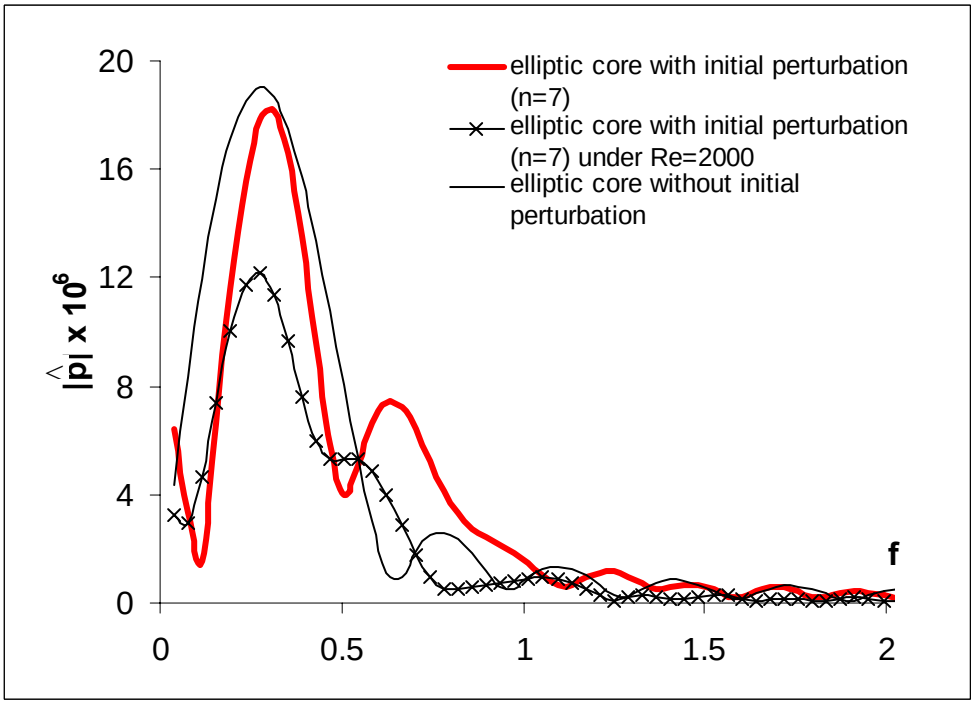

Figure 5.10 Far-field pressure in the frequency domain for wake vortex pair with elliptic core

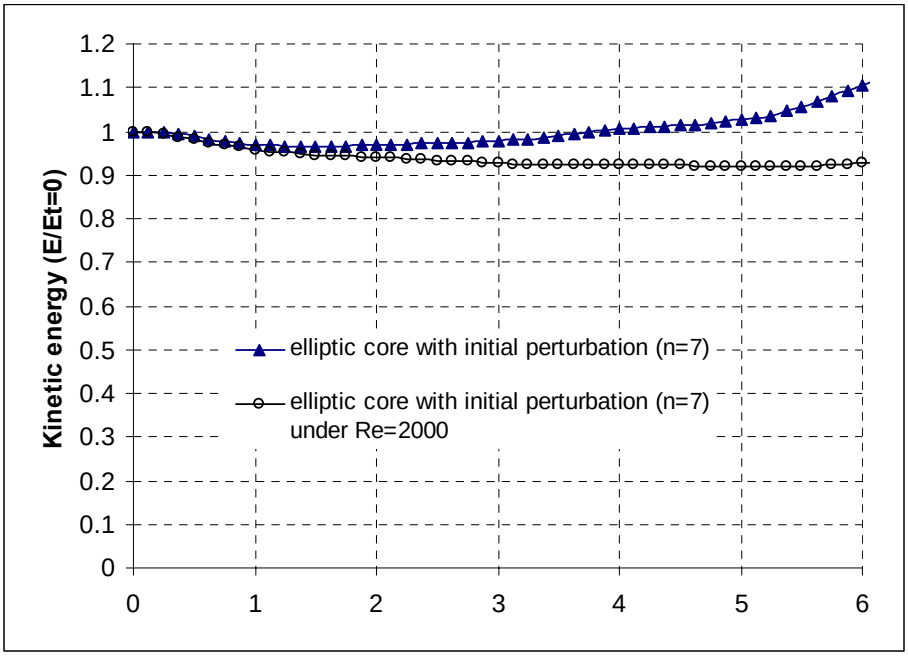

Figure 5.11 Kinetic energy ($E/E_{t=0}$) of a perturbed vortex pair (initially elliptic core) with wave number n = 7.

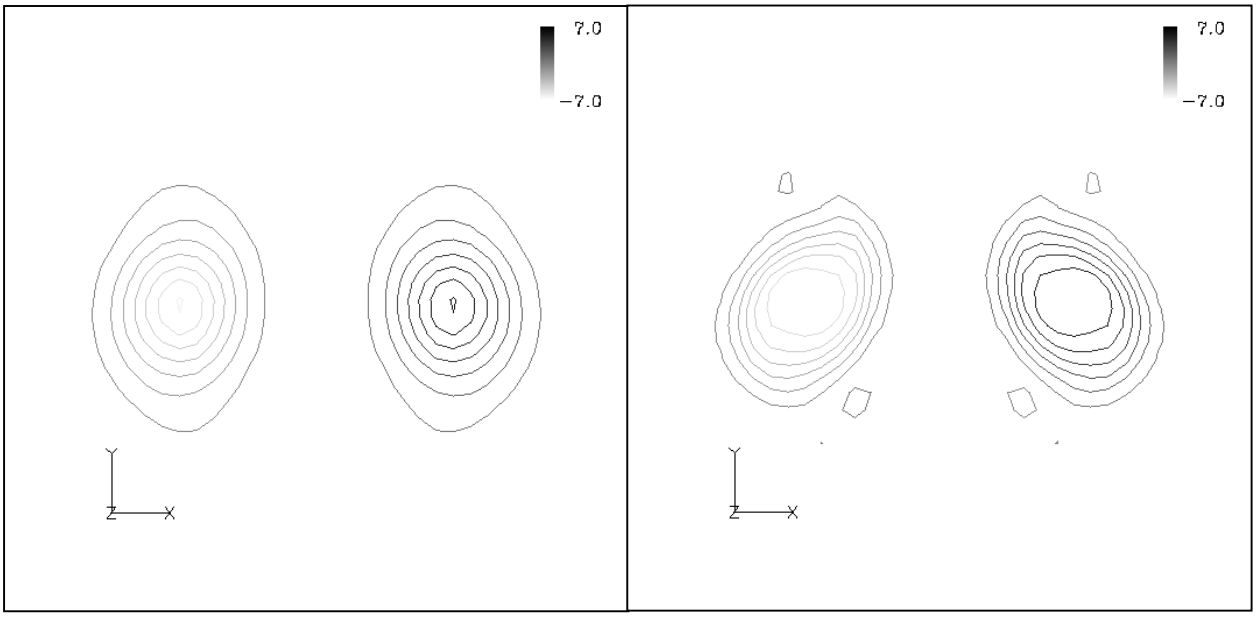

(a) (b)

Figure 5.12 Contours of ω_z in the z = 0 symmetry plane at time $t\Gamma / b^2$ = 2.25 for unperturbed wake vortex pair (SGS = 2.5e6): (a) initially Gaussian core; (b) initially elliptic core

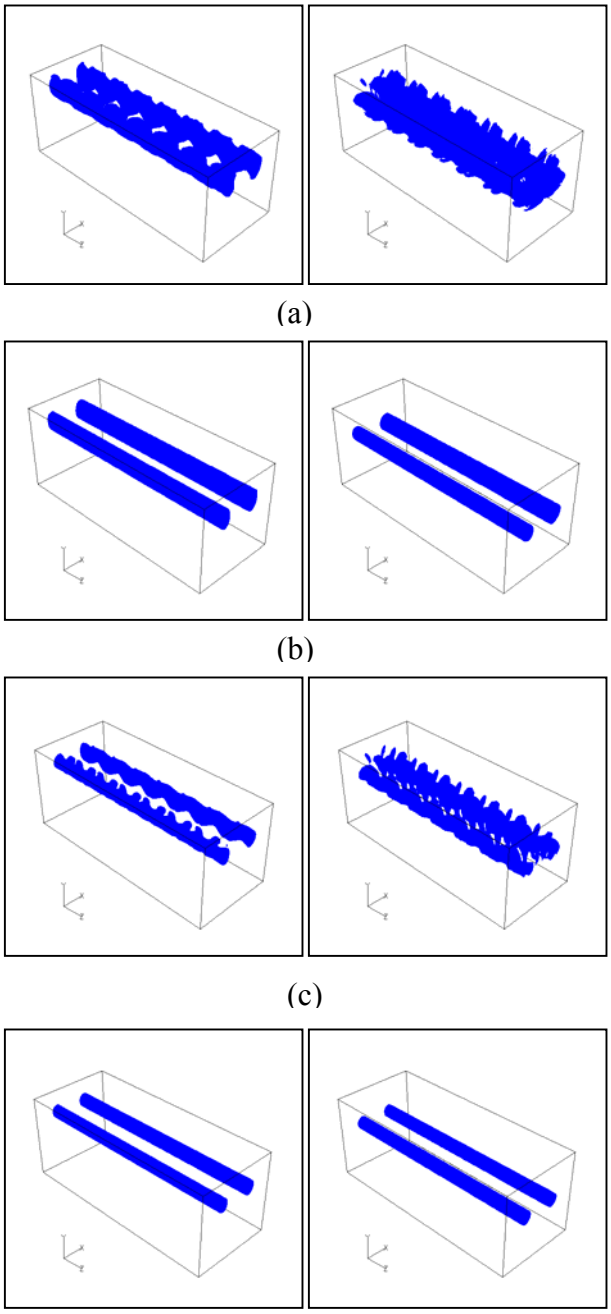

Figure 5.13 Perspective views of ISO-vorticity surface of magnitude $|\omega|R^2/\Gamma = 3$ at time $t\Gamma/b^2$ = 1.25 (left hand side), 3.75 (right hand side) for wake vortex pair: (a) elliptic core and instability; (b) elliptic core and without instability; (c) Gaussian core and instability; (d) Gaussian core and without instability

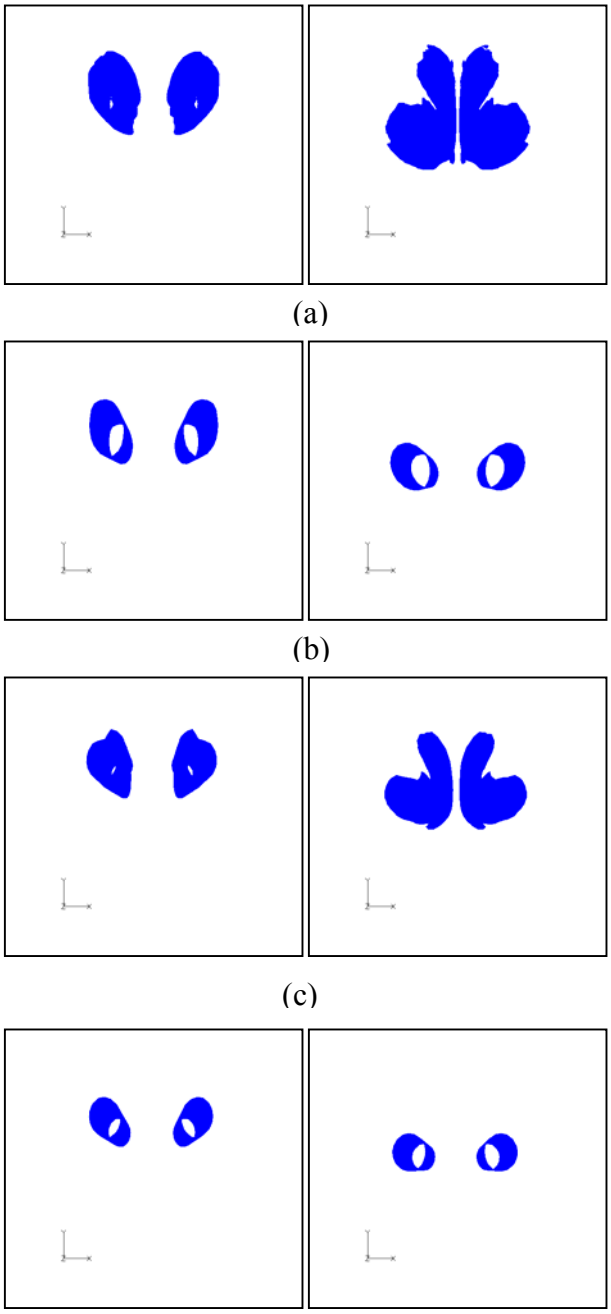

(a)

(b)

(c)

(d)

Figure 5.14 Side views of ISO-vorticity surface of magnitude $|\omega|R^2/\Gamma = 3$ at time $t\Gamma/b^2$ = 1.25 (left hand side), 3.75 (right hand side) for wake vortex pair. (a) elliptic core with instability; (b) elliptic core without instability; (c) Gaussian core with instability; (d) Gaussian core without instability

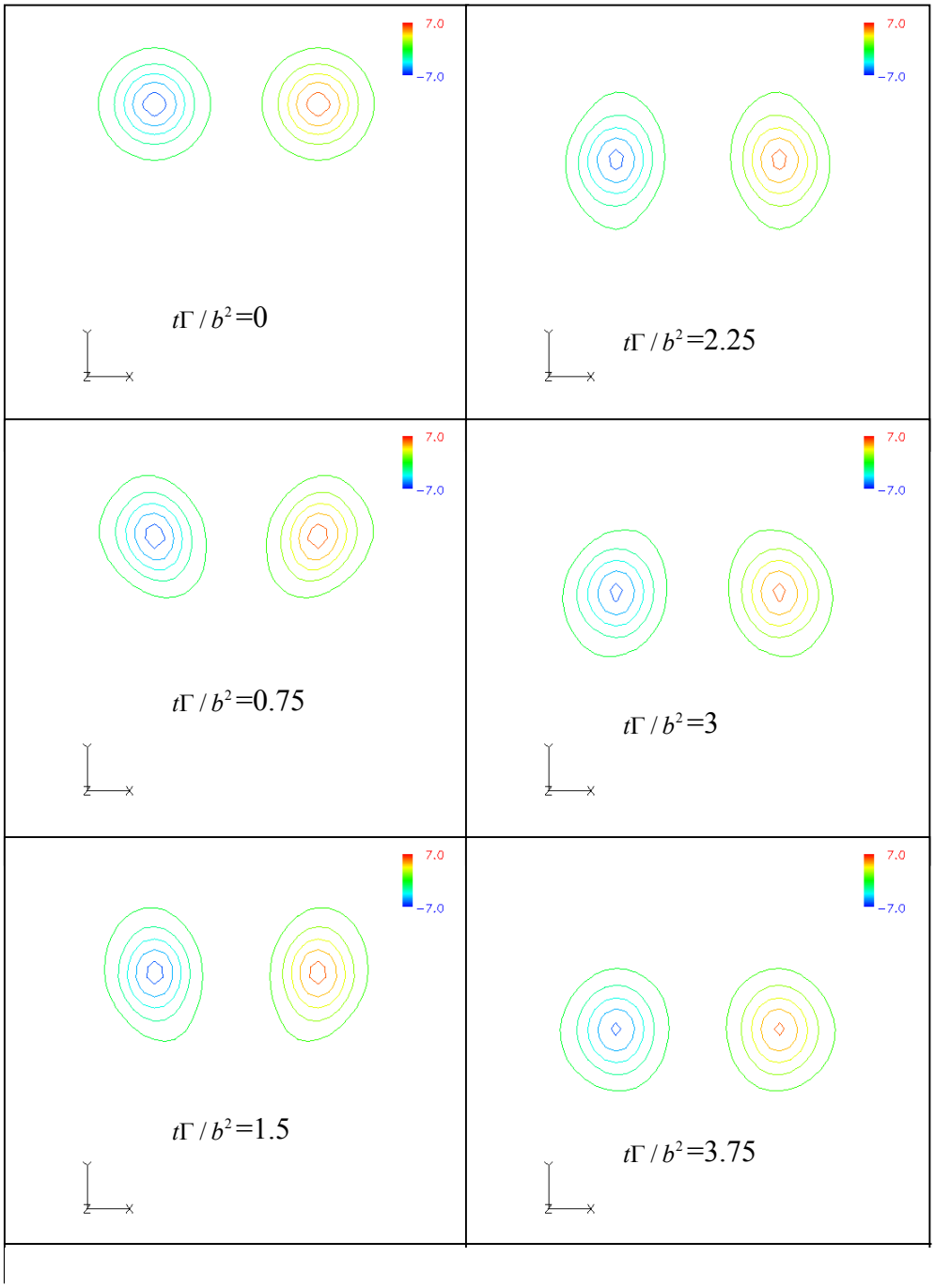

Figure 5.15 Contours of ω_z in the z = 0 symmetry plane at time $t\Gamma / b^2$ = 0, 0.75, 1.5, 2.25, 3 and 3.75 for unperturbed wake vortex pair with Gaussian distributed core (SGS = 2.5e6)

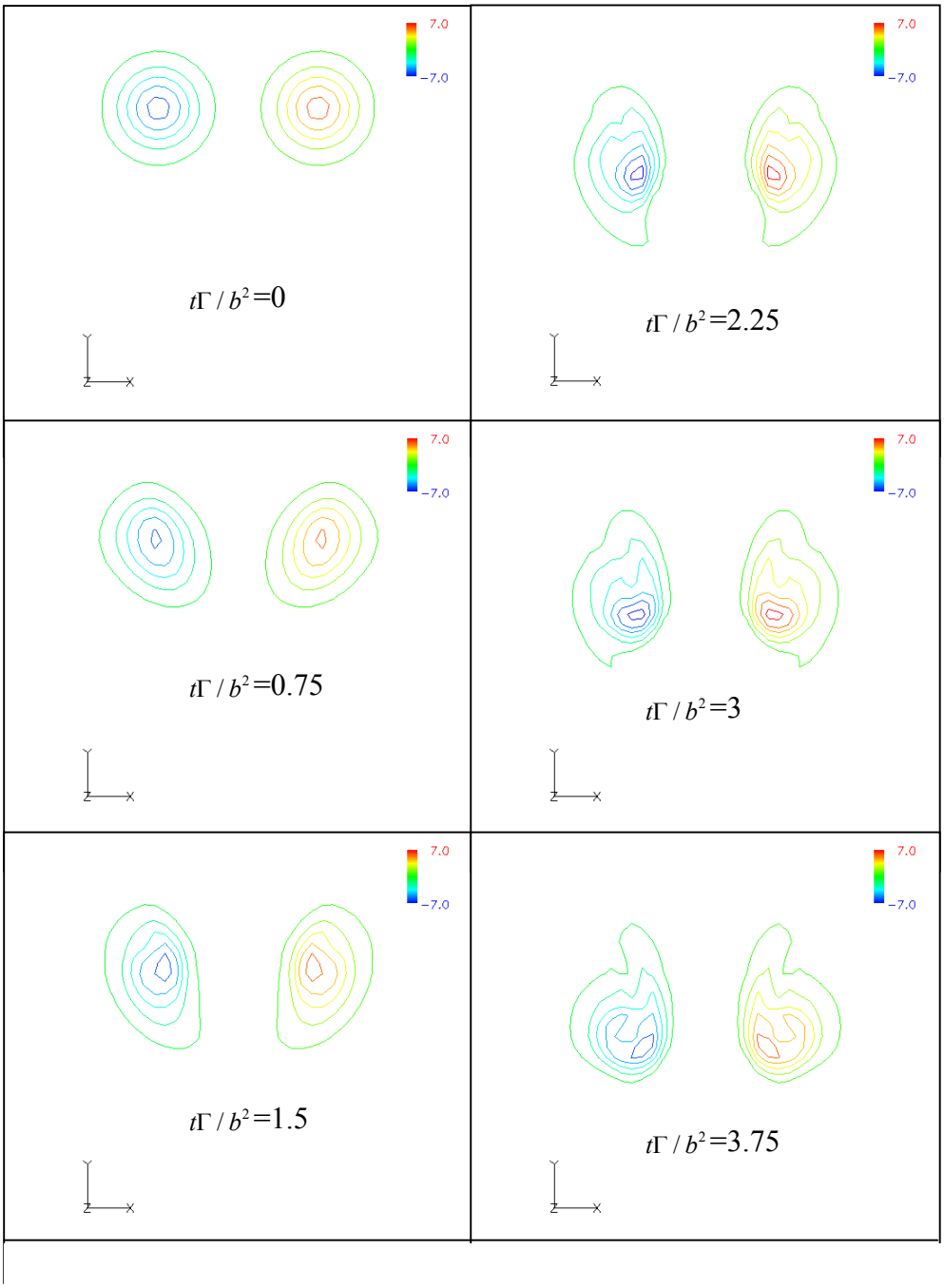

Figure 5.16 Contours of ω_z in the $z = 0$ symmetry plane at time $t\Gamma / b^2$ = 0, 0.75, 1.5, 2.25, 3 and 3.75 for wake vortex pair with Gaussian distributed core under short-wave instability (SGS = 2.5e6, n = 7)

5.6 Behavior and Acoustics of a Counter-rotating Vortex Pair under Long-wave Instability

In this section, the acoustics of a counter-rotating vortex pair under long-wave instability are investigated. Because the results of acoustics caused by the initial conditions of the Gaussian core and the results of acoustics caused by an elliptic core is explored in the wake vortex system under short-wave instability are different and the difference is explored in the preceding section, the section will mainly examine the acoustics caused by long-wave instability with an initially Gaussian distribution core.

The wake vortex pair is configured with the same initial conditions as those under short-wave instability: $a/b_o = 0.25$, $b_o = 1$, $\Delta x = 0.0628$, $\Delta t = 0.05$, $\Gamma = 1$ and the disturbance amplitude $A = 0.05$. The only difference in the current initial condition from the preceding section (short-wave instability) here is the wave number $n = 0.75$, which corresponds to a long-wave instability (wavelength is 8.38). For the setting of $na = 0.1875$, one can find it corresponds to a first zero of the rotating frequency in Figure 5.1. An initial configuration of the vortex tubes is shown in Figure 5.17.

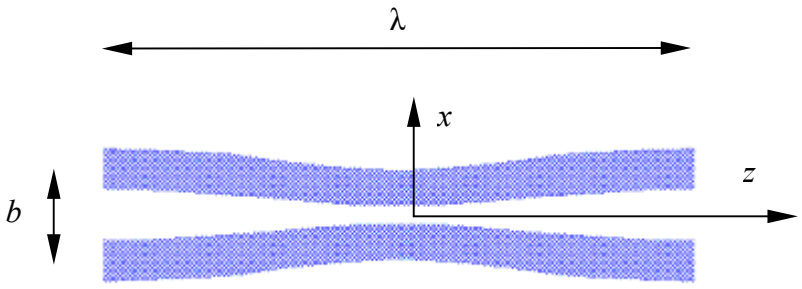

Figure 5.17 Diagram showing initial configuration of the vortex pair, with wavelength λ, nominal separation distance *b*, and the circulation Γ and –Γ.

These computations are intended to describe the evolution of two nominally anti-parallel vortices subjected to periodic perturbations in the axial direction.

Vortex tubes with arbitrary initial orientation tend to become reoriented in an anti-parallel manner as they approach each other, owing to their self- and mutually-induced velocity fields. Vortices are driven together by their mutual instability.

The vorticity contours within the core become increasingly deformed as the vorticies move toward each other, developing into the head-trail structure. This stage is characterized by active cross-diffusion, which by necessity is accompanied by bridging between the two vortex structures as a consequence of the requirement that the strength of a vortex tube remains constant (Marshall et al. 2001). The behaviors are also illustrated in Figure 5.18, Figure 5.19, Figure 5.20, and Figure 5.21.

To explain the cooperative development of the instability and corresponding acoustics, one has to consider the effect of the perturbations of each vortex on the strain it induces on the other vortex, and their mutual interaction.

Figure 5.22 and Figure 5.23 illustrate the far-field pressure within time history for the wake vortex pair with SGS = 2.5e6 and Re = 1500, respectively. When the figures are compared, it is evident that within t = 20, three stages appear for the invisicd case as I – temporary, II – approaching, and III – merging, while only two stages occurs during the time history for the viscous case as I – temporary and II – approaching. However, it should be noted here that when the invicid vortices start into the stage III, the simulation becomes numerically unstable and the result of far-field pressure is not reliable. This can be seen from the largely increasing of pressure in Figure 5.22 and the increasing of kinetic energy in Figure 5.24. However, by comparing the results of far-field pressure between two different time step sizes such as dt = 0.05 and dt = 0.025

in Figure 5.22, one can be sure that the time history of the stage II is reliable for acoustic analysis.

In Figure 5.25, showing far-field pressure with frequency domain, two peak frequencies appear for the perturbed wake vortex pair under long-wave instability, which is the same as the result for the wake vortex pair under short-wave instability. The lower peak frequency is related to the self-induced rotation and the elliptic-like shape deformed by the mutual interaction. The frequency is consistent, with the frequency without instability initially. The higher peak frequency is the result caused by the instability, which results in significant flow structure changes.

As the vorticity contour within the core is deformed seriously due to the viscous effect (Re = 1500), the corresponding frequency should be smaller than the result under inviscid effects (SGS = 2.5e6). This is proved in Figure 5.25. As the vortices move forward with each other, the vorticity contour within the core becomes increasingly deformed (see Figure 5.20 and Figure 5.21). The vortices with Re = 1500 is much more deformed than those with SGS = 2.5e6. This can be easily understood because the effect of viscosity, which smoothes the vorticity distribution and makes the core size increase in time, may significantly change this flow picture (see Figure 5.20 and Figure 5.21). Viscosity will not only reduce the perturbation growth rate, but also increase the base flow vortex radius (Sipp and Jacquin 2003). Therefore, the two kinds of peak frequency under the viscous case of Re = 1500 are smaller than those under the inviscid case of SGS = 2.5e-6, respectively.

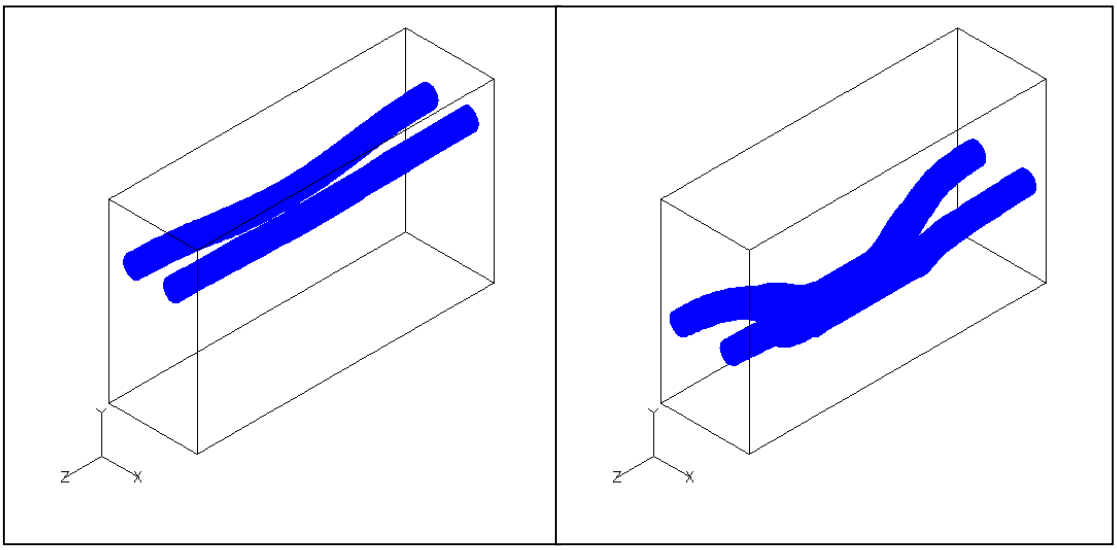

Figure 5.18 Perspective views of ISO-vorticity surface of magnitude $|\omega|R^2/\Gamma = 1.5$ at time $t\Gamma/b^2$ = 6 (left hand side), 17 (right hand side) for wake vortex pair (SGS = 2.5e-6)

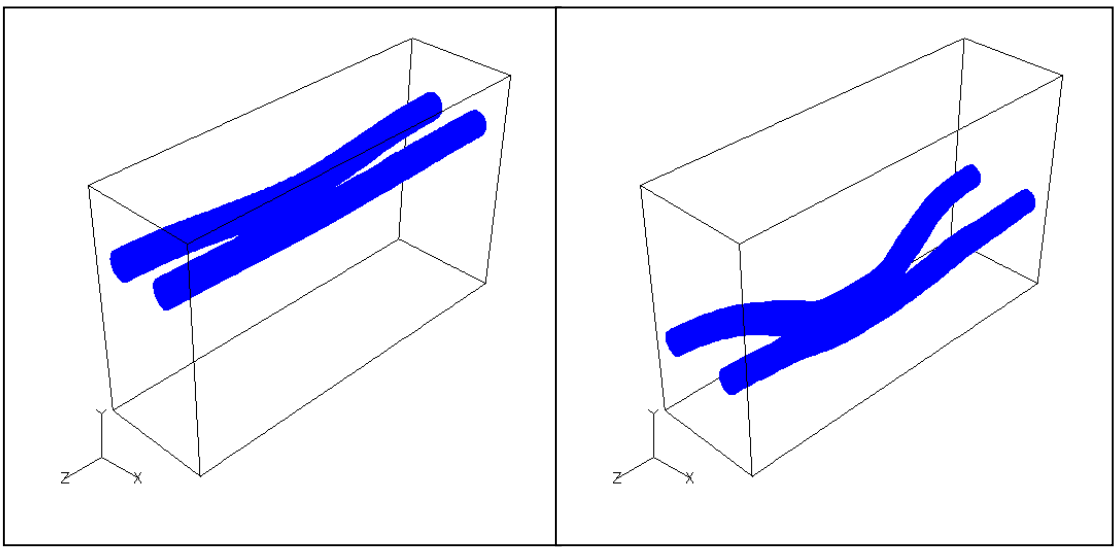

Figure 5.19 Perspective views of ISO-vorticity surface of magnitude $|\omega|R^2/\Gamma = 1.5$ at time $t\Gamma/b^2$ = 6 (left hand side), 20 (right hand side) for wake vortex pair (Re = 1500)

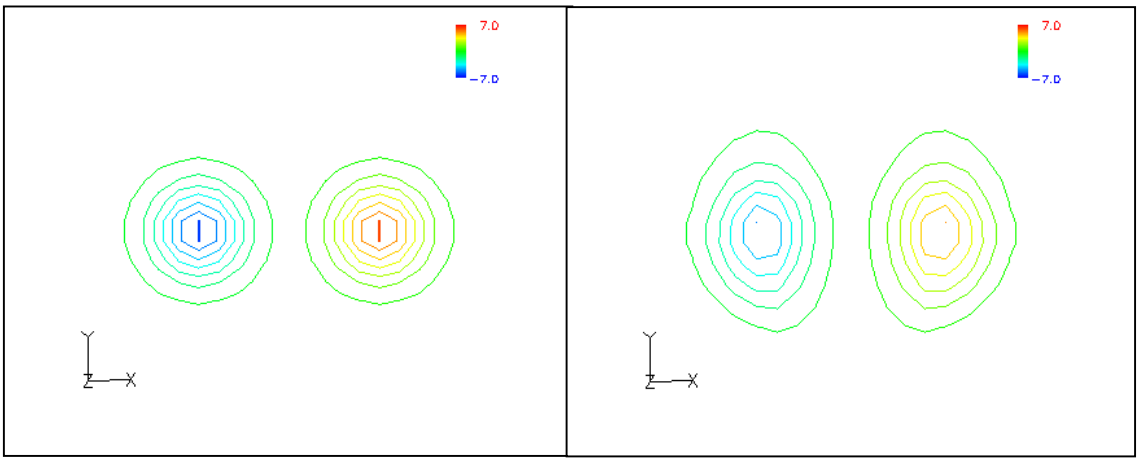

$t\Gamma / b^2 = 0$ $t\Gamma / b^2 = 6$

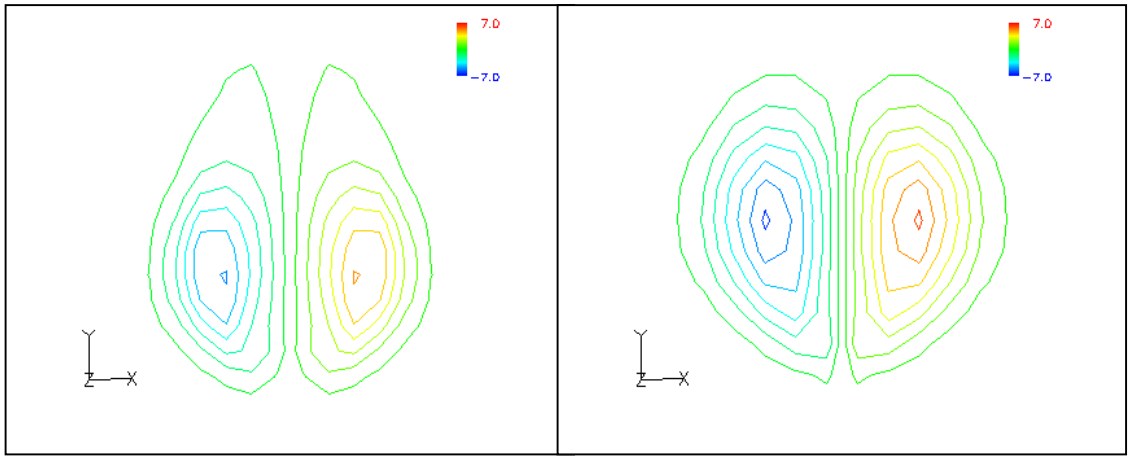

$t\Gamma / b^2 = 17$ $t\Gamma / b^2 = 20$

Figure 5.20 Contours of ω_z in the z = 0 symmetry plane at time $t\Gamma / b^2$ = 0, 6, 17 and 20 for wake vortex pair (SGS = 2.5e6)

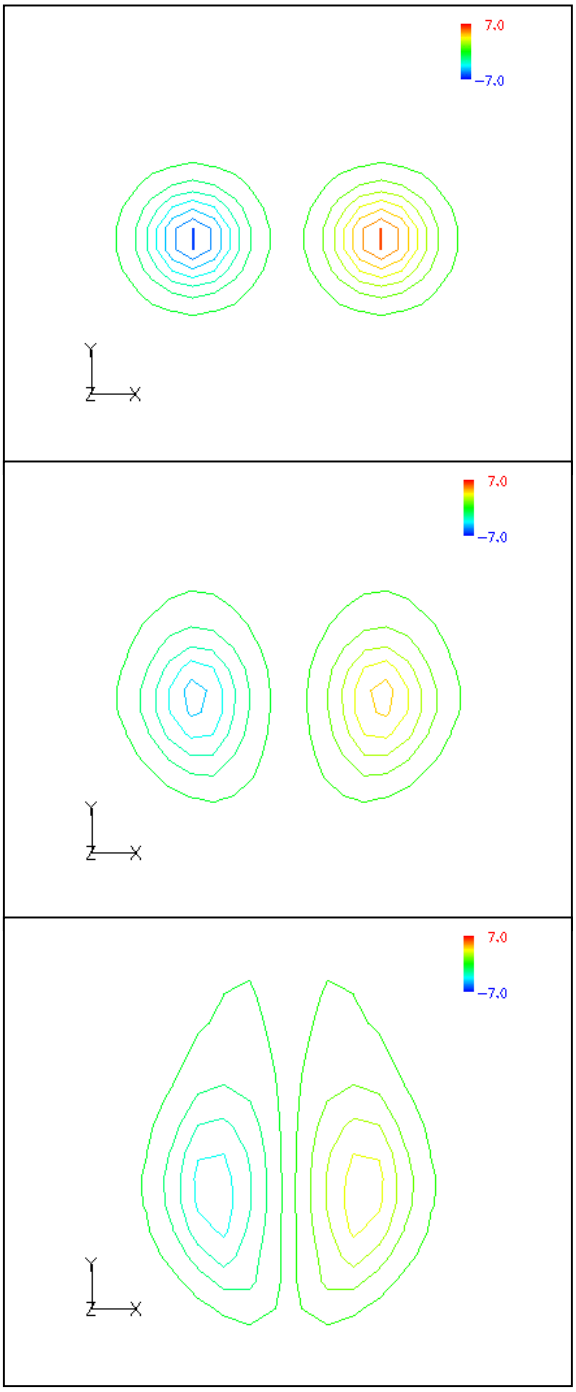

Figure 5.21 Contours of ω_z in the z = 0 symmetry plane at time $t\Gamma / b^2$ = 0, 6 and 20 for wake vortex pair (Re = 1500)

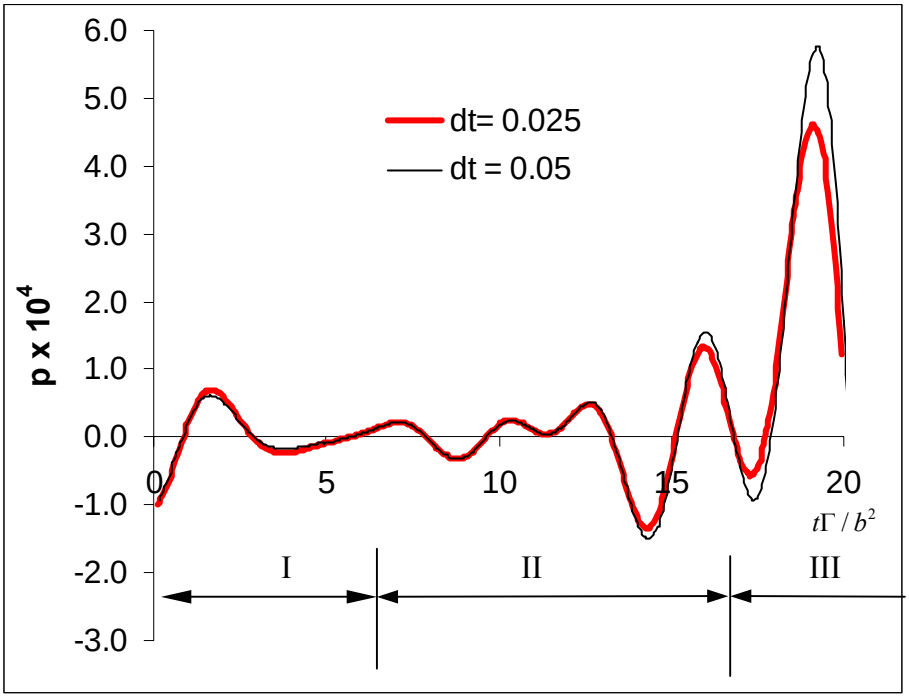

Figure 5.22 Far-field pressure within time-domain for wake vortex pair (Gaussian core) with long wavelength instability: SGS = 2.5e6

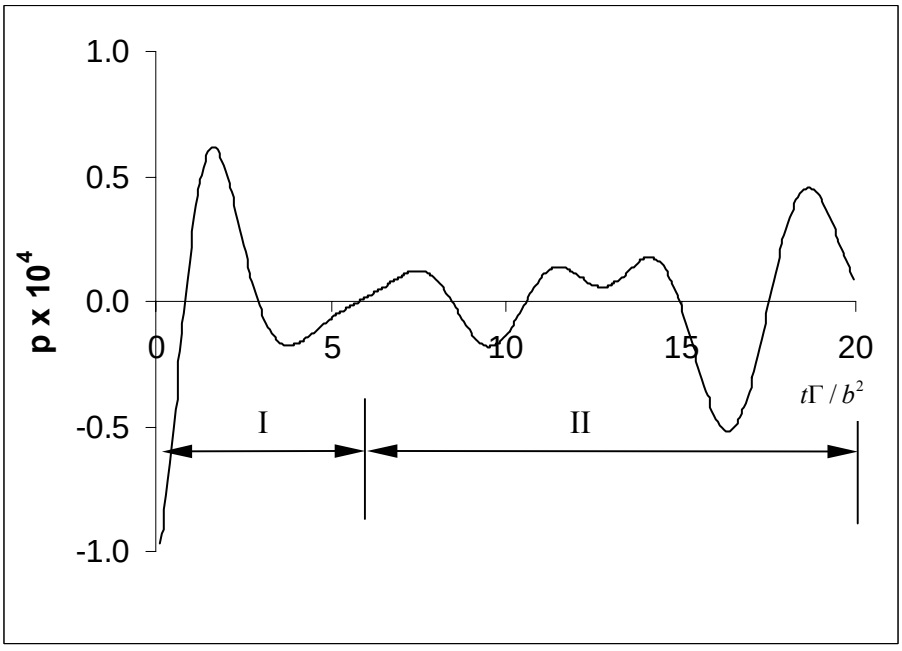

Figure 5.23 Far-field pressure in the time domain for wake vortex pair (Gaussian core) with long wavelength instability: Re = 1500

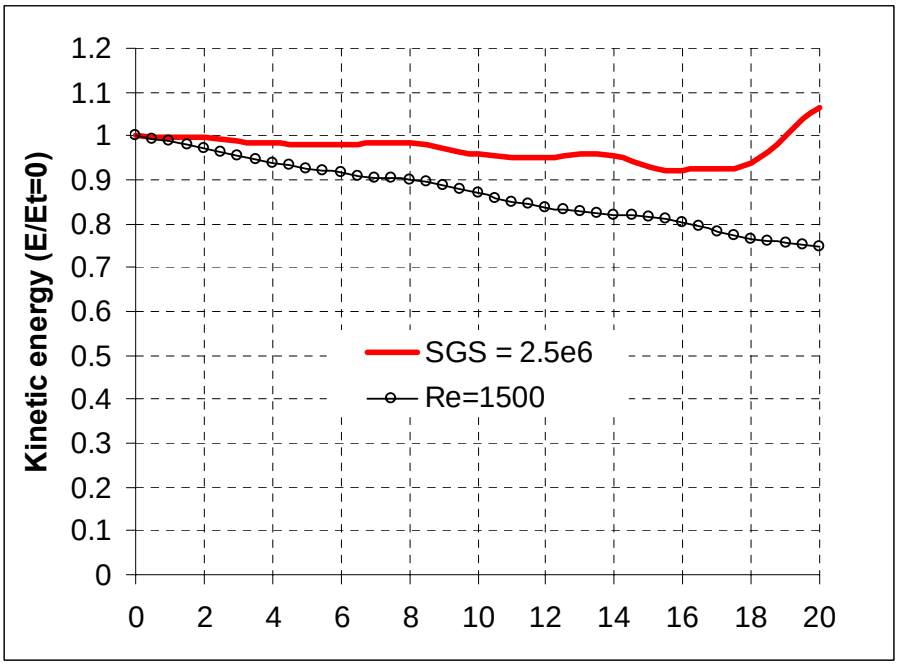

Figure 5.24 Kinetic energy ($E/E_{t=0}$) of a perturbed vortex pair (Gaussian core) under long wavelength instability.

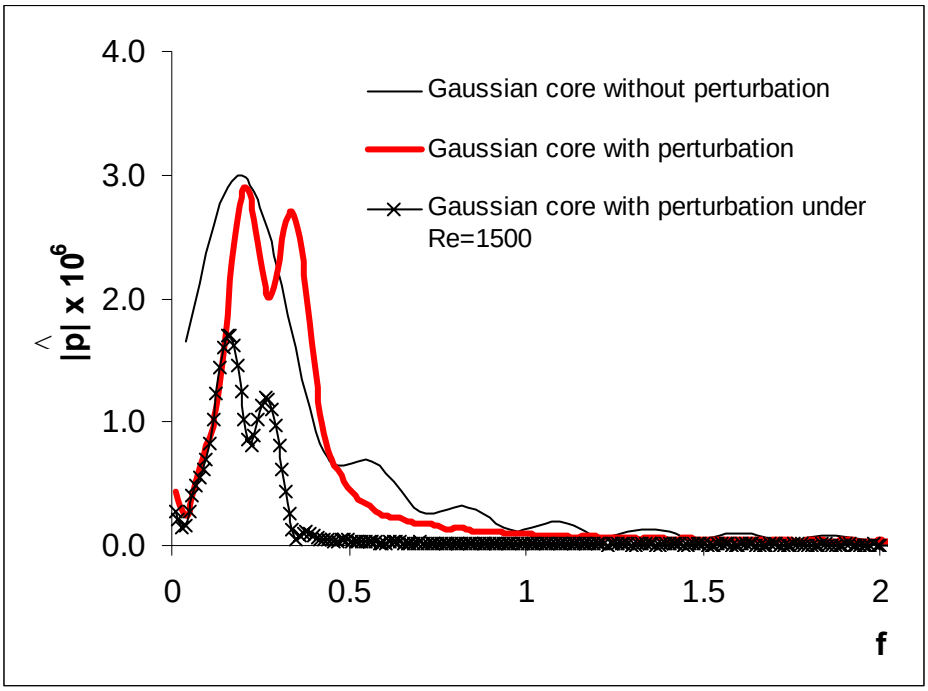

Figure 5.25 Far-field pressure in the frequency domain for wake vortex pair (Gaussian core) under long wavelength instability.

5.7 Summary and Discussion

A vortex particle method with the SGS model has been developed to compute the three-dimensional flow field related to a counter-rotating vortex pair under sinusoidal-wave instability conditions. Two kinds of instabilities, short wave and long wave, are analyzed in this chapter. They have the same core size of $a = 0.25$, the same circulation of $\Gamma = 1$ and the same amplitude of instability with $A = 0.05$ for the initial conditions. The difference is that the wave number for short wave instability is $n = 7$ and for long wave instability it is $n = 0.75$. It is apparent that the so-called cooperative instability (short wave), which has a length scale comparable to the vortex core size, has a growth rate that can exceed that of the Crow instability (long wave) (see Figure 5.7 and Figure 5.22). The conclusion is also supported by a number of theoretical studies (Widnall et al. 1974, Landman and Saffman 1987).

The far-field acoustic pressure of a three-dimensional wake vortex pair shows that a dominant frequency is related to the frequency of the elliptic vortex core rotation when the wake vortex pair is not under instability. The unstable structure can cause a higher peak frequency to appear while the frequency related to elliptic vortex core rotation still exists in the phenomena.

A peak frequency is produced by a three-dimensional counter-rotating vortex pair (about 0.2 in Figure 5.25) as the initially round Gaussian vortex cores are deformed to become an elliptic-like shape quickly due to the stretching effect and mutual interaction. If the initial core distribution is elliptic, the peak frequency becomes greater, approximating the value of the Kirchhoff frequency (0.37 in Figure 5.25).

A higher peak frequency appears due to the straining field caused by mutual perturbation. The corresponding flow structure caused by the mutual perturbation should be different from the existing self-induced rotation. Whether for long-wave instability or for short-wave instability, the

higher peak frequency is greater than the analytical Kirchhoff frequency, which is approximately 0.5. If the initial vorticity distribution in the vortex cores is elliptic, coupled with the instability, the produced higher peak frequency is more than 0.5.

The effect of viscosity, which smoothes the vorticicity distribution and makes the core size bigger, has an important influence on the peak frequency and corresponding pressure magnitude. Actually, the peak frequency and the pressure magnitude are reduced further with the effect of viscosity.

6 Conclusion and Future Work

Acoustic sound produced by an aircraft wake vortices has been investigated using a vortex particle method and a vortex sound formula in the far field. The mechanisms of sound production have been identified.

In a two-dimensional vortex system, the stretching effect in the axial direction is neglected. The purpose of this study is to focus on the behaviors of a vortex core. The following conclusions can be made for the two-dimensional vortex system based on our results:

(1) The simulation results of a counter-rotating vortex pair confirm that the peak frequency of the wake sound emission is essentially the same as the classical Kirchhoff vortex, even under the influences of an inviscid ground effect or a weak-shear cross wind. These results suggest that the identified mechanism should be fairly robust which demonstrates its persistency under several different environmental conditions.

(2) In a system with multiple vortices, there are identifiable frequencies when no merging occurs, each of which can be attributed to either the vorticity in the vortex cores or to the motion of the center of the vortices. When two identical vortices approach each other, the low frequency related to the rotation motion of the vortex center becomes higher, and the high frequency related to the core self-rotation tends to decrease although not significantly. After vortex merging, there is only one frequency resulting from the merged core rotation. In a multiple vortex pair system such as those in aircraft wakes, the above-described behaviors do not seem to change in spite of the induction from the mirror image of the vortices.

In three-dimensional vortices, sinusoidal instabilities, which occur in the axial direction at various length scales, result in significant flow structure changes in these vortices, and thus influence their radiated acoustic signals. Numerical simulations of a perturbed vortex ring and a pair of counter-rotating wake vortices undergoing both long-wave and short-wave instabilities show the following:

(1) A steady vortex ring with a Gaussian core does not radiate any sound. When a perturbation is imposed at the azimuthual direction of the vortex ring, two distinct peak frequencies appear for both the stable mode and unstable mode. The higher-frequency peak is related to the forced perturbation. The lower-frequency peak is related to the deformation of the vortex core. As we know, an unperturbed vortex ring with an elliptic core is able to radiate sound. The vortex core of the perturbed vortex ring is mostly deformed into an elliptic-like core due to the perturbation around the azimuthal direction. A stable perturbed vortex ring tends to radiate stronger sound than an unstable one at the higher frequency peak.

(2) A dominant frequency is related to the Kirchhoff frequency of the elliptic vortex core rotation when the wake vortex pair is not perturbed. A peak frequency is produced by three-dimensional wake vortices when the initially round Gaussian vortex cores are quickly deformed to an elliptic-like shape due to stretching effects and mutual interaction.

(3) A higher peak frequency than the original Kirchhoff frequency appears due to the straining field caused by mutual perturbation, under both long-wave and short-wave instabilities, while the Kirchhoff frequency related to the elliptic vortex core rotation still exists. The corresponding flow structure induced by the mutual perturbation becomes different from the existing self-induced rotation.

(4) The effect of viscosity, which smoothes the vorticity distribution and makes the core size bigger, has an important influence on the peak frequency and corresponding pressure magnitude. Actually, the peak frequency and the pressure magnitude are reduced further with the effect of viscosity.

(5) In the numerical simulations of a three-dimensional vortex ring and the vortex pair, two distinct peak frequencies are found under perturbations. The mechanism of generation of the lower peak frequency, which is related to the core deformation, is consistent with that in the two-dimensional wake vortices. When a perturbation is imposed at the axial direction in the three-dimensional flow, a higher peak frequency occurs due to mutual perturbation, which cannot be simulated in two-dimensional calculations.

In future work, an efficient computation such as fast multiple methods while maintaining the accuracy to capture acoustic fluctuations is very necessary. Our current numerical simulation is based on the bigger core size (a/b=0.25) while the realistic core size a of aircraft wake vortex is at the range of 1.5% and 2% of wing span b. The numerical simulation with a smaller core size requires expensive computations. Our current MPI scheme cannot quite accommodate the expensive computations.

In addition, future work should also explore the multiple wake vortices under both long-wave and short-wave instabilities. Airplanes with flaps deployed produce multiple vortices in the near field, which can result in a pair of co-rotating vortices on each side of the aircraft farther downstream. The recent studies have exploited the instabilities and transient growth mechanisms that exist for systems of vortices with multiple vortex pairs (Crouch 1997, Fabre et al. 2003). These mechanisms lead to a more rapid growth than that occurs on a single vortex pair. As we have mentioned in the numerical simulation of a counter-rotating pair, the instability can cause

the peak frequency shift to a higher value. In a multiple vortex system, the more rapid growth can possibly generate a higher peak frequency than the one we currently calculated. Furthermore, in a multiple vortex system, two co-rotating pairs tend to merge and form a new counter-rotating pair, which also has an effect on the mechanisms of sound production. During the merging, numerically instability in our current schemes also becomes a major challenge for the future work. This will urge us to explore a more efficient numerical scheme to capture the perturbations while maintaining the numerical stability.

References

Alix, D.C., Simich, P.D., Wassaf, H. and Wang, F.Y., "Acoustic characterization of wake vortices in ground effect," AIAA paper 2005-0260, Jan. 2005.

Ashurst W.T., Meiburg, E., Three-dimensional shear layers via vortex dynamics. Journal of fluid mechanics 1988, vol. 189, pp. 87-116.

Beale, J.T. and Majda, A., "Vortex methods. I: convergence in three dimensions". Mathematics of computation 39, 159(1982).

Bohning, P., Baumann, R., Michel, U. and Gerz, T., Numerical study of wake vortex noise using LES and an acoustic analogy method, Euromech colloquium 467: turbulent flow noise generation, Marseille, France, July 2005.

Booth, E.R., Jr., and Humphreys, W.M., Jr., "Tracking and characterization of aircraft wakes using acoustic and lidar measurements," AIAA paper 2005-2964, May 2005.

Cottet, G.H. and Koumoutsakos, P., "Vortex Methods: Theory and Practice". Cambridge University Press, 2000.

Crouch, J.D. Instability and transient growth for two trailing-vortex pairs. J. Fluid Mech. (1997), vol 350, pp. 311-330.

Crow, S.C. Stability theory for a pair of trailing vortices. AIAA Journal (8) 1970, pp2172-2179.

Donaldson, C. Dup., and Bilanin, A.J., Vortex wakes of conventional aircraft. AGARDograph 204, May 1975.

Dougherty, R. P., Wang, F. Y., Booth, E. R., Watts, M. E., Fenichel, N. and D'Errico, R. E., Aircraft wake vortex measurements at Denver International Airport. 10th AIAA/CEAS Aeroacoustics Conference, AIAA Paper No. 2004-2880, Manchester, UK, May 2004.

Eldredge, J.D., Colonius, T., and Leonard, A., A vortex particle method for two-dimensional compressible flow. J. C.P (2002) 179, pp. 371-399.

Eldredge, J.D., Leonard, A. and Colonius, T., A general deterministic treatment of derivatives in particle methods. J. C.P (2002) 180, pp. 686-709.

Fabre, D., Jacquin, L. and Loof, A., Optimal perturbations in a four-vortex aircraft wake in counter-rotating confirguration. J.Fluid Mech. (2002), vol. 451, pp. 319-328.

Fischer, D., A new vortex scheme for viscous flows. J. Comput. Phys. (1990) V86, pp. 211-224.

Garten, J.F., Werne, J., Fritis, D.C. and Arendt, S., Direct numerical simulations of the Crow instability and subsequent vortex reconnection in a stratified fluid. J.Fluid Mech. (2001), Vol. 426, pp. 1-45.

Gerz, T., Holzapfel, F. and Darracq, D., Commercial aircraft wake vortices. Progress in Aerospace Sciences 38 (2002) 181-208.

Gharakhani, A., Application of the vorticity redistribution method to LES of incompressible flow. J. of turbulence 2003 February.

Greene, G.C., Earl, D.R., Burnham, D.C., Hallock, J.N. and Rossow, V.J., Wake vortex research lessons learned. Proceeding of the aircraft wake vortices conference, Vol. 1, U.S. Dept. of Transportation, Washington, DC, 1991.

Greengard, L. and Rokhlin, V., A fast algorithm for particle simulations. J. Comput. Phys. 73(2), 325 (1987).

Gropp, W. Lusk, E. and Skjellum, A., Using MPI: portable parallel programming with the message-passing interface. The MIT Press Cambridge, 1999.

Han, J., Lin, Y., Arya, S.P. and Proctor, F.H., " Numerical study of wake vortex decay and descent in homogeneous atmospheric turbulence, " AIAA Journal, Vol. 38, No.4, 2000, pp. 643-656

Han, J., Lin, Y.L., Schowalter, D., Arya, S. and Proctor, F., Large eddy simulation of aircraft wake vortices within homogeneous turbulence: Crow instability. J. Aircraft (200) 38, 292-300.

Hardin, J.C. and Wang, F.Y., Sound generation by aircraft wake vortices. NACA/CR-2003-212674, December 2003.

Hongyu, Ran. Numerical study of the dynamics and sound generation of a turbulent vortex ring. 2004 Caltec Thesis.

Hongyu, Ran and Colonius, T., Numerical simulation of sound radiated from a turbulent vortex ring. 10th AIAA/CEAS Aeroacoustics Conference, AIAA 2004-2918..

Howe, M.S., Theory of vortex sound, Cambridge university press, Cambridge, U.K., 2003.

Izaguirre, J.A., Hampton, S.S., and Matthey, T., Parallel Multigrid Summation for the N-body Problem. Journal of Parallel and Distributed Computing, Vol. 65, pp. 949-962, 2005.

Jacquin, L., On trailing vortices: A short review. International Journal of Heat and Fluid Flow 26 (2005) 843-854.

Kao, H.C., Body – vortex interaction, sound generation, and destructive interference. AIAA Journal, Vol. 40, No. 4, 2002, pp. 652-660.

Knio, O.M., Ghoniem, A.F., Numerical study of a three-dimensional vortex method. J. Comput. Phys. 86, 75-106 (1990).

Landman, M.J. and Saffman, P.G., The three-dimensional instability of strained vortices in a viscous fluid. Phys. Fluids. 30, 2339-2342.

Lamb, H., Hydrodynamics, Cambridge University Press, Cambridge, U. K., 7th ed., 1975.

Leonard, A., Vortex methods for flow simulation. J.C.P. 37(3), 289(1980).

Leung, R.C.K, and N.W.M.Ko, On sound radiated from a perturbed vortex ring. Acta Mechanica 146, 43-58 (2001).

Leweke, T. and Williamson, C.H.K., Cooperative elliptic instability of a vortex pair. J. Fluid Mech. (1998), vol. 360, pp. 85-119.

Lighthill, M.J., On sound generated aerodynamically I. General theory. Pro. R. Soc. Lond. A 211, 1952, pp. 564-587.

Lu, J.L., and Okunbor, D., *A Massively Parallel Fast Multipole Algorithm in Three Dimensions,* in the Proceedings of Fifth IEEE International Symposium on High Performance and Distributed Computing, pp. 40-48, August 1996. [EI]

Mitchell, B.E., Lele, S., and Moin, P., Direct computation of the sound from a compressible co-rotating vortex pair. Journal of Fluid Mechanics, Vol. 285, 1995, pp.181-202.

Mitchhell, U. and Bohning, P., Investigation of aircraft wake vortices with phased microphone arrays. 8th AIAA / CEAS Aeroacoustics Conference, AIAA paper No. 2002-2501, Breckenridge, CO, June 2002.

Mohring, W., On vortex sound at low Mach number. Journal of Fluid Mechanics, Vol. 85, 1978, pp. 685-691.

Nomura, K.K., Tsutusi, H., Mahoney, D. and Rottman, J.W., Short-wavelength instability and decay of a vortex pair in a stratified fluid.

Marshall, J.S., Brancher, P. and Giovannini, A., Interaction of unequal anti-parallel vortex tubes. J. Fluid Mech. (2001), vol. 446, pp. 229-252.

Moore, D.W. and Saffman, P.G., The instability of a straight vortex filament in a strain field. Proc. R. Soc. London Ser. (1975) A 346, pp. 413-425.

Muller, B. and Yee, H.C., High order numerical simulation of sound generated by the Kirchhoff vortex, Computing and visualization in science, vol. 4, 2002, pp. 197-204.

Orlandi, P., Carnevale, G.F., Lele, S.K. and Shariff, K., DNS study of stability of trailing vortices. In Proceedings of the Summer Program 1998, Center for Turbulence Research, pp. 187-208.

Ortega, J.M., Bristol, R.L. and Savas, O., Experimental study of the instability of unequal-strength counter-rotating vortex pairs. J. Fluid Mech. (2003), vol. 474, pp. 35-84.

Pozrikidis, C., Fluid dynamics: theory, computation, and numerical simulation. Kluwer academic publishers, 2001.

Qiao, W., and Michel, U., "A study on the vortex shedding noise from the wake of aircraft wings." AIAA paper 2000-1973, June 2000.

Ploumhans, P., Winckelmans, G.S., Salmon, J.K., Leonard, A. and Warren, M.S., Vortex methods for direct numerical simulation of three-dimensional bluff body flows: application to the sphere at Re=300, 500 and 1000. J.C.P 178 (2002), pp. 427-463

Rubin, W.L., " The generation and detection of sound emitted by aircraft wake vortices in ground effect," Journal of Atmospheric and Oceanic Technology, Vol. 22, May 2005, pp. 543-554.

Rogers, M.M. and Moser, R.D., The three-dimensional evolution of a plane mixing layer: the Kelvin-Helmholtz rollup, Journal of Fluid Mechanics, vol. 243, 1992, pp. 183-226.

Saffman, P.G., Vortex dynamics, Cambridge Univ. Press, Cambridge, England, 1995.

Salmon, J.K., Warren, M., Skeletons from the treecode closet. J. Comput. Phys. 111 (1994) 136-155.

Salmon, J.K., Warren, M., Skeletons, Winckelmans, G., Fast parallel tree codes for gravitational and fluid dynamical N-body problems. Internat. J. Supercomput. Appl. High Performance Comput. 8(2)(1994) 129-142.

Shariff, K., Verzicco, R. and Orlandi, P., A numerical study of the three-dimensional vortex ring instabilities: viscous corrections and early nonlinear stage. J. Fluid Mech. 279, 351-375

Scorer, R.S. and Davenport, L.J., Contrails and aircraft downwash. J. F.M (1970) 43, 451-464

Singer, J.K., Parallel implementation of the fast multipole method with periodic boundary condition. J. Numer. Math., vol.0., No.0, pp. 000-000 1995.

Sipp, D. and Jacquin, L., Widnall instabilities in vortex pairs. Phys. Fluids (2003) 15, 1861-1874.

Spalart, P.R., Airplane trailing vortices. Annu. Rev. Fluid Mech. 1998.30: 107-38.

Spalart P.R., Wray, A.A., Initiation of the Crow instability by atmospheric turbulence. Proceedings of Symposium on the characterization and moidification of wakes from lifting vehicles in fluids, AGARD-CP-584, 1996.

Sparpkaya, T., Daly, J.J., Eeffect of ambient turbulence on trailing vortices. Journal of Aircraft 1987, Vol. 240, pp. 399-404.

Tang, S. K., and Ko, N. W. M., Sound sources in the interactions of two inviscid two-dimensional vortex pairs. Journal of Fluid Mechanics, vol. 419, 2000, pp. 177-201.

Tang, S. K., and Ko, N. W. M., Basic sound generation mechanisms in inviscid vortex interactions at low Mach numer. Journal of Sound and Vibration, vol. 262, 2003, pp. 87-115.

Tsai, S.E., Widnall, S.E., The instability of short waves on a straight vortex filament in a weak externally imposed strain field. J. Fluid Mech., vol. 73, 1976, pp. 721-733.

Wang, F.Y., Wassaf, H.S., Gulsrud, A., Delisi, D.P. and Rudis, R.P., Acoustic imaging of aircraft wake vortex dynamics. AIAA Paper No. 2005-4849, Toronto, Canada, June 2005.

Wee, D. and Ghoniem, A.F., Modified interpolation kernels for treating diffusion and remeshing in vortex methods. J.C.P 213 (2006) 239-263.

Widnall, S. E., Bliss, D. and Tsai, C. The instability of short waves on a vortex ring. J. Fluid Mech. 66(1974), 35-47

Widnall, S.E. and Sullivan, J.P., On the stability of vortex rings. Proc. Roy. Soc. Lond. A332, 335-353 (1973).

Widnall, S., and Tsai, C. The instability of the thin vortex rings of constant vorticity. Phil. Trans. R. Soc. London A 287 (1977), 273-305.

Winckelmans, G.S., Vortex methods, in: E. Stein, R. de Borst, Th.J.R. Hughes (Eds.), The Encyclopedia of Computational Mechanics, vol.3, John Wiley and Sons, Oct. 2004.

Winckelmans, G., Leonard, A., Contributions to vortex particle methods for the computation of three-dimensional incompressible unsteady flows, J.Comput.Phys. 109(2)(1993) 247-273.

Winckelmans, G., Cocle, R., etc. “Vortex methods and their application to trailing wake vortex simulations”. Comptes Rendus Physique, Vol. 6, No. 4-5, 2005, pp. 467-486.

Zheng, Z.C., Thin-tube vortex simulations for sinusoidal instability in a counter-rotating vortex pair. International journal for numerical methods in fluids (2002), Vol. 39, pp. 301-324.

Zheng, Z.C., Far-field acoustic pressure from a system of discrete vortices with time-varying circulation. AIAA paper 2005-3005, 11th AIAA/CEAS Aeroacoustics Conference, May 23-25, 2005, Monterey, CA.

Zheng, Z.C., and Lim, S.H., "Validation and operation of a vortex wake/shear interaction model," Journal of Aircraft, Vol. 37, No. 6, 2000, pp. 1073-1078

Zheng, Z. C., Li, W., Wang, F. and Wassaf, H. F., "Influence of Vortex Core on Wake Vortex Sound Emission." Journal of Aircraft, Vol. 44, No. 4, 2007, pp. 1369-1377

Appendix A - Far-Field Sound Formula for a Discrete Vortex System

Similar to the derivation of Kao (2002), a matched-asymptotic-expansion method is used that matches the inner region of incompressible flow to the outer region of an acoustic field. The condition for the matched asymptotic expansions to exist is low Mach number. All the variables are nondimensionalized by *L, U* and ρ_o, which are respectively the vortex half-span, the nominal maximum vortex rotating speed, *U*, and the density of air. The Mach number, *M*, is defined as U/c_o where c_o is the speed of sound.

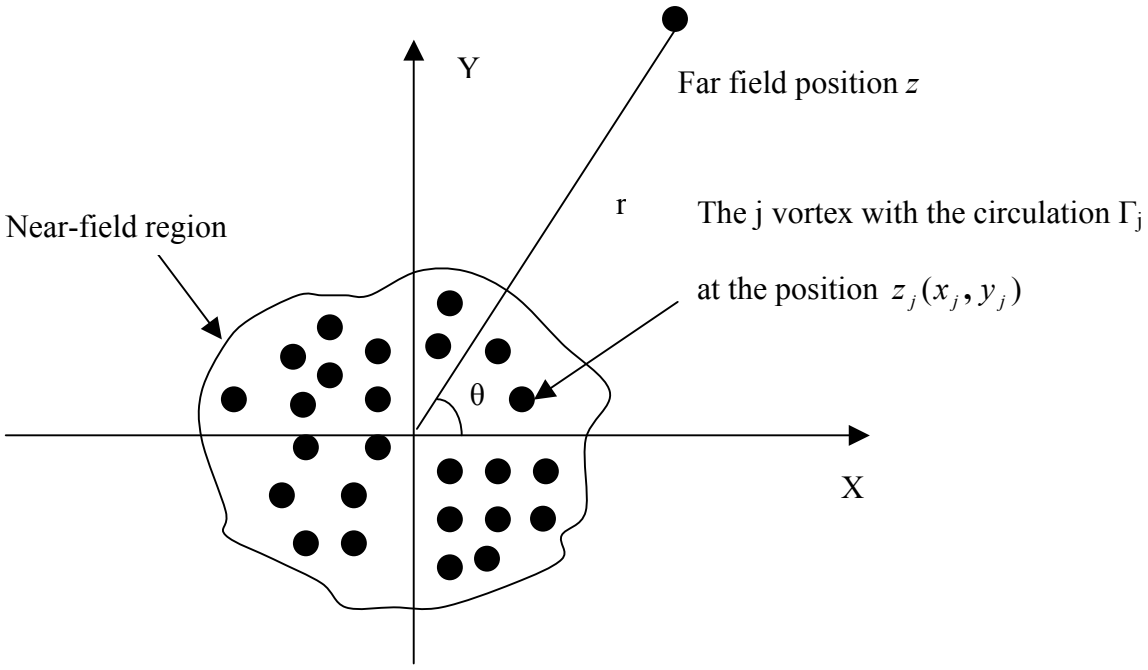

Fig. 1 Illustration of a discrete vortex system and the far field position

Since the inner region flow field is generated by a system of discrete vortices, the complex velocity potential can be expressed as

$$W = \Phi + i\Psi = \frac{i}{2\pi}\Gamma_i(t)\ln[z - z_j(t)], \tag{A1}$$

where Γ_j is the j vortex circulation at position z_j, and z is the far-field location (see the following Fig. 1 for the detail). Both Γ_j and z_j can be functions of time. The Einstein summation convention, with respect to j, is implied.

After expanding the logarithmic function (Taylor series) in Eq. A1 around z_j under the condition of $\left|z_j / z\right| << 1$, we have

$$W = \frac{i}{2\pi}\ln z\sum\Gamma_j - \frac{i}{2\pi}\Gamma_j\frac{z_j}{z} - \frac{i}{4\pi}\Gamma_j\frac{z_j^2}{z^2} + O\left[\left(\frac{z_j}{z}\right)^3\right]. \tag{A2}$$

The first term does not relate to acoustic sources, and is steady following Kelvin's theorem. Denoting the fluctuation complex velocity potential as w, we have

$$w = -\frac{i}{2\pi}\Gamma_j\frac{z_j}{z} - \frac{i}{4\pi}\Gamma_j\frac{z_j^2}{z^2}. \tag{A3}$$

By means of the Bernoulli equation in non-dimensional form, the inner pressure fluctuation is

$$\begin{aligned} p_i = -\frac{\partial\phi}{\partial t} = \frac{1}{2\pi r}\left[\frac{d(\Gamma_j x_j)}{dt}\sin\theta - \frac{d(\Gamma_j y_j)}{dt}\cos\theta\right] - \\ \frac{1}{4\pi r^2}\left\{\frac{d}{dt}\left[\Gamma_j(2xy)_j\right]\cos(2\theta) - \frac{d}{dt}\left[\Gamma_j(x_j^2 - y_j^2)\right]\sin(2\theta)\right\} \end{aligned}, \tag{A4}$$

where $r = |z|$ and $\theta = \mathrm{Arg}(z)$ are the distance and angle of the far-field receiver, respectively, and are assumed independent of time.

The pressure fluctuation at the outer region, p_o, satisfies the convective wave equation, given by

$$\frac{\partial^2 p_o}{\partial x^2} + \frac{\partial^2 p_o}{\partial y^2} - M^2\frac{D^2 p_o}{Dt^2} = 0. \tag{A5}$$

After transformation using the outer variables and letting $M \to 0$, the acoustic equation is obtained:

$$\frac{\partial^2 p_o}{\partial X^2} + \frac{\partial^2 p_o}{\partial Y^2} - \frac{\partial^2 p_o}{\partial t^2} = 0, \tag{A6}$$

where $X = Mx$ and $Y = My$. The formation of the outer solution is suggested by the inner solution to be

$$\begin{aligned} p_o = &\sum_j S_j(R,t)\sin\theta + \sum_j C_j(R,t)\cos\theta + \\ &\sum_j K_j(R,t)\cos(2\theta) + \sum_j L_j(R,t)\sin(2\theta) \end{aligned}, \tag{A7}$$

where $R = M r$, and S_j, C_j, K_j and L_j are functions to be determined. After substituting this expression into Eq. A6 and performing the Fourier transform in time, Eq. A6 can be solved to yield p_o in the frequency domain for the out-going waves, giving

$$\begin{aligned} \hat{p}_o = &\left(\sum_j A_j \sin\theta + \sum_j B_j \cos\theta\right) H_1^{(2)}(\Omega R) + \\ &\left(\sum_j E_j \cos(2\theta) + \sum_j G_j \sin(2\theta)\right) H_2^{(2)}(\Omega R) \end{aligned}, \tag{A8}$$

where $H_1^{(2)}$ is the second kind Hankel function of order one, $H_2^{(2)}$ is the second kind Hankel function of order two, Ω is the angular frequency and A_j, B_j, E_j and G_j are constants to be determined by the matching condition between the inner and outer solutions.

The matching is performed by letting $R \to 0$ in Eq. A8 and re-writing the expression in terms of the inner variables. Thus,

$$H_1^{(2)}(\Omega R \to 0) \to \frac{2i}{\pi \Omega R} = \frac{2i}{\pi \Omega M r}, \tag{A9}$$

$$H_2^{(2)}(\Omega R \to 0) \to \frac{4i}{\pi (\Omega R)^2} = \frac{4i}{\pi \Omega^2 M^2 r^2}. \tag{A10}$$

Substituting these expressions into Eq. A8 and comparing to Eq. A4 yields the outer solution as

$$\hat{p}_o(\Omega) = \frac{iM\Omega}{4} H_1^{(2)}(\Omega R) \cdot \left\{ F[\frac{d(\sum_j \Gamma_j y_j)}{dt}] \cos\theta - F[\frac{d(\sum_j \Gamma_j x_j)}{dt}] \sin\theta \right\} +$$

$$i\frac{M^2\Omega^2}{16} H_2^2(\Omega R) \left\{ F[\frac{d(\sum_j 2x_j y_j \Gamma_j)}{dt}] \cos(2\theta) - F[\frac{d(\sum_j (x_j^{\,2} - y_j^{\,2})\Gamma_j)}{dt}] \sin(2\theta) \right\}, \tag{A11}$$

where **F**[] denotes the Fourier transform in time. Note that Eq. A11 is the dimensionless expression for far-field acoustic pressure. The characteristic parameters used in the expression are the vortex half-span, L, the nominal maximum vortex rotating speed, U, and the density of air, ρ_o.

With only the quadrupole source from the vortex core, the dipole terms (related to sinθ and cosθ) in Eq. A11 are zero. The strengths of the quadrupole terms depend on $\Gamma_j x_j y_j$ and $\Gamma_j (x_j^2 - y_j^2)$, a fact that agrees with expressions for two-dimensional vortex systems obtained by Mohring (1978, 1979) and others (Tang and Ko 2003, Kambe al etc. 1993, Muller 1998, Howe 2003, Mitchell al etc. 1995, Knio al etc. 1995)

Appendix B - Parallelization implementation

Many simulations involve computing the interaction of a large number of particles or objects. If the force between the particles is completely described by adding the forces between all pairs of particles, and the force between each particle acts along the line between them, this is called an N-body problem. Such a problem is a good candidate for parallelization.

In this research, we compute the velocity of, not the force between each particle. Each particle evolves as

$$\frac{d\mathbf{x}_p}{dt} = \mathbf{u}(\mathbf{x}_p, t) = \sum_q K_\sigma(\mathbf{x}_p - \mathbf{x}_q) \times \alpha_q(t)$$

If this is an N particles system, it would require N^2 computations!

To parallel the N-body problem, one simple way is to divide the particles evenly among the P processors. Each processor has N/P particles. P processors should be organized in a ring network. The allocation of data can be performed by an MPI function:

MPI_Scatter(void* sendbuf, int sendcount, MPI_Datatype sendtype, void* recvbuf, int recvcount, MPI_Datatype recvtype, int root, MPI_Comm comm)

Each processor owns a chunk of data (position and vorticity strength of each particle). Each processor keeps a local copy of the chunk for N/P particles. It will send a traveling copy to the next processor in the ring.

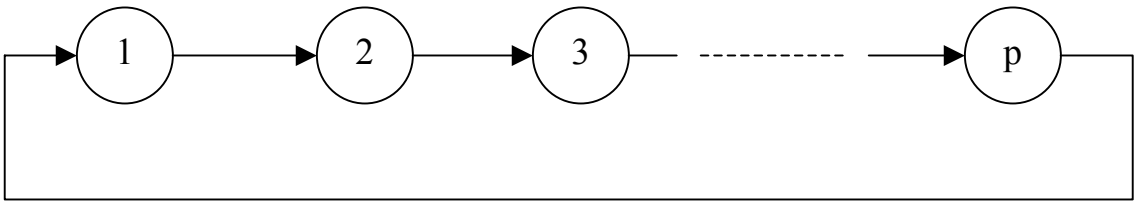

When calculation starts, each processor first computes the velocity between N/P particles it keeps in its chunk. And then each processor computes the velocity between N/P particles it has and N/P particles it receives from left-hand side processor in the ring network through the following for-loop cycle:

```
for(int size=1;size<P;size++){
        MPI_ISend(…);
        MPI_IRecv(…);
}
```

Each processor sums the accumulated velocity of its own.

After one-time marching is done, we can use the following MPI function to perform data collection and output data through one processor (it is called root):

MPI_Gather(void* sendbuf, int sendcount, MPI_Datatype sendtype, void* recvbuf, int recvcounts, MPI_Datatype recvtype, int root, MPI_Comm comm)

However, in most cases, when the particles cannot be divided evenly among the P processors, one has to consider how to divide the particles unevenly into the P processors. We can use a self-defined function

create_mixed_xfer_arrays(myrank, numprocs, prt_number, &cnt, &disp);

to handle the problem. The variable cnt is the array of counts each process has and disp is the array of displacements each process locates in. The two arrays store the message of counts and displacement for each processor.

The following head file MyMPI.h is listed here for the implementation of dividing particles into the P processors.

```
//*****************MyMPI.h************************//
```

```
#ifndef _MYMPI_H_
#define _MYMPI_H_

#include "mpi.h"
#define BLOCK_LOW(id,p,n) ((id)*(n)/(p))
#define BLOCK_HIGH(id,p,n) (BLOCK_LOW((id)+1,p,n)-1)
#define BLOCK_SIZE(id,p,n) (BLOCK_HIGH(id,p,n)-BLOCK_LOW(id,p,n)+1)
#define root 0

//id: IN--process rank; bytes: IN-bytes to allocate //
inline void *my_malloc(int id,int bytes)
{
        void *buffer;
        if((buffer=malloc((size_t) bytes))==NULL){
                printf("Error:Malloc failed for process %d\n",id);
                fflush(stdout);
        }
        return buffer;
}

//id: IN-process rank; p:IN-number of processes;n:IN-total number of elements;//
//count:OUT-array of counts;disp:OUT-array of displacements //
inline void create_mixed_xfer_arrays(int id,int p,int n,int **count,int **disp)
```

```
{
        int i;
        *count=(int *)my_malloc(id,p*sizeof(int));
        *disp=(int *)my_malloc(id,p*sizeof(int));
        (*count)[0]=BLOCK_SIZE(0,p,n);
        (*disp)[0]=0;
        for(i=1;i<p;i++){
                (*disp)[i]=(*disp)[i-1]+(*count)[i-1];
                (*count)[i]=BLOCK_SIZE(i,p,n);
        }
}

#endif /* _MYMPI_H_ */
```

Appendix C - Computational Techniques for Vortex Particle Methods

1. Computational techniques for the two-dimensional vortex particle method

In the 2-D vortex particle method for an incompressible and inviscid flow, the total circulation is conserved. The only equation we need to solve is the time evolution of each particle position (see Section 2.1).

Step 1: Initialization

In a 2-D mesh with uniform size h, each particle is located at the center of each of these cells (see Fig.1). The vorticity strength assigned to the point or particle is the local value of the vorticity multiplied by the volume h^2 of the cell. Therefore, at $t = 0$,

$$\mathbf{x}_p^0 = S_p, \text{ and } \alpha_p^0 = \omega_o h^2$$

where ω_o is the initial vorticity value of each particle and S_p is the position of the center of each cell. If the wake vortex is initialized with a Kirchhoff vortex, the vorticity of the particles inside the vortex core is constant; and outside the core, vorticity is zero.

To calculate velocity for each particle, the modified Biot-Savart kernel is used and the blob radius is $\sigma = 2h$ (see Section 2.1 for more details).

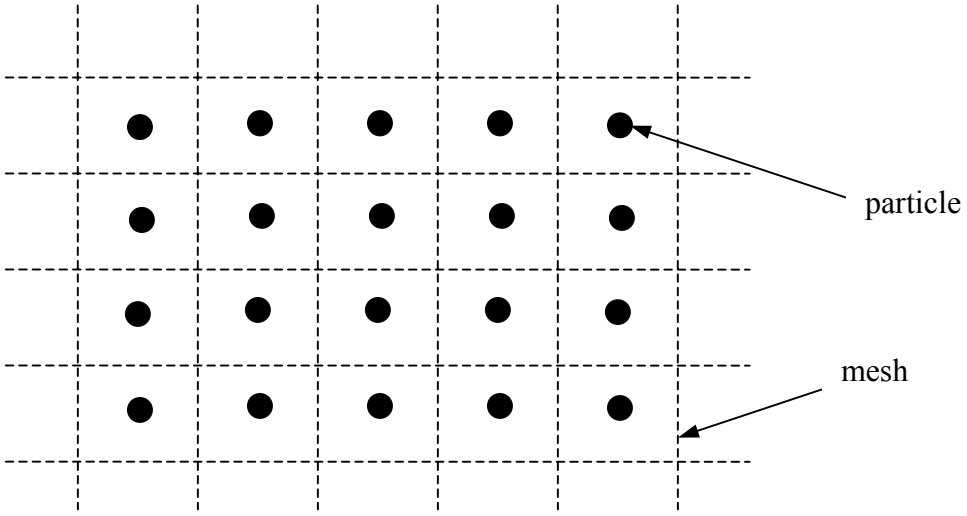

Fig. 1 Illustration of the initialization for a 2-D particle method

Step 2: Time-marching scheme

To solve Eq. 2.7, a numerical time-advancing scheme such as the Runge-Kutta 2nd order scheme is used in the simulation:

$$\mathbf{x}_p^* = \mathbf{x}_p^n + \Delta t \mathbf{u}(\mathbf{x}_p^n),$$

$$\mathbf{x}_p^{n+1} = \mathbf{x}_p^n + \frac{1}{2}\Delta t\left\{\mathbf{u}(\mathbf{x}_p^n) + \mathbf{u}(\mathbf{x}_p^*)\right\}.$$

During the evolution of each particle, the vorticity strength carried by each particle does no change, which can be seen through Eq. 2. 8.

Step 3: Redistribution

For the convergence of a vortex particle method (Beale and Majda 1982), one needs to maintain the condition that particle cores overlap at all times. This calls for a particle redistribution or remeshing scheme. The scheme consists of replacing the distorted set of particles with a new set where the new particles are located on the Lagragian regular grid of *h x h* lattice and simultaneously transporting accurately the vorticity from the old particles to the new ones (see Fig. 2)

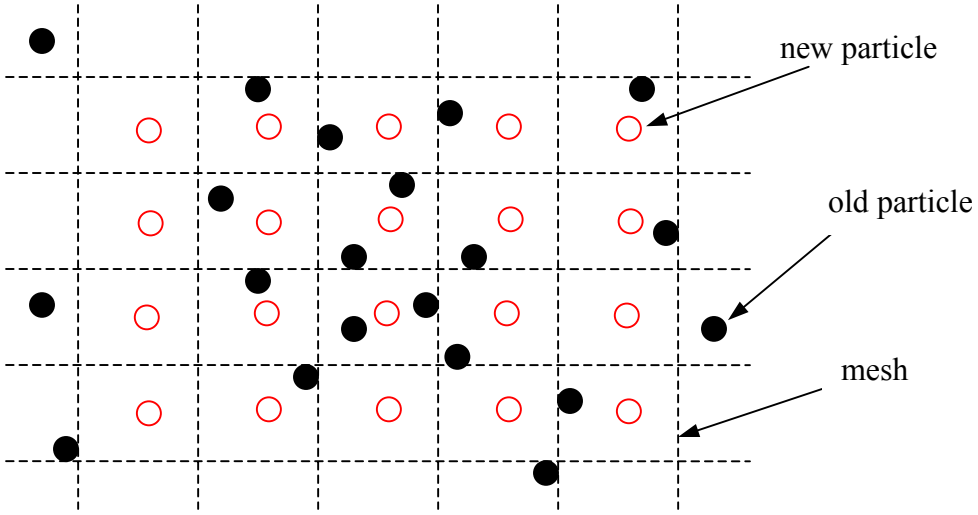

Fig. 2 Illustration of the redistribution for a 2-D particle method

Thus, the new vorticity strength for the particle p is acquired through

$$\tilde{\alpha}_p = \sum_q W_\varepsilon(\tilde{\mathbf{x}}_p - \mathbf{x}_q) h^2 \alpha_q ,$$

where $\tilde{\mathbf{x}}_p$ is the new particle position, $\mathbf{x}_p$ is the old particle position and α_p is the vorticity strength for the old particle q. The interpolation kernel, W, is described in Section 2.1. The value of the new particle position $\tilde{\mathbf{x}}_p$ is the center of each cell S_p, namely $\tilde{\mathbf{x}}_\mathbf{p} = S_p$.

The numerical implementation for the two-dimensional vortex particle method can be summarized in Fig. 3.

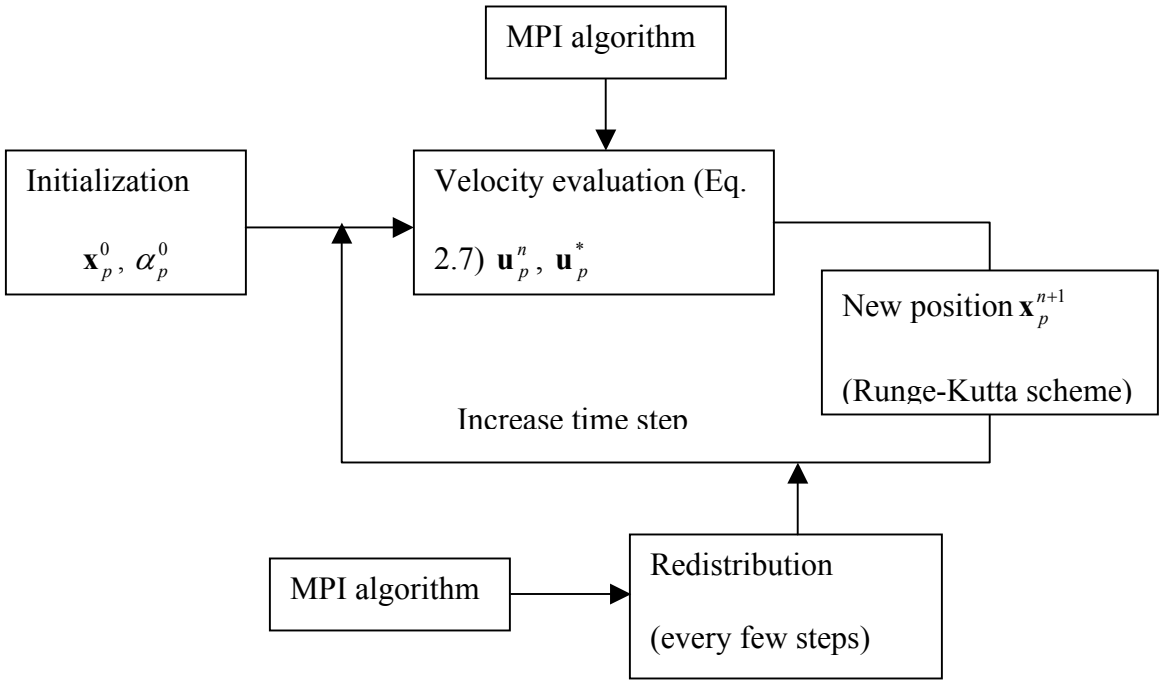

Fig. 3 Numerical procedure of the 2-D vortex particle method

2. Computational techniques for the three-dimensional vortex particle method

Step 1: Initialization

In a 3-D mesh with uniform size *h*, each particle is located at the center of each of these cells (note: a cell represents a cubic volume in a 3-D mesh). The vorticity strength assigned to the point or particle is the local value of the vorticity multiplied by the volume h^3 of the cell. Therefore, at $t = 0$,

$$\mathbf{x}_p^0 = \mathbf{S}_p, \text{ and } \boldsymbol{\alpha}_p^0 = \boldsymbol{\omega}_o h^3,$$

where $\boldsymbol{\omega}_o$ is the initial vorticity value of each particle and $\mathbf{S}_p$ is the position of the center of each cell. It should be noted that the variables, $\mathbf{x},\ \mathbf{S},\ \boldsymbol{\alpha}, \boldsymbol{\omega}_o$, are vectors. If the wake vortex is initialized with a Kirchhoff vortex, the vorticity of the particles inside the vortex core is constant; and outside the core, vorticity is zero.

Step 2: Time-marching scheme

To solve the Eq. 5.7 and Eq. 5.8, a numerical time-advancing scheme such as Runge-Kutta 2nd order scheme is used in the simulation

$$\mathbf{x}_p^* = \mathbf{x}_p^n + \Delta t \mathbf{u}(\mathbf{x}_p^n, \boldsymbol{\alpha}_p^n),$$

$$\boldsymbol{\alpha}_p^* = \boldsymbol{\alpha}_p^n + \Delta t \frac{d\boldsymbol{\alpha}_p}{dt}(\mathbf{x}_p^n, \boldsymbol{\alpha}_p^n),$$

$$\mathbf{x}_p^{n+1} = \mathbf{x}_p^n + \frac{1}{2}\Delta t\left\{\mathbf{u}(\mathbf{x}_p^n, \boldsymbol{\alpha}_p^n) + \mathbf{u}(\mathbf{x}_p^*, \boldsymbol{\alpha}_p^*)\right\},$$

$$\boldsymbol{\alpha}_p^{n+1} = \boldsymbol{\alpha}_p^n + \frac{1}{2}\Delta t\left\{\frac{d\boldsymbol{\alpha}}{dt}(\mathbf{x}_p^n, \boldsymbol{\alpha}_p^n) + \frac{d\boldsymbol{\alpha}}{dt}(\mathbf{x}_p^*, \boldsymbol{\alpha}_p^*)\right\}.$$

The stretching term, $(\boldsymbol{\alpha}\cdot\nabla)\mathbf{u}$ in Eq. 5.8, is evaluated by directly differentiating the velocity kernel (Eq. 5.7) for the current trend (Anderson and Greengard 1985):

$$\nabla\mathbf{u}(\mathbf{x},\boldsymbol{\alpha}) = \sum \nabla\mathbf{k}_\sigma(\mathbf{x}_p - \mathbf{x}_q)\times\boldsymbol{\alpha}_q.$$

The new kernel $\mathbf{R}_\sigma = \nabla\mathbf{k}_\sigma$ can be written in terms of ξ and Q as

$$R_\sigma^{ij}(\mathbf{x}) = \frac{\partial k_{\sigma,i}}{\partial x_j} = \frac{1}{4\pi}\left\{\left(-\xi_\sigma(\mathbf{x}) + \frac{3q(|\mathbf{x}|/\sigma)}{4\pi|\mathbf{x}|^3}\right)\frac{x_i x_j}{|\mathbf{x}|^2} - \frac{Q(|\mathbf{x}|/\sigma)}{4\pi|\mathbf{x}|^3}\delta_{ij}\right\},$$

where the blob function $\xi(\mathbf{x})$ and $q(\mathbf{x})$ are referred to Section 4.2 for details, and δ_{ij} is a delta function, which is 1 when $i = j$ and 0 when $i \neq j$. Note that $R_\sigma^{ij}(0) = -\xi_\sigma(0)\delta_{ij}/3$.

The divergence term, $\mathbf{u}(\nabla\cdot\boldsymbol{\omega})$, is calculated using Eq. 4.10. The calculations of the viscous term and the term of SGS model are described in Sections 4.2 and 4.4, respectively.

Step 3: Redistribution

Similarly with a 2-D particle method, redistribution is also needed in the 3-D vortex particle method to maintain the condition that particle cores overlap at all times. The new vorticity strength for the particle *p* is acquired through

$$\tilde{\boldsymbol{\alpha}}_p = \sum_q W(\frac{\tilde{\mathbf{x}}_p - \mathbf{x}_q}{h})\boldsymbol{\alpha}_q ,$$

where $\tilde{\mathbf{x}}_p$ is the new particle position, $\mathbf{x}_p$ is the old particle position and $\boldsymbol{\alpha}_q$ is the vorticity strength for the old particle *q*. The interpolation kernel, *W*, is described in Section 4.2. The value of the new particle position, $\tilde{\mathbf{x}}_p$, is the center of each cell S_p, namely $\tilde{\mathbf{x}}_\mathbf{p} = \mathbf{S}_p$.

The numerical implementation for the three-dimensional vortex particle method can be summarized in Fig. 4.

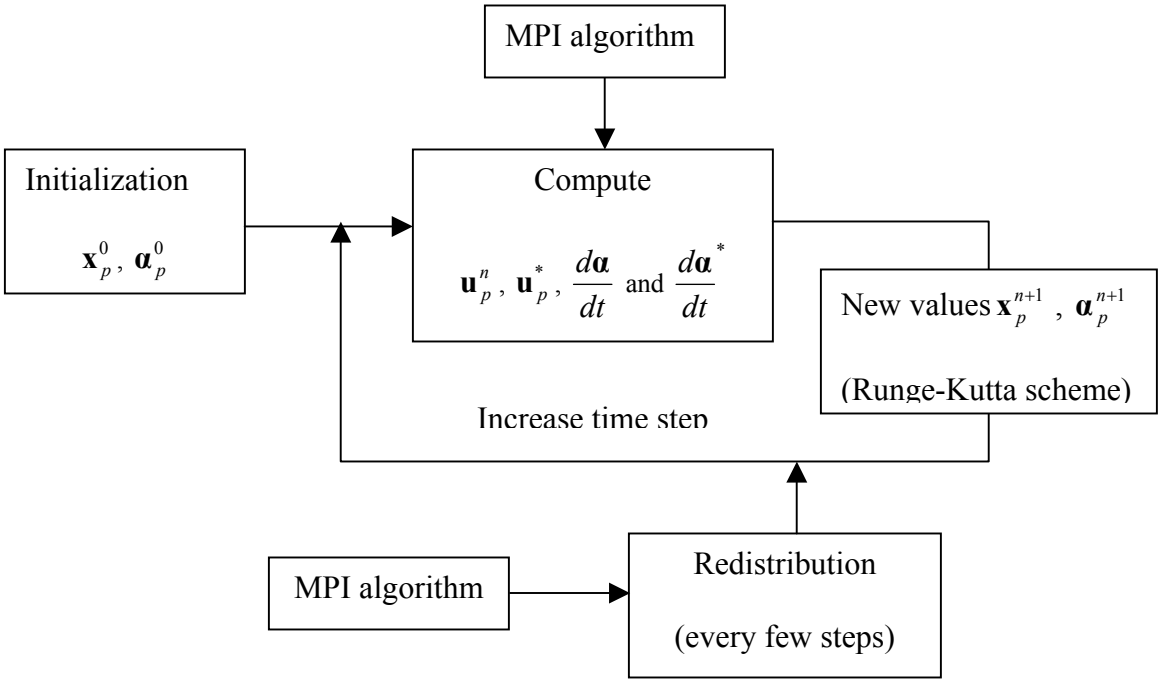

Fig. 4 Numerical procedure of the 3-D vortex particle method

Step 4: Implementation into C++

We use C++ object-oriented software to implement the 3-D vortex particle method. It is very efficient to handle a lot of calculations under a C++ programming environment between vectors and constants such as mathematical algorithms of +, -, * and /. In our numerical simulation, a new class of vector is defined for the purpose as follows:

```
/*
 * Structure declarations of a vector
 */

typedef struct myvector{
      double x,y,z;
      myvector(){};
      myvector(double a,double b,double c){x=a;y=b;z=c;}
      myvector & operator=(double a){x=a;y=a;z=a;return *this;}
}Vector;

inline Vector operator+(const Vector &a,const Vector &b){
      return Vector(a.x+b.x,a.y+b.y,a.z+b.z);}
inline Vector operator+(double a,const Vector &b){
      return Vector(b.x+a,b.y+a,b.z+a);}
inline Vector operator+(const Vector &b,double a){
      return Vector(b.x+a,b.y+a,b.z+a);}

inline Vector operator-(const Vector &a,const Vector &b){
      return Vector(a.x-b.x,a.y-b.y,a.z-b.z);}

inline Vector operator*(const Vector &a,const Vector &b){
      return Vector(a.x*b.x,a.y*b.y,a.z*b.z);}
inline Vector operator*(double a,const Vector &b){
      return Vector(b.x*a,b.y*a,b.z*a);}
inline Vector operator*(const Vector &b,double a){
      return Vector(b.x*a,b.y*a,b.z*a);}

inline Vector operator/(const Vector &b,double a){
      return Vector(b.x/a,b.y/a,b.z/a);}
inline Vector operator/(const Vector &b,const Vector &a){
      return Vector(b.x/a.x,b.y/a.y,b.z/a.z);}

inline Vector & operator+=(Vector &s,const Vector &a){
      s.x +=a.x;s.y +=a.y;s.z +=a.z;
      return s;}
inline Vector & operator-=(Vector &s,const Vector &a){
      s.x -=a.x;s.y -=a.y;s.z -=a.z;
      return s;}
inline Vector & operator*=(Vector &s,const double a){
      s.x *=a; s.y *=a; s.z *=a;
      return s;}
inline Vector & operator/=(Vector &s,const double a){
      s.x /=a; s.y /=a; s.z /=a;
      return s;}

inline double norm(const Vector &a){
```

```
      return sqrt(a.x*a.x+a.y*a.y+a.z*a.z);}
inline double dot(const Vector &a,const Vector &b){
      return a.x*b.x+a.y*b.y+a.z*b.z;}
inline Vector cross(const Vector &a,const Vector &b){
      return Vector(a.y*b.z-a.z*b.y,a.z*b.x-a.x*b.z,a.x*b.y-a.y*b.x);}

inline ostream & operator<<( ostream & s, const Vector & a) {
      return s<<a.x<<" "<<a.y<<" "<<a.z;}
inline istream & operator>>( istream & is, Vector & a) {
      return is>>a.x>>a.y>>a.z;}
```

The definition of a vector is included in the head file named mygeneral.h. A class of a particle is defined based on the above class of a vector:

```
typedef struct ptable {
    Vector pos;                  /* position */
    Vector cir;                  /* strength */
    Vector vel;                  /* velocity */
    Vector acc;                  /* d(alpha)/dt */
    Vector LapVor;               /* viscous term */
    double div;                  /* divergence term */

} PARTICLE;
typedef PARTICLE *PTablePtr;
```

In the MPI parallelization, to accelerate more efficiently the computation of velocity evaluation and $d\boldsymbol{\alpha}/dt$, it is necessary to perform the summation of particles distributed in one CPU and the summation of particles between two difference CPUs separately. For the summation of particles in one CPU, we can reduce the processing time half by considering the symmetry of the summation. For example, evaluation of velocity for a particle p is written as

```
for(p=0;p<N;p++){
      For(q=0;q<N;q++){
            u_p += k_σ(x_p − x_q) × α_q
      }
}
```

Because of $\mathbf{k}_\sigma(-\mathbf{x}) = -\mathbf{k}_\sigma(\mathbf{x})$ (see Section 4.2 for details about the kernel), we can rewrite above algorithms to reduce the simulation time to half:

```
for(p=0;p<N;p++){
      For(q=p+1;q<N;q++){
```

$$\mathbf{u}_p += \mathbf{k}_\sigma(\mathbf{x}_p - \mathbf{x}_q)\times\boldsymbol{\alpha}_q$$
$$\mathbf{u}_q -= \mathbf{k}_\sigma(\mathbf{x}_p - \mathbf{x}_q)\times\boldsymbol{\alpha}_q$$

```
        }
}
```

All the basic calculations such as the evaluation of velocity and $d\boldsymbol{\alpha}/dt$ are completed in the file of element.cpp. The function DirectNeighborCell() is to calculate velocity and $d\boldsymbol{\alpha}/dt$ of particles between different CPUs while the function DirectWithinCell() is to evaluate velocity and $d\boldsymbol{\alpha}/dt$ of particles in the same CPU.

```
//**************************elements.h**************************//

#ifndef _ELEMENTS_H
#define _ELEMENTS_H

#include "mygeneral.h"


class elements{
private:
      DP prt_rad,volume,viscosity,sgs_const;
      int PRDBC,SYMBC;
      Vector CubeLength;

public:
      elements(){};
      elements(int BC_TYPE1,int SYMBC1,DP prt_rad1,DP volume1,DP
viscosity1,const Vector &CubeLength1,DP sgs_const1);
      ~elements();

      void cal_Blob_Qr(DP r,DP &blob,DP &Qr,DP &lap);
      DP cal_BlobFunc0();
      void cal_Blob(DP r,DP &lap);
      void reg_kernel_vel(Vector *diff_k);
      void cal_AllKernel(const Vector &X,Vector &U_k,Vector *diff_k,Vector
&div_k,DP &lap);
      void cal_sgs_model(int Np,const PTablePtr body);
      void cal_sgs_model(int Np,const PTablePtr body,int Nq,const PTablePtr
others);
      void DirectWithinCell(int Np,const PTablePtr body);     /* force.c */
      void DirectNeighborCell(int Np,const PTablePtr body,int Nq,const
PTablePtr others);
};


#endif

//****************************elements.cpp********************//

#include "mpi.h"
```

```
#include "elements.h"


elements::elements(int PRDBC1,int SYMBC1,DP prt_rad1,DP volume1,DP
viscosity1,const Vector &CubeLength1,DP sgs_const1):
PRDBC(PRDBC1),SYMBC(SYMBC1),prt_rad(prt_rad1),volume(volume1),viscosity(visco
sity1),
CubeLength(CubeLength1),sgs_const(sgs_const1)
{
}

//default is to calculate standard scheme and full space interal //
void elements::DirectNeighborCell(int Np,const PTablePtr body,int Nq,const
PTablePtr others)
{
      int i,p,q;

      //calculate d(X)/d(t)=vel and d(cir)/d(t)=acc//
      Vector temp,UU[NDIM],diff_k[NDIM],div_k,UUT[NDIM];
      DP lap,coef_LapVor;

      coef_LapVor=2.0/(prt_rad*prt_rad);
      for(p=0;p<Np;p++){
            for(i=0;i<NDIM;i++) UU[i]=0;
            for(q=0;q<Nq;q++){
                  cal_AllKernel(body[p].pos-
others[q].pos,temp,diff_k,div_k,lap);
                  body[p].vel += cross(temp,others[q].cir);

#ifndef nomore
                  //the term: u*(div(vor))//
                  body[p].div += dot(div_k,others[q].cir+body[p].cir);
#endif
                  for(i=0;i<NDIM;i++) UU[i] +=
cross(diff_k[i],others[q].cir);
                  //diffusion term//
                  body[p].LapVor += (coef_LapVor*lap)*(others[q].cir-
body[p].cir);
            }

            if(PRDBC==1){// peridic bc at x-y plane //
                  Vector PosImag,CirImag;
                  double Z;
                  for(q=0;q<Nq;q++){
                        PosImag=others[q].pos;CirImag=others[q].cir;
                        Z=body[p].pos.z-others[q].pos.z;
                        if(fabs(Z)>1.0e-10){
                              if(Z>0){
                                    PosImag.z += CubeLength.z;
                              }else{
                                    PosImag.z -= CubeLength.z;
                              }
                              cal_AllKernel(body[p].pos-
PosImag,temp,diff_k,div_k,lap);
                              body[p].vel += cross(temp,CirImag);
#ifndef nomore
                              body[p].div += dot(div_k,CirImag+body[p].cir);
```

```
#endif
                              for(i=0;i<NDIM;i++) UU[i] +=
cross(diff_k[i],CirImag);
                              //diffusion term//
                              body[p].LapVor += (coef_LapVor*lap)*(CirImag-
body[p].cir);
                        }
                  }
            }

            //calculate gradient of velocity//
            //standard scheme//
#ifndef transpose
            for(i=0;i<NDIM;i++) UUT[i]=UU[i];
            UU[0].y=UUT[1].x;UU[0].z=UUT[2].x;
            UU[1].x=UUT[0].y;UU[1].z=UUT[2].y;
            UU[2].x=UUT[0].z;UU[2].y=UUT[1].z;
#endif
            //transpose scheme//
            body[p].acc.x += dot(UU[0],body[p].cir);
            body[p].acc.y += dot(UU[1],body[p].cir);
            body[p].acc.z += dot(UU[2],body[p].cir);

      }
}

//default is to calculate standard scheme and full space interal //
void elements::DirectWithinCell(int Np,const PTablePtr body)
{
      int p,q;

      //calculate d(X)/d(t)=vel and d(cir)/d(t)=acc//
      //result_x=[au1/ax1,au2/ax1,au3/ax1],result_y=[au1/ax2,au2/ax2,au3/ax2]
,...//
      Vector
temp,diff_k[NDIM],Xpq,*result_x,*result_y,*result_z,div_k,UUT[NDIM];;
      result_x=new Vector [Np];result_y=new Vector [Np];result_z=new Vector
[Np];
      DP lap,coef_LapVor;
      coef_LapVor=2.0/(prt_rad*prt_rad);

      for(p=0;p<Np;p++){
            result_x[p]=0;result_y[p]=0;result_z[p]=0;
      }
      for(p=0;p<Np;p++){
            for(q=p+1;q<Np;q++){
                  Xpq=body[p].pos-body[q].pos;
                  cal_AllKernel(Xpq,temp,diff_k,div_k,lap);

                  body[p].vel += cross(temp,body[q].cir);
                  body[q].vel -= cross(temp,body[p].cir);

                  result_x[p] += cross(diff_k[0],body[q].cir);
                  result_y[p] += cross(diff_k[1],body[q].cir);
                  result_z[p] += cross(diff_k[2],body[q].cir);
                  result_x[q] += cross(diff_k[0],body[p].cir);
                  result_y[q] += cross(diff_k[1],body[p].cir);
```

```
                result_z[q] += cross(diff_k[2],body[p].cir);

#ifndef nomore
                //the term: u*(div(vor))//
                DP aa;
                temp=body[q].cir+body[p].cir;
                aa=dot(div_k,temp);
                body[p].div += aa;
                body[q].div -= aa;
#endif
                //diffusion term//
                temp=(coef_LapVor*lap)*(body[q].cir-body[p].cir);
                body[p].LapVor += temp;
                body[q].LapVor -= temp;
          }

          if(PRDBC==1){// peridic bc at x-y plane //
                Vector PosImag,CirImag;
                double Z;
                for(q=0;q<Np;q++){
                      Z=body[p].pos.z-body[q].pos.z;
                      if(fabs(Z)>1.0e-10){
                            PosImag=body[q].pos;CirImag=body[q].cir;
                            if(Z>0){
                                  PosImag.z += CubeLength.z;
                            }else{
                                  PosImag.z -= CubeLength.z;
                            }
                            cal_AllKernel(body[p].pos-
PosImag,temp,diff_k,div_k,lap);
                            body[p].vel += cross(temp,CirImag);
#ifndef nomore
                            body[p].div += dot(div_k,CirImag+body[p].cir);
#endif
                            result_x[p] += cross(diff_k[0],CirImag);
                            result_y[p] += cross(diff_k[1],CirImag);
                            result_z[p] += cross(diff_k[2],CirImag);
                            //diffusion term//
                            temp=(coef_LapVor*lap)*(CirImag-body[p].cir);
                            body[p].LapVor += temp;
                      }
                }
          }
     }

     for(p=0;p<Np;p++){
          //if p==q or Xp=Xq//
          reg_kernel_vel(diff_k);
          result_x[p] += cross(diff_k[0],body[p].cir);
          result_y[p] += cross(diff_k[1],body[p].cir);
          result_z[p] += cross(diff_k[2],body[p].cir);
          //calculate gradient of velocity//
          //standard scheme//
#ifndef transpose
          UUT[0]=result_x[p];UUT[1]=result_y[p];UUT[2]=result_z[p];
          result_x[p].y=UUT[1].x;result_x[p].z=UUT[2].x;
          result_y[p].x=UUT[0].y;result_y[p].z=UUT[2].y;
```

```
            result_z[p].x=UUT[0].z;result_z[p].y=UUT[1].z;
#endif
            //transpose scheme//
            body[p].acc.x += dot(result_x[p],body[p].cir);
            body[p].acc.y += dot(result_y[p],body[p].cir);
            body[p].acc.z += dot(result_z[p],body[p].cir);

      }
}


//regularized velocity gradient kernel Ri,j(X)=aKi/axj(X): i--vector j--
array//
void elements::cal_AllKernel(const Vector &X,Vector &U_k,Vector
*diff_k,Vector &div_k,DP &lap)
{
      Vector temp;
      DP r,xrad,mm,qr,blob;

      r=norm(X);
      xrad=r/prt_rad;
      cal_Blob_Qr(xrad,blob,qr,lap);
      mm=qr/4.0/PI/pow(r,3.0);

      U_k=X*(-mm);//BS_Kernel//

      //regularized velocity gradient kernel Ri,j(X)=aKi/axj(X): i--vector j-
-array//
      temp=(-1*blob+3.0*mm)*X/pow(r,2.0);
      diff_k[0]=temp*X.x;diff_k[1]=temp*X.y;diff_k[2]=temp*X.z;
      //for i==j//
      diff_k[0].x -= mm;diff_k[1].y -= mm;diff_k[2].z -= mm;

      //divergent term div(vor)//
      div_k=-1.0*lap/pow(prt_rad,2.0)*X;
}

//regularized velocity gradient kernel Ri,j(X)=aKi/axj(X): i--vector j--
array//
//for special condition: Xp=Xq or r=0//
void elements::reg_kernel_vel(Vector *diff_k)
{
      DP mm;
      diff_k[0]=0;diff_k[1]=0;diff_k[2]=0;
      mm=cal_BlobFunc0();
      mm /= (-3.0);
      diff_k[0].x = mm;diff_k[1].y = mm;diff_k[2].z = mm;
}


//blob distribution: r=0 //
DP elements::cal_BlobFunc0()
{
      DP eps3;
      eps3=pow(prt_rad,3.0);
      return 1.0/pow(2*PI,1.5)/eps3;//error function//
}
```

```
// blob distribution;r=norm(X)/prt_rad,2nd order error function//
void elements::cal_Blob_Qr(DP r,DP &blob,DP &Qr,DP &lap)
{
      DP temp,AA,r2,eps3;
      r2=-0.5*r*r;
      eps3=pow(prt_rad,3.0);
      temp=exp(r2);
      AA=erf(r/sqrt(2.0));

      Qr=AA-sqrt(2.0/PI)*r*temp;
      blob=1.0/pow(2*PI,1.5)*temp/eps3;
      lap=blob;
}
// blob distribution;r=norm(X)/prt_rad,2nd order error function//
void elements::cal_Blob(DP r,DP &lap)
{
      DP temp,r2,eps3;
      r2=-0.5*r*r;
      eps3=pow(prt_rad,3.0);
      temp=exp(r2);

      lap=1.0/pow(2*PI,1.5)*temp/eps3;
}


/*
the SGS model comes from the paper: Winckelmans, G., Cocle, R., etc.
“Vortex methods and their application to trailing wake vortex simulations”.
Comptes Rendus Physique, Vol. 6, No. 4-5, 2005, pp. 467-486.
*/
void elements::cal_sgs_model(int Np,const PTablePtr body)
{
      int p,q;
      double r,lap,coef;
      Vector temp;

      coef=(2.0/(prt_rad*prt_rad))*volume;
      for(p=0;p<Np;p++){
            for(q=p+1;q<Np;q++){
                  r=norm(body[p].pos-body[q].pos);
                  cal_Blob(r/prt_rad,lap);
                  temp=(body[q].LapVor-body[p].LapVor)*(coef*lap);
                  body[p].acc += (sgs_const*volume)*temp;
                  body[q].acc -= (sgs_const*volume)*temp;
            }
            if(PRDBC==1){// peridic bc at x-y plane //
                  Vector PosImag;
                  double Z;
                  for(q=0;q<Np;q++){
                        Z=body[p].pos.z-body[q].pos.z;
                        if(fabs(Z)>1.0e-10){
                              PosImag=body[q].pos;
                              if(Z>0){
                                    PosImag.z += CubeLength.z;
                              }else{
```

```
                                    PosImag.z -= CubeLength.z;
                              }
                              r=norm(body[p].pos-PosImag);
                              cal_Blob(r/prt_rad,lap);
                              temp=(body[q].LapVor-
body[p].LapVor)*(coef*lap);
                              body[p].acc += (sgs_const*volume)*temp;
                        }
                  }
            }
      }
}

void elements::cal_sgs_model(int Np,const PTablePtr body,int Nq,const
PTablePtr others)
{
      int p,q;
      double r,lap,coef;
      Vector temp;

      coef=(2.0/(prt_rad*prt_rad))*volume;
      for(p=0;p<Np;p++){
            for(q=0;q<Nq;q++){
                  r=norm(body[p].pos-others[q].pos);
                  cal_Blob(r/prt_rad,lap);
                  temp=(others[q].LapVor-body[p].LapVor)*(coef*lap);
                  body[p].acc += (sgs_const*volume)*temp;
            }
            if(PRDBC==1){// peridic bc at x-y plane //
                  Vector PosImag;
                  double Z;
                  for(q=0;q<Nq;q++){
                        PosImag=others[q].pos;
                        Z=body[p].pos.z-others[q].pos.z;
                        if(fabs(Z)>1.0e-10){
                              if(Z>0){
                                    PosImag.z += CubeLength.z;
                              }else{
                                    PosImag.z -= CubeLength.z;
                              }
                              r=norm(body[p].pos-PosImag);
                              cal_Blob(r/prt_rad,lap);
                              temp=(others[q].LapVor-
body[p].LapVor)*(coef*lap);
                              body[p].acc += (sgs_const*volume)*temp;
                        }
                  }
            }
      }
}
```

The other computations of input, output, parallelization, time-marching etc. are implemented in the file named `INCOMP_VPM.cpp`, which defines a new class to handle all the computations. All initial parameters such as time step size, grid size, distribution type of a vortex

core and so on are introduced into the simulation through the file input.txt. And the constructor function of the class INCOMP_VPM finishes the initialization of particles and MPI parallelization, which calls for the functions ReadParticlePos() and SetIniCond(). The function update_rk2() performs the time-marching work using the Runge-Kutta numerical scheme. The function remesh() performs the calculation of redistribution to get new values of position and vorticity strength for each particle. The output includes the values of vorticity, velocity, and farfield pressure.

The detailed procedure to call for functions is in Fig. 5:

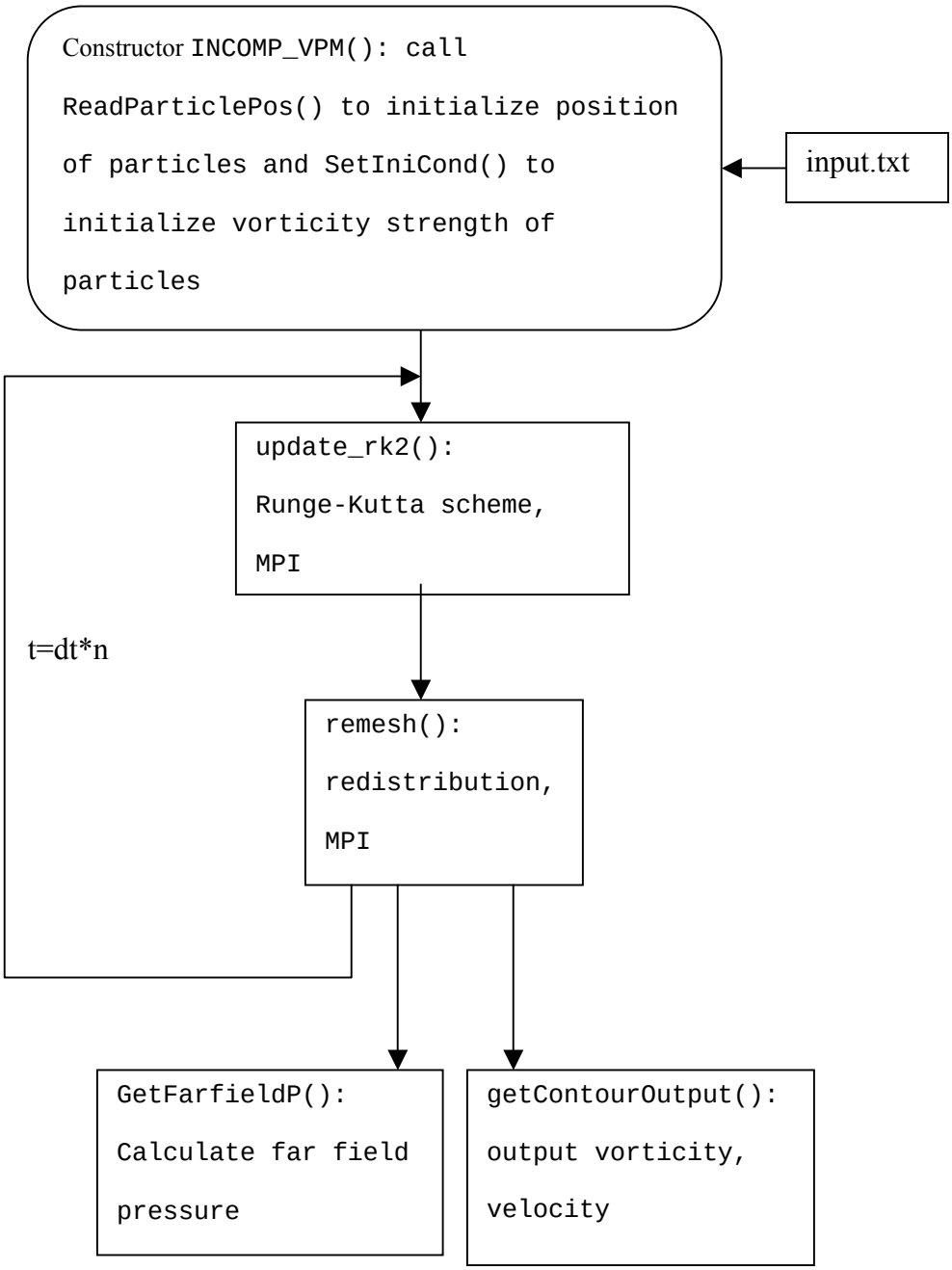

Fig. 5 Call procedure of subroutines in INCOMP_VPM.cpp